Bandwidth Scaling Behavior in Wireless Systems: Theory, Experimentation, and Performance Analysis

by

Wesley M. Gifford

S.M., Massachusetts Institute of Technology (2004)
B.S., Rensselaer Polytechnic Institute (2001)

Submitted to the Department of Electrical Engineering and Computer Science
in partial fulfillment of the requirements for the degree of

Doctor of Philosophy in Electrical Engineering

at the

MASSACHUSETTS INSTITUTE OF TECHNOLOGY

September 2010

Author ....
Department of Electrical Engineering and Computer Science
September 2, 2010

Certified by ....
Moe Z. Win
Associate Professor
Thesis Supervisor

Accepted by ....
Professor Terry P. Orlando
Chairman, Department Committee on Graduate Students

Bandwidth Scaling Behavior in Wireless Systems: Theory, Experimentation, and Performance Analysis

by

Wesley M. Gifford

Submitted to the Department of Electrical Engineering and Computer Science
on September 2, 2010, in partial fulfillment of the
requirements for the degree of
Doctor of Philosophy in Electrical Engineering

Abstract

The need for ubiquitous wireless services has prompted the exploration of using increasingly larger transmission bandwidths often in environments with harsh propagation conditions. However, present analyses do not capture the behavior of systems in these channels as the bandwidth changes. This thesis: describes the development of an automated measurement apparatus capable of characterizing wideband channels up to 16 GHz; formulates a framework for evaluating the performance of wireless systems in realistic propagation environments; and applies this framework to sets of channel realizations collected during a comprehensive measurement campaign. In particular, the symbol error probability of realistic wideband subset diversity (SSD) systems, as well as improved lower bounds on time-of-arrival (TOA) estimation are derived and evaluated using experimental data at a variety of bandwidths. These results provide insights into how the performance of wireless systems scales *as a function of bandwidth.*

Experimental data is used to quantify the behavior of channel resolvability as a function of bandwidth. The results show that there are significant differences in the amount of energy captured by a wideband SSD combiner under different propagation conditions. In particular, changes in the number of combined paths affect system performance more significantly in non-line-of-sight conditions than in line-of-sight conditions. Results also indicate that, for a fixed number of combined paths, lower bandwidths may provide better performance because a larger portion of the available energy is captured at those bandwidths.

The expressions for lower bounds on TOA estimation, developed based on the Ziv-Zakai bound (ZZB), are able to account for the a priori information about the TOA as well as statistical information regarding the multipath phenomena. The ZZB, evaluated using measured channel realizations, shows the presence of an *ambiguity region* for moderate signal-to-noise ratios (SNRs). It is shown that in a variety of propagation conditions, this ambiguity region diminishes as bandwidth increases. Results indicate that decreases in the root mean square error for TOA estimation were significant for bandwidths up to approximately 8 GHz for SNRs in this region.

Thesis Supervisor: Moe Z. Win
Title: Associate Professor

Acknowledgments

The success of this thesis is due to the contributions of many people. I am grateful to my advisor, Professor Moe Win, whose mentoring, encouragement, and tireless energy have helped tremendously throughout the research process. I am also indebted to Professor Dennis Freeman and Professor Vivek Goyal for their helpful advice and feedback during my graduate program.

Most importantly, I would like to thank Stacey MacGrath for always being there when I need her. Without her support and encouragement, this dissertation would not have been possible. I also thank my parents and family for their unwavering support. I especially thank my father for his invaluable advice and assistance during the design and fabrication of the positioning subsystem.

I also thank my Italian colleagues, Professor Marco Chiani, Professor Davide Dardari, and Professor Andrea Conti. The success of this thesis is due to several fruitful collaborations with these colleagues, and I look forward to working with them in the future.

I thank my colleagues and friends in the Wireless Communications Group at LIDS for helpful discussions. I am especially grateful to Dr. Henk Wymeersch, Yuan Shen, Watcharapan Suwansantisuk, William Weiliang Li, Ulric Ferner, Stefano Maranò, Dr. Pedro Pinto, and Megumi Ando.

This thesis was greatly facilitated by assistance along the way from: Joseph Gencorelli and Michael Ballou at Agilent Technologies, Douglas Pitts at Numatics Motion Control, and Riaan Booysen at Saab-Grintek.

I would also like to acknowledge support from the MIT Claude E. Shannon Endowment Fund, the John W. Jarve Fellowship, the Office of Naval Research Young Investigator Award N00014-03-1-0489, the Office of Naval Research Presidential Early Career Award for Scientists and Engineers (PECASE) N00014-09-1-0435, the National Science Foundation under Grants ANI-0335256, ECS-0636519, and ECCS-0901034, the Charles Stark Draper Laboratory, the Defense University Research Instrumentation Program under grant N00014-08-1-0826, and the MIT Institute for Soldier Nanotechnologies.

Contents

List of Figures

List of Tables

List of Notation

$(\cdot)^T$	Matrix transpose
$(\cdot)^\dagger$	Conjugate transpose
$(\cdot)^{-1}$	Matrix inverse
$\mathbf{A} \otimes \mathbf{B}$	The Kronecker product of the matrices $\mathbf{A}$ and $\mathbf{B}$. If $\mathbf{A}$ is an $m \times n$ matrix

$$\mathbf{A} \otimes \mathbf{B} = \begin{bmatrix} a_{11}\mathbf{B} & \cdots & a_{1n}\mathbf{B} \\ \vdots & \ddots & \vdots \\ a_{m1}\mathbf{B} & \cdots & a_{mn}\mathbf{B} \end{bmatrix}$$

$(\cdot)^*$	Complex conjugate
$\mathrm{tr}\{\cdot\}$	Trace of a matrix
$\det\{\cdot\}$	Determinant of a matrix
$\mathbb{E}\{\cdot\}$	Expectation
$\mathbb{V}\{\cdot\}$	Variance
$\mathrm{Cov}\left\{\cdot, \cdot\right\}$	Covariance
$\Pr\{\cdot\}$	Probability
$\langle \cdot, \cdot \rangle$	Inner product
$\Re\{c\}$	Real part
$\Im\{c\}$	Imaginary part
$\{a_i\}_{i=1}^N$	The set consisting of elements $a_1, a_2, \ldots, a_N$

List of Acronyms

AWGN	additive white Gaussian noise
SNR	signal-to-noise ratio
UWB	ultrawide bandwidth
VNA	vector network analyzer
IF	intermediate frequency
IDFT	inverse discrete Fourier transform
FFT	fast Fourier transform
IFT	inverse Fourier transform
FT	Fourier transform
SS	spread spectrum
WSSUS	wide-sense stationary uncorrelated scattering
RSSD	Rake subset diversity
SP	single path
ARake	all Rake
SRake	selective Rake
MFEP	matched front-end processor
ELP	equivalent lowpass

BEP	bit error probability
SEP	symbol error probability
SSD	subset diversity
MRC	maximal-ratio combining
H-S/MRC	hybrid selection/maximal-ratio combining
RV	random variable
IID	independent, identically distributed
PDF	probability density function
MGF	moment generating function
CF	characteristic function
MSE	mean square error
MMSE	minimum mean square error
RMSE	root mean square error
LSE	least squares estimate
LLSE	linear least squares estimate
ML	maximum likelihood
LRT	likelihood ratio test
LR	likelihood ratio
LLR	log-likelihood ratio
CRB	Cramér-Rao bound
ZZB	Ziv-Zakai bound
ZZBT	Ziv-Zakai Bellini-Tartara
LOS	line-of-sight

NLOS	non-line-of-sight
GPS	Global Positioning System
TOA	time-of-arrival
UWB	ultrawide bandwidth
TH	time-hopping
PPM	pulse position modulation
PDP	power delay profile
WWB	Weiss-Weinstein bound
CPR	channel pulse response
LRT	likelihood ratio test
RRC	root raised cosine
PDP	power delay profile

Chapter 1

Introduction

The emergence of ubiquitous wireless services has prompted the exploration of using increasingly large bandwidth transmission, often in challenging environments and over bandwidths that are already in use for legacy systems. Current demands in quality and reliability of wireless connections suggest that ever-higher bandwidths in various frequency bands be made available in an unlicensed manner for unrestricted wireless access. Along this line, ultrawide bandwidth (UWB) spread spectrum systems have received considerable attention from the scientific, commercial and military sectors [1–15].

The use of extremely large transmission bandwidth results in desirable capabilities, including: 1) accurate positioning and ranging, and lack of significant multipath fading due to fine delay resolution; 2) simple implementation for multiple access communications; and 3) superior obstacle penetration due to low frequency components [3–7]. Interest in UWB systems has intensified owing to a ruling by the United States Federal Communications Commission (FCC) concerning UWB emission masks.[1] This ruling is flexible enough to allow various implementations that satisfy the emission mask condition [16], enable UWB to coexist with traditional and protected radio services, and permit the use of UWB transmission without allocated spectrum.

Among other advantages, UWB systems inherently provide covert communication due to low power operation in an extremely large transmission bandwidth combined with spread spectrum techniques. UWB systems possess low probability of detection and interception (LPD/LPI) as well as anti-jam capabilities. By virtue of their robustness against fading

---

[1] Similar activities are also underway in other countries.

and superior obstacle penetration, UWB systems allow reliable communication in extremely challenging environments, where there are obstacles and dense multipath. Examples include dense urban areas, confined areas, within buildings, onboard vehicles, and in shipyards. It is known that current communication systems used by the military and emergency services do not perform well, or may fail altogether, under such conditions. UWB networks promise reliable, low-power and high-speed services for time-critical information to be relayed to its destination even in such challenging environments. Consequently, UWB systems are under consideration for many applications, including high-speed short-range WiFi, emergency services, military communications networks, sensor networks, and homeland defense systems [10–15].

1.1 Channel Characterization

Characterization of wideband channels requires precise measurements over a very large bandwidth. Typically this is done using two methods: 1) time-domain based channel sounding using very short duration pulses and a digital sampling oscilloscope, and 2) frequency-domain based channel measurement using a vector network analyzer (VNA). The first method uses a pulse generator to generate short pulses and a digital sampling oscilloscope to sample the channel response. Usually a series of pulses, modulated by a pseudo-random sequence, are transmitted to improve the SNR and produce more reliable measurements. These specialized channel sounders can be prohibitively expensive and are generally not widely available. Channel sounders also have limited dynamic range because they operate over the entire bandwidth of interest and hence are subject to the broadband noise floor.

Using the time-domain based method, extensive UWB propagation measurement campaigns have previously been performed in a modern laboratory/office building with the goal of characterizing the channel [3–7]. For these campaigns, a nanosecond-wide pulse was transmitted periodically with a repetition rate of 2×10^6 pulses per second.

The research described in this thesis made use of the second method to measure channel responses in the frequency domain over the 2–18 GHz range. VNAs use a swept sine wave stimulus and therefore have better dynamic range, because the measurement is only made over the intermediate frequency (IF) bandwidth; a much smaller bandwidth. VNAs also come equipped with built in error correction capabilities which can correct for errors induced by cables and impedance mismatches. Using this method it is easier to characterize the propagation channel over various bandwidths, since the measured responses can simply be filtered. The time-domain response can easily be computed using the inverse Fourier transform of the measured frequency response. A recent measurement campaign using a VNA to measure the 3–10 GHz frequency range is available in [17].

1.2 Wideband Diversity

Multipath diversity using spread spectrum (SS) signaling [18–25] has played an increasingly important role in current and future wireless systems. Wide transmission bandwidths available in SS systems allow receivers to resolve closely spaced multipath components. The detection of signals in multipath environments is typically done using a Rake receiver, where the components of a received signal (arriving at different delays) are combined to provide diversity. Discussions on classical Rake architectures can be found in [18–21]. One version of the Rake receiver consists of multiple correlators (fingers); each correlator detecting the signal from one of the multipath components created by the channel. The outputs of the Rake fingers are then combined to achieve the benefits of multipath diversity.

The complexity and performance issues associated with combining all the available multipath components have motivated studies of receivers that process only a *subset* of the available resolved multipath components. Such Rake subset diversity (RSSD) receivers are a way to reduce resource use in receiver designs while maintaining the benefits of full diversity order [26–29]

Practical RSSD receivers must estimate the channel gain affecting each multipath component, and thereby incur a performance loss [30–35]. This is in contrast to many previous studies of RSSD which assumed that perfect channel knowledge is available at the receiver. In the case of practical RSSD, the estimation plays a dual role; it affects *both* the selection process as well as the combining mechanism. Indeed, in an RSSD receiver the subset of multipath components chosen is based on the receiver's knowledge of the channel, i.e., the *estimated* channel gains. Therefore, there is the possibility that the receiver makes an erroneous selection.

1.3 Ranging Error Bounds

One of the primary advantages of ultra wideband communication is the fine delay resolution that results from wide transmission bandwidth. For this reason, wideband systems are receiving increasing attention for use in ranging and localization systems. One way these systems operate is by time-of-arrival (TOA) estimation, where the first path of the received signal is detected to form an estimate of the distance from transmitter to receiver. However, when operating in dense multipath environments these systems are affected by errors induced by phenomena such as direct path blockage and direct path excess delay.

In some areas of the environment the direct path to a transmitter may be completely obstructed, so that the only received signals are from reflections, resulting in measured ranges larger than the true distances. Direct path excess delay occurs when the partially obstructed direct path propagates through different materials, such as walls. When such a partially obstructed direct path signal is observed as the first arrival, the propagation time depends not only upon the traveled distance, but also upon the materials it encountered. Because the propagation of electromagnetic signals is slower in some materials than in the air, the signal arrives with excess delay, again yielding a range estimate larger than the true one. It is important to note that the effect of direct path blockage and direct path excess delay is the same: they both add a positive bias to the true range, so that the measured range is larger than the true value. This positive error has been identified as a limiting factor in UWB ranging performance and it must be taken into account [36, 37].

While the performance of a specific TOA estimation algorithm can be evaluated, estimation error bounds play a fundamental role since they can serve as useful performance benchmarks for the design of TOA estimators. The CRB has been widely used as a performance benchmark for assessing estimation error. However, it is well known that the CRB can be very loose at low and moderate SNR. Other bounds, such as the ZZB, can be applied to a wider range of SNRs and account for both ambiguity effects and a priori information of the parameter to be estimated. It is expected that as the bandwidth increases, the bound on the TOA estimation error will decrease, because larger bandwidth yields finer delay resolution. However, there may be a point where the improvement diminishes. Understanding the point at which this occurs is valuable to system engineers.

1.4 Contributions

This thesis first describes a channel measurement apparatus that was designed and built to accurately characterize wideband propagation channels over a frequency range of 2–18 GHz. This frequency range represents more than double the bandwidth of conventional UWB systems. The apparatus contains an automated positioning subsystem, responsible for positioning the receive antenna, to enable accurate and rapid collection of channel responses. The extremely wide measurement bandwidth allows for the investigation of the effects of bandwidth at ranges beyond those currently available in the literature. The data collected using this apparatus is used in the subsequent chapters to make conclusions about the effects of bandwidth in realistic propagation environments.

This thesis characterizes the SEP performance of wideband subset diversity (SSD) systems operating in multipath channels. These systems operate by selecting and combining a subset of the resolvable multipath components. Analytical expressions are developed for the case of non-ideal channel estimation, where the selection and combining process occur in the presence of channel estimation error. Two channel models are considered. The first considers a wide-sense stationary uncorrelated scattering (WSSUS) channel with a constant PDP. The second considers the case where only a set of channel realizations is available. In this case, the expressions are semi-analytical in nature—they are based on Monte-Carlo averaging of exact conditional SEP expressions. The analysis is valid for arbitrary two-dimensional signaling constellations and the expressions give insight into the performance losses of non-ideal SSD when compared to ideal SSD. Due to estimation error, these losses occur in branch combining as well as in branch selection. The SEP performance as a function of bandwidth is investigated under different propagation conditions. Results indicate that increased bandwidth yields more multipath components, and thereby increases the diversity present in the channel. However, operation at 1 GHz bandwidth provides better performance in terms of SEP because there is significantly more energy present in each path.

This thesis also investigates lower bounds on TOA estimation error for wideband and UWB ranging systems operating in realistic multipath environments. The thesis specifically considers developing bounds on TOA estimation for two cases: 1) when a statistical model of the multipath phenomena is available and 2) when only a finite set of channel realizations are available. In particular, analytical expressions for the CRB and ZZB on TOA estimation error for dense multipath channels are provided and discussed under different operating conditions. It is shown that for practical values of the SNR the classical CRB does not properly account for multipath effects and hence one needs to resort to improved bounds, such as those based on the ZZB. Using these bounds it is also shown how a priori knowledge about the multipath characteristics can improve TOA estimation performance. Furthermore, these bounds serve as useful performance benchmarks for the design of TOA estimators.

1.5 Organization

This thesis is organized as follows. Chap. 2 describes the channel measurement apparatus, including the positioning and measurement subsystems, as well as the software developed to control them. Chap. 3 gives specific details about the measurement campaign that was performed on the MIT campus, how the captured waveforms were processed, and describes the procedure for extracting the gains and delays from individual channel responses. Chap. 4 develops a framework for investigating the performance of non-ideal wideband diversity systems, both for theoretical models and measured channel responses. Chap. 5 develops a framework for the evaluation of the CRB and ZZB on the TOA estimation error of wideband signals affected by multipath propagation.

Chapter 2

Measurement Apparatus

This chapter describes a channel measurement apparatus that was custom designed and fabricated to precisely measure extremely wideband wireless channels. The measurement apparatus consists of two major components: 1) the positioning subsystem, and 2) the wireless channel measurement subsystem. Care was taken in designing both subsystems to maximize the fidelity of the measurement data, while maintaining the flexibility of the overall apparatus. The complete channel measurement apparatus, including the transmit antenna, is shown in Fig. 2-1. The next sections describe the positioning and channel measurement subsystems, as well as the associated calibration procedures. Finally, a detailed discussion of the software developed to control the measurement apparatus is presented.

2.1 Positioning Subsystem

In order to understand and predict the performance of systems operating in realistic environments, it is first necessary to understand the statistical nature of the communication channel. To develop statistical models for the communication channel, one must capture numerous channel realizations. Typically, each of these channel realizations is collected by fixing the transmit and receive antenna, transmitting a known signal, and capturing the response. Then, the position of the receive antenna is moved to the next point and the process continues. Once all the measurements have been captured over a small-scale grid, additional measurements are then made by moving the small-scale grid to a new location. Since manual positioning of the transmit and receive antenna to collect this data can be time consuming, tedious, and error prone, the measurement apparatus incorporates an

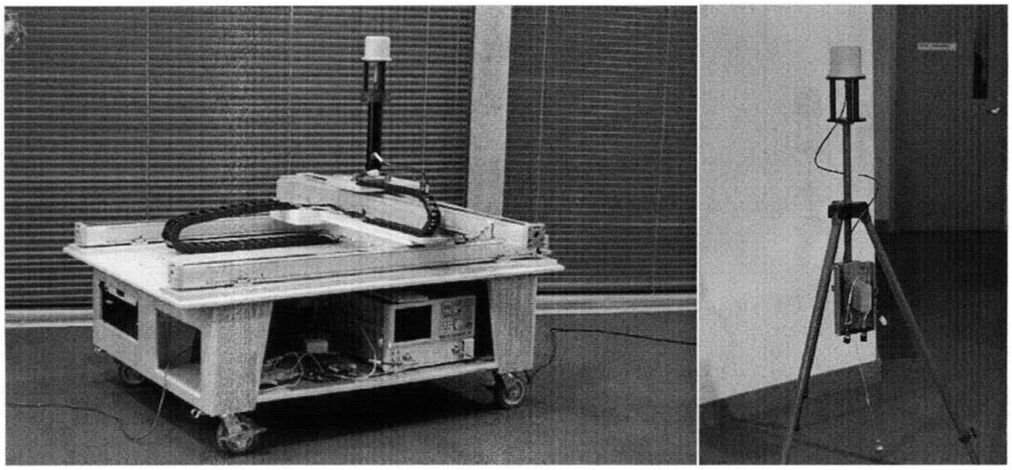
(a) (b)

Figure 2-1: The channel measurement apparatus: (a) the positioning subsystem and measurement hardware, (b) the transmit antenna mounted at the top of the tripod, along with the amplifier and coupler located near the base of the tripod.

automated positioning subsystem to position the receive antenna.

2.1.1 Configuration

The positioning subsystem consists of a mobile cart, three linear motion units, and the necessary motors and motor controllers. The mobile cart was constructed primarily of nonmetallic materials, including wood, plastic, fiberglass, and other composites to minimize any effects on the propagation environment. It measures 1.73 m × 1.22 m, and was designed to support the linear motion units, as well as the measurement hardware, while still allowing mobility. The mobile cart was also designed with enough space below the linear motion units to store the measurement and control hardware, creating a self-contained measurement apparatus.

The linear motion units, typically used in factory automation applications, offer speed and precision in positioning. Each unit consists of a track and a saddle which rides in the track. The saddle is connected to a timing belt which runs over two timing pulleys located at the ends of the track. One of the timing pulleys, the drive pulley, is rotated by a stepper motor. A Cartesian positioning grid is formed using these three units. Two units, parallel to each other and linked by a common drive shaft, form the y-axis. The third unit, perpendicular to the other units, is mounted on top of the saddles of the lower units to form the x-axis. The receive antenna is mounted on a small platform located on the

Name	Mfr. Name, Model (Alt. Mfr. Name, Model)
Linear motion units	Numatics, BDU 75 (Warner, Rapidtrak M75)
Motor controllers	Numatics, NSDP6C (Superior Electric, SS2000D6i)
Stepper motors	Numatics, FLM9310 (Superior Electric, KM093)
X-axis gearbox	GAM, EPL-N34-003G
Y-axis gearbox	GAM, HPS-TB-075-003G
X-axis coupler	Lovejoy, L-070
Y-axis couplers	GAM/Jakob, EKZ 20/304

Table 2.1: Components used in the positioning subsystem

saddle of the top axis. Each linear motion unit is about 1.8 m long and is capable of 1.2 m of travel. The distance moved for every rotation of the drive pulley, referred to as the drive ratio, is 12.98 cm/rev. The two axes allow positioning the receive antenna anywhere in a 1.2 m × 1.2 m grid. The positioning subsystem can be seen in Fig. 2-1 and details about the components can be found in Table 2.1.

Movement of each axis of the positioning grid is accomplished by a stepper motor mounted to a low-backlash, high precision, 3:1 gear-reducer. The stepper motors have 200 full steps per revolution (1.8° per step), but are operated in micro-stepping mode (with one microstep equal to 1/64-th of a full step). A separate stepper motor drive controller is responsible for controlling each the stepper motors. The motor controllers have internal microprocessors which control the motion profile of each axis and enable the user to issue configuration and control commands over a serial interface.

Each axis of the positioning grid has three position sensors. Two of these sensors are used as end of travel limit sensors. These protect the linear motion units from damage if the saddle attempts to travel past the end of the unit. The third sensor, or home sensor, is used to determine the origin of the axis. The motor controller software includes commands that use the end of travel limit sensors and the home sensor to calibrate the axis. These sensors are also used to check the accuracy of the positioning subsystem.

2.1.2 Accuracy and Precision

Accuracy refers to the degree to which a measurement is close to the true value. Precision, or repeatability, is the degree to which measurements show the same results. There are several factors affecting the overall accuracy and precision of the positioning subsystem. In the context of the positioning subsystem, accuracy refers to how closely the desired position matches the actual position. Precision refers to how close repeated movements to the same location are to one another. An ideal positioning system will have both high accuracy and precision. Below we discuss the individual components of the positioning subsystem and their effect on the overall accuracy and precision.

The overall accuracy and precision of the positioning subsystem is ±1 mm and 0.42 mm, respectively. This level of accuracy and precision is acceptable, since, during experiments, the mobile cart must be moved to locations where measurements will be taken. The coordinates of this location are recorded, to be able to understand propagation conditions and to calculate the true distance between the transmit and receive antennas. It is extraordinarily difficult to position the cart and measure its location with greater accuracy than that of the positioning subsystem.

The positioning subsystem has high resolution, since the motor controllers are configured to operate in micro-stepping mode with 1/64-th step resolution. This gives 12,800 microsteps per revolution of the stepper motors or a final positioning resolution of $< 0.0034\,\text{mm}$ for each axis. The accuracy and precision of the positioning subsystem is dominated by the linear motion units, where the main contributing factor is the interaction between the timing belt and timing pulleys. The specified positioning accuracy of the linear motion units is ±0.8333 mm/m and the repeatability is ±0.3 mm. This contributes $\pm 1.2 \times 0.8333 = 1.00\,\text{mm}$ and ±0.3 mm to the accuracy and repeatability, respectively.

Other components in the system also contribute to the overall accuracy and precision. However, their effects are much less significant. The stepper motors themselves are accurate to within ±2% of a full step, non-cumulative. These errors do not accumulate as the number of steps increases because of the way stepper motors are designed. Thus, the positioning accuracy of the stepper motors is $\pm 2\% \cdot 129.79/(3 \cdot 200) = \pm 0.0043\,\text{mm}$—significantly smaller than the accuracy of the linear motion units. The gearboxes also contribute to the accuracy and precision. Backlash is a term that refers to the clearance between mating components, in our case the gears in the gear reducers, in a mechanical device. It can be thought of as the amount of lost motion when movement is reversed and contact between the gears is re-established. This affects the precision of the positioning system, but again, the effects are less significant than the precision of the linear motion units. The gear reducers have an output backlash of <10 arcmin and <6 arcmin for the x-axis and y-axis, respectively. This

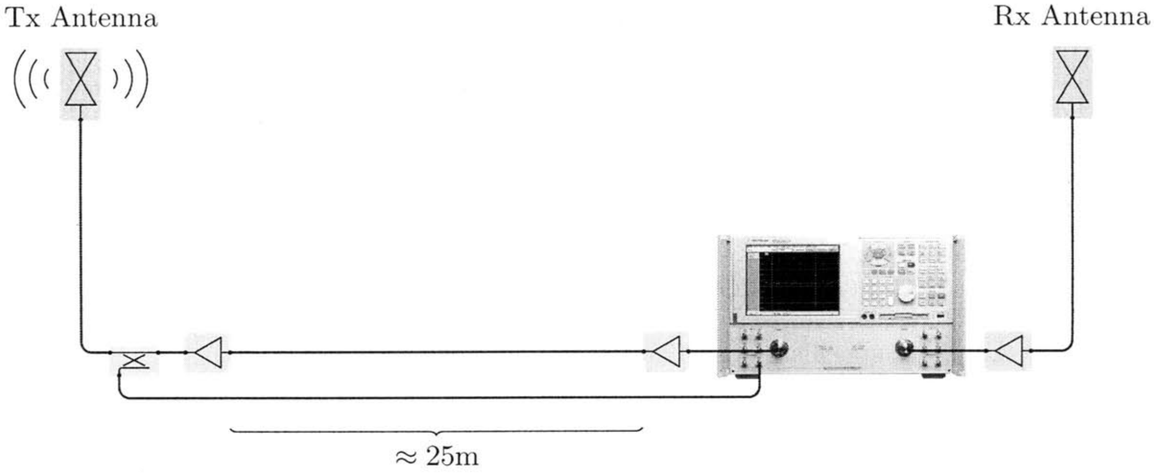

Figure 2-2: Setup of the measurement system

creates an additional positioning uncertainty of ±0.060 mm and ±0.036 mm, respectively.

2.1.3 Summary

The positioning subsystem enables extremely flexible positioning of the receive antenna. Grid layouts which would be very difficult to achieve with manual positioning, are now possible with the positioning subsystem. Furthermore, moving from one grid point to the next takes less than a few seconds compared to several minutes for manual positioning. Also, the accuracy achieved through automated positioning is far better than one can achieve with manual positioning. This allows for accurate and extremely rapid data collection. The convenience and accuracy of automated positioning comes with the cost of additional hardware and the presence of this hardware during the measurements. Ideally, channel measurements are taken to capture the propagation environment only. However, in a practical setting, these measurements will capture the effect of the environment and all the objects in it, including the measurement hardware. No matter the setup, it is impossible to remove all the effects of the measurement hardware.

2.2 Channel Measurement Subsystem

A VNA makes up the core of the channel measurement subsystem. VNAs are capable of accurately measuring the incident, reflected, and transmitted signals associated with a device under test. VNAs operate as a stimulus-response system: a known signal is transmitted and the resulting signals are measured. The channel measurement subsystem uses an Agi-

Location	Mfr. Name, Model	Output Power (dBm)	Gain (dB)	Noise Figure (dB)
Transmit path	Lucix, S001200L2405	20	24	3.5
Receive path	Herotek, AF0120183A	8	18	2.8
Receive path	Lucix, S001200L2405	20	24	3.5

Table 2.2: Amplifier specifications. The Herotek amplifier was used initially, but was later replaced by the Lucix amplifier.

Mfr. Name, Model	Frequency Range	Coupling Factor	Directivity	Insertion Loss
Krytar, 152013	0.5-20 GHz	13±1.0 dB	>15 dB	<1.4 dB

Table 2.3: Coupler specifications

lent E8362B VNA to measure the frequency response of wireless channels over a frequency range of 2–18 GHz. The measurement setup is shown in Fig. 2-2. The subsequent sections describe the configuration of the measurement system in detail, the sources of error in the system, and the steps taken to mitigate them.

2.2.1 Configuration

The channel measurement subsystem makes use of two vertically polarized, omni-directional wideband antennas that radiate over a frequency range of 2–18 GHz. The azimuth and elevation antenna patterns are shown in Fig. 2-3. The antenna patterns indicate that the antennas have a very flat gain across their azimuth and a broad elevation beamwidth. The

Location	Mfr. Name, Model	Lengths (m)	Loss (dB/m) @ 18 GHz
Tx-VNA connection	Florida RF, LabFlex 290AW	25	0.656
Rx-VNA connection	Huber-Suhner, Sucoflex 104PE	5	1.6
Tx interconnections	Megaphase, Conformable Jumper CC141	0.10, 0.13, 0.33	2.17
Rx interconnections	Megaphase, SuperFlex SF26	0.30, 0.46, 0.76	1.55

Table 2.4: Cable specifications

gain, averaged over azimuth angle, as a function of frequency is shown in Fig. 2-4. The figure indicates that the average gain, relative to an isotropic radiator, of the transmit and receive antennas are closely matched and is nearly uniform over frequency (the variation is less than ±1 dB about the mean). The receive antenna is mounted on the positioning platform and connected to port 2 of the VNA. The transmit antenna is mounted to a tripod made of non-reflective composite materials and connected to port 1 of the VNA. Both antennas are located at a height of 1.43 m above the ground. Additional details about the antenna properties will be discussed in Sec. 2.2.2.

The measurement apparatus was designed to support a transmit and receive antenna separation of up to 25 m. This separation distance is reasonable for characterization of indoor environments in a single large room and between adjacent rooms. To overcome signal attenuation, the measurement system contains three amplifiers (specifications are listed in Table 2.2). Each amplifier is mounted to a heat-sink to dissipate heat and improve measurement stability. The measurement setup requires the transmitter and receiver to be connected. Thus, the transmit antenna and the VNA are connected by two 25 m low-loss cables. In the transmission path there are two amplifiers to overcome the loss of the 25 m cable and boost the power at the input to the transmit antenna. To account for drift and any other sources of error due to the amplifiers in the transmission path, a reference signal is coupled off the output of the last amplifier [38]. The coupling is achieved through the use a microwave directional coupler, whose complete specifications are given in Table 2.3. The output port of this coupler is connected to the transmit antenna. The coupled output port is fed through an identical 25 m low-loss cable and connected to the reference receiver on port 1 (the R1 input) of the VNA. This reference signal (as opposed to the internal reference) is used for all measurements. APC-7 connectors are used at the ends of the 25 m low-loss cables. These connectors mate to corresponding APC-7 panel mount connectors on the transmit antenna tripod and the channel characterization apparatus. This type of connector was chosen for its electrical repeatability and durability, since these connections are frequently disconnected and reconnected.

In the receive path, the output of the receive antenna is connected to an amplifier which serves to amplify the received signal that has been significantly attenuated due to propagation through the environment. The output of the receive amplifier is connected to a 5 m cable and then to port 2 of the VNA. The 5 m length is necessary because the cable

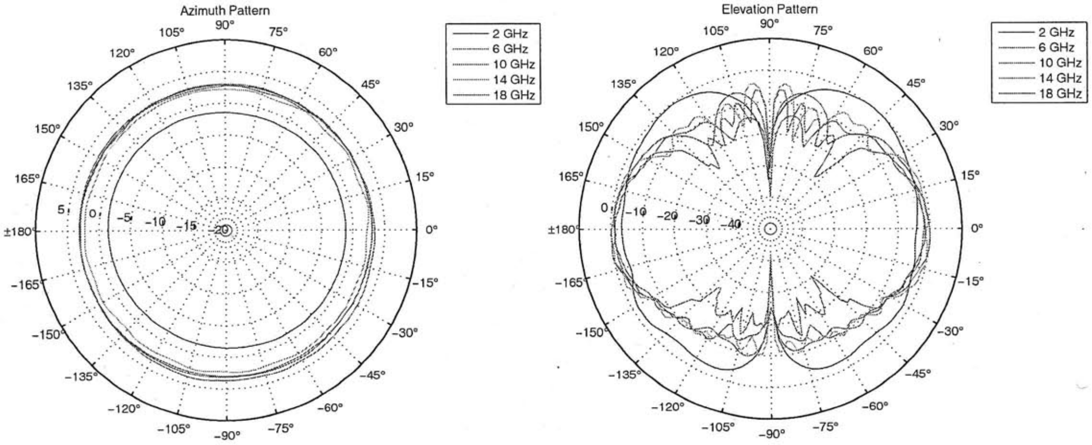

Figure 2-3: Azimuth and elevation patterns for the wideband antennas used by the channel measurement apparatus. Note that the azimuth pattern is extremely uniform and the elevation beamwidth is very broad at a particular frequency.

must be routed through each of the cable carriers. These cable carriers serve to protect the cable from the moving parts of the positioning subsystem. A summary of the cables used in the measurement setup, as well as their specifications is given in Table 2.4.

For each position of the transmit and receive antenna the VNA was used to measure the S21 parameter (B/R1), which represents the propagation channel from the transmit to the receive antenna. This measurement is determined by dividing the signal received on port 2 of the VNA (receiver B) by the reference signal (receiver R1). The S21 measurement, along with the R1 measurement, is then stored for later analysis.

2.2.2 Calibration

To achieve the most accurate measurements with a VNA, one typically has to use a full two-port calibration. Unfortunately, full two-port calibration is not possible because the amplifiers present in the measurement setup limit measurements in the reverse direction. Furthermore, all the required signals for two-port calibration are not available at the VNA. Thus, the calibration procedure reduces to a response calibration where the transmission response of various components in the measurement subsystem is measured and their effect is removed during post-processing. Additional details of the calibration procedure are discussed below.

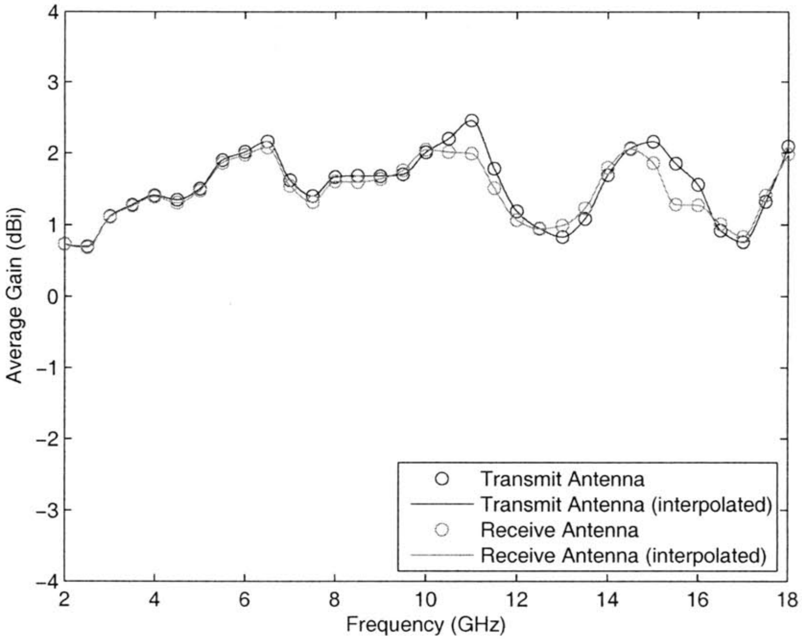

Figure 2-4: The manufacturer provided gain data of the antennas, averaged over azimuth angle, is within ±1 dBi of the average over frequency.

Source Power Calibration

First a source power calibration is performed at the cable feeding the transmit antenna. This ensures that the power level at the input to the transmit antenna is flat over the entire frequency band of interest. This improves the overall accuracy of measurements since the transmit antenna is supplied with a uniform power level. Power variations in the measurements would then be due to the transmit and receive antennas and the wireless channel. Source power calibration also helps to guarantee that the channel is being measured at with the highest available power.

The source power calibration is accomplished using a wideband power sensor (Agilent E4413A) connected to a power meter (Agilent N1911A) and proceeds as follows. The power sensor is connected to the cable which normally feeds the transmit antenna and the power meter is connected to the VNA via an ethernet cable. The power meter measures the power level incident on the power sensor and reports this information to the VNA. The VNA then makes adjustments to the source power level until the reading of the power sensor is within the desired range. The procedure then continues for each of the remaining frequencies. More details on the use of power meters and the source power calibration procedure can be found in [39, 40].

Transmission Response Calibration

A transmission response calibration is performed by directly connecting the cables feeding the antennas. This measurement includes the effect of all the components in the system, except for the antennas and the wireless channel. The result of this measurement is stored for later use. Errors introduced by the transmission amplifiers will be ratioed-out because of the coupled reference signal on the transmit side. The response calibration will then correct for frequency response errors and any mismatch associated with the coupler, cables, receiver-side amplifier, and the VNA. Before connecting the two antenna-feed cables, a 30 dB attenuator is inserted in the signal path. This prevents the receiver-side amplifier from getting saturated, but the effect of this attenuation must then be removed as part of the post-processing [38].

Antenna Calibration

The antenna calibration serves two purposes: 1) to precisely measure the path loss at a known distance in order to appropriately normalize the captured channel responses, and 2) to accurately characterize the effective transmit pulse that results from the transmitted signal passing through both antennas. The goal is to minimize the effects of the antennas on the measurements collected with the channel measurement apparatus.

As discussed earlier, the positioning subsystem allows for positioning of the receive antenna along any path. In order to accurately characterize the response of the pair of antennas, numerous orientations of the pair must be considered. With this in mind, the positioning subsystem was configured to measure points along arcs. The transmit antenna was placed near one of the four corners of the positioning subsystem and the receive antenna's position was varied along an arc with a radius of 1 m centered at the transmit antenna's position. Each arc contains eight positions for the receive antenna, and at each position ten measurements were made. The process was then repeated at the other three corners while keeping the transmit antennas angular orientation constant (i.e., the antenna was not rotated). In all, $4 \times 8 \times 10 = 320$ measurements were made and stored for subsequent processing. A diagram depicting the arrangement of the transmit antenna and receive antenna positions during the measurement process is shown in Fig. 2-5. This procedure systematically captures responses at many of the possible orientations of the pair of antennas and

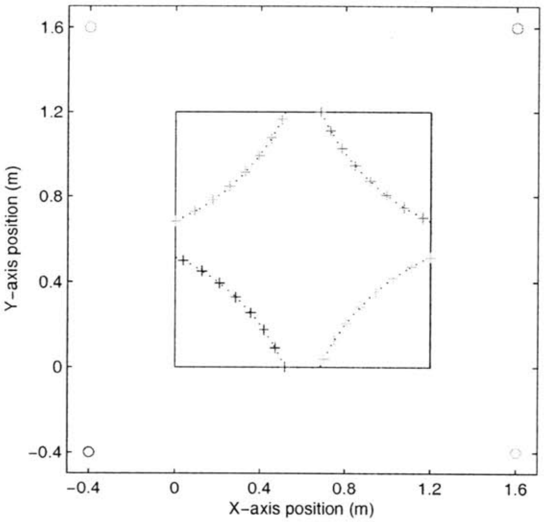

Figure 2-5: The measurement layout for the antenna calibration procedure. Circles indicate the position of the transmit antenna and crosses indicate the position of the receive antenna along arcs with a radius of 1 m. The large black square indicates the positioning area of the channel characterization apparatus.

gives a good approximation of the true response of the pair of antennas.

The stored responses were then processed as follows: 1) the ten responses measured at each position were averaged, this reduces any noise present in the system, 2) these average responses are then windowed in the time domain[1] to select only the direct path, and 3) these windowed responses are then aligned in time by detecting the dominant peak, and averaged to produce a single averaged, windowed response. The time-domain windowing is necessary to remove additional paths caused by reflections in the environment.[2] The magnitude and phase of the resulting response is shown in Fig. 2-6 and the time-domain response is shown in Fig. 2-7. The resulting frequency response can then be used to normalize the frequency responses of the subsequent measured channels. The time-domain response is also used as the template transmit pulse in the channel parameter extraction algorithm (see Sec. 3.4.3).

The antennas also introduce a delay in the captured channel realizations. Removing this delay is very important when using the data to investigate ranging performance. This delay can be estimated by measuring the antenna return loss (i.e., S11 at the antenna input). The magnitude and phase of the return loss are reported in Fig. 2-8. From the measured data, we see that the phase is approximately linear, corresponding to a constant group delay. The group delay of this measurement corresponds to the amount of time it takes a

---

[1] A time-domain, raised-cosine window was used with roll-off factor $\beta = 0.25$ and $T = 625\,\text{MHz}$.

[2] These steps are necessary since an anechoic chamber was not readily available.

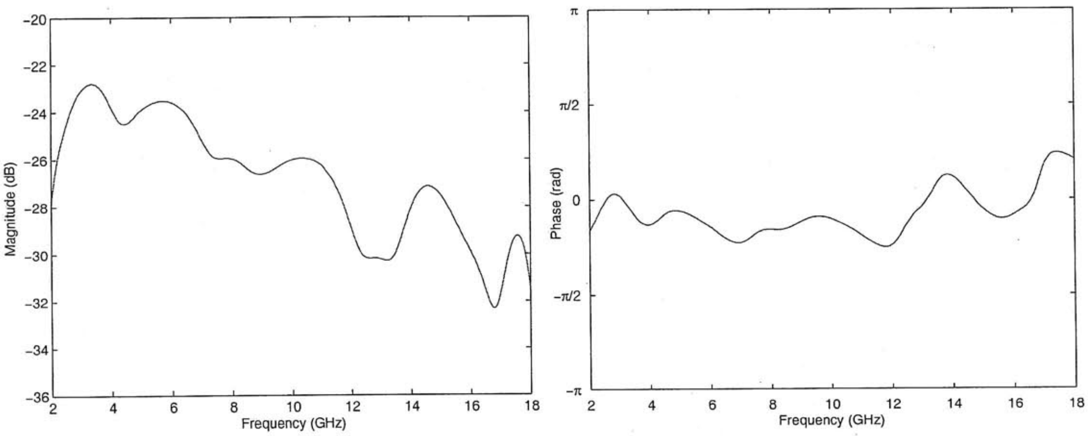

Figure 2-6: Magnitude and phase of the average response of the pair of antennas at a distance of 1 m.

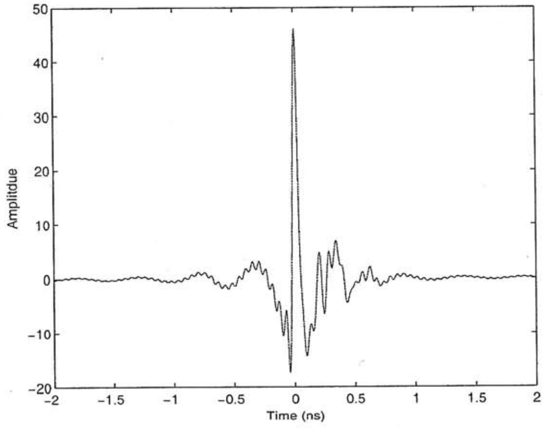

Figure 2-7: Passband impulse response of the pair of antennas, resulting from the calibration procedure described in Sec. 2.2.2.

signal to travel into the antenna and back out of the input. Thus, half the group delay is a reasonable estimate of the delay introduced by the antennas. Performing a linear best-fit on the phase data yields the following delay estimates:

$$\hat{\tau}_{\text{Tx Ant}} = 0.824\,\text{ns}$$

$$\hat{\tau}_{\text{Rx Ant}} = 0.698\,\text{ns}$$

for the transmit and receive antennas, respectively.

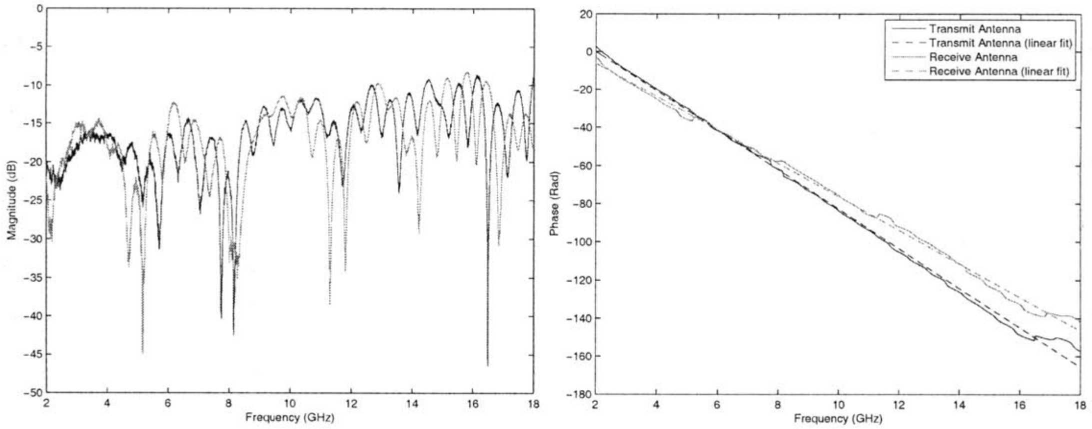

Figure 2-8: Magnitude and phase of the reflection coefficient (S_{11}) of the antennas used in the channel measurement apparatus. Note that the magnitude is approximately less than $-10\,\mathrm{dB}$ and the phase is nearly linear.

2.2.3 Measurement Accuracy

There are many factors which affect the accuracy of the channel measurement subsystem. The calibration steps discussed above are taken to maximize accuracy of the captured channel realizations, but some sources of error are unavoidable. Below we list these error sources and describe their effect on the measurements.

Antenna response is a function of azimuth and elevation angle

Signal propagation paths originate from the transmit antenna and terminate at the receive antenna at specific azimuth and elevation angles. While the response of the antennas is relatively uniform as a function of azimuth angle, there is a large variation with elevation angle (see Fig. 2-3). Ideally, we would like to correct for the magnitude and phase changes that each of these paths undergo. While it is feasible to measure the antenna response at all possible azimuth and elevation angles, it is difficult to determine the exact angles corresponding to each propagation path in an experimental setting. This makes it challenging to remove the effect of the antenna on each arriving path. Instead, when removing the response of the antenna from the measurements, we will use the average antenna response measured at a distance of 1 m (estimated using the procedure described earlier).

Amplifier characteristics drift as temperature changes

Typically, the gain of an amplifier is reduced as the amplifier's temperature increases to its steady-state value. Thus, if calibration measurements are made under different conditions than the conditions under which data is collected, errors could be introduced. These effects can be eliminated by using a reference signal, as is used in the transmission path of the measurement system described here. When a reference signal is not possible, the effects can be minimized by waiting until all components reach their normal operating temperatures. Furthermore, calibration measurements should also be made under operating conditions that are identical to those for the data collection. In our case all calibration measurements were performed at normal operating temperatures to avoid any effects due to the receiver-side amplifier.

Connector repeatability and cable flexure introduce measurement variations

Connector repeatability refers to changes in measurements that occur when connectors are disconnected and reconnected. If a connector has low repeatability, there will be large variations between measurements. The measurement system makes use of APC-7 connectors wherever connectors are frequently disconnected, namely at both ends of the two 25 m cables. It is generally accepted that these connectors have the highest repeatability of all connectors in the 2–18 GHz range.

Measurement variations also occur when cables are flexed. Normally, these variations can be avoided by limiting the movement of cables in a measurement setup. For the measurement apparatus discussed here, this is not possible for two reasons. First, as the position of the receive antenna is varied, the cable connecting the receive antenna to the VNA, which is routed through two cable carriers, is flexed. Second, the position of the two 25 m cables can only be kept constant during a single set of measurements. When the measurement apparatus is moved to a new location the cables must be repositioned. Furthermore, the position of these cables must be changed when making the transmission response measurements for calibration purposes and when collecting data. During informal tests, the effects of cable flexure and connector repeatability were shown to be small.

Receive SNR at the VNA

The accuracy of measurements made by the VNA is affected by the SNR of the input signal. Noise present in the signals at the input of the VNA receivers can causes degradation in the measurement accuracy. The amplifiers present in the transmission chain attempt to increase the transmit power and thereby improve the SNR of the received signal. If we were only interested in measurements over a narrow frequency range, it would be possible to further increase the SNR, since high-powered narrowband amplifiers are readily available. In a wideband channel, regardless of the transmit power, there will always be multipath components that arrive at large excess delays in the measured channel realizations. These paths will experience significant path loss and therefore arrive at the VNA with very low SNR, making it difficult for the VNA accurately measure them.

2.2.4 Summary

In summary, the channel measurement subsystem was designed to accurately measure extremely wideband channels. Many steps were taken to mitigate the impact of all sources of error in the system, but it is impossible to completely remove these errors. The steps taken include the use of a reference channel in the transmission path to mitigate effects caused by amplifier variations, use of highly repeatable connectors, precise calibration of the transmit power using source power calibration, and a systematic procedure to capture an accurate average antenna response.

2.3 Computer Automation

Both the positioning subsystem and the channel measurement subsystem are linked via computer to enable fully automated antenna positioning and collection of channel realizations. The two motor controllers of the positioning subsystem are connected via an RS-485 serial interface to an RS-485–ethernet serial server (B&B-Electronics Mfg. Co., ESR901). The serial server and the VNA are connected to a local ethernet network. Also part of this network is a computer, referred to as the *host computer*, that runs MATLAB code to control all the equipment. Typically the host computer is a laptop that is located away from the immediate measurement environment, but there are essentially no restrictions on its exact location.

The MATLAB code running on the host computer is responsible for several tasks. First, the code calibrates the positioning subsystem and configures the VNA, setting measurement parameters and loading calibration data. At this point the user also selects the coordinates for each of the measurement points (i.e., the measurement grid), and the name of the file in which the measurement data will be stored. The basic measurement procedure is as follows: 1) the antenna is positioned to the correct coordinates; 2) the VNA measures the channel realization; 3) the measurement data is transmitted to the host computer and stored in a custom binary format. This binary format is necessary to overcome limitations in MATLAB's built in .mat format when storing large amounts of data on low-end computers. The format allows saving and loading individual measurements without requiring the whole set of measurements to be loaded into memory, thereby reducing memory requirements.

The next subsections give details about the MATLAB code that runs on host computer, the data storage format, and how to access the data after the experiment is complete.

2.3.1 Positioning and Channel Measurement Subsystems Control Software

The positioning subsystem control software was developed using object-oriented programming in MATLAB. The software consists primarily of two classes: pt_axis and positioning_table. The object-oriented nature allows for extending the software to control additional axes if the system is expanded in the future.[3] The constructor for the positioning_table class takes as arguments, among others, a number of pt_axis objects. The classes contain methods for setting up parameters for the axes, moving the axis, determining the position, and checking the error status of the underlying motor controllers. A key part of the pt_axis class is that it is responsible for the translation of MATLAB commands into the commands sent over the serial interface to the motor controllers. Details of the complete command set are available in [41].

The channel measurement subsystem control code makes use of Standard Commands for Programmable Instruments (SCPI) and the Instrument Toolbox in MATLAB. Complete documentation of all the commands available for controlling Agilent network analyzers is available in [39].

---

[3] For example, one might consider the addition of a rotary stage on the top axis to control the angle of a directional receive antenna.

2.3.2 Software and Data Organization

This section briefly describes how the positioning and channel measurement subsystems software, raw data, and processed data are organized. In the root directory there are four sub-directories:

- **cals:** This directory contains calibration information for the channel measurement apparatus. There are two sub-directories: 1) Antennas, and 2) Measurement Subsystem. The Antennas sub-directory contains gain and S11 measurements for the antennas, as well as response data for the antennas collected at a distance of 1 m. The Measurement Subsystem sub-directory contains S21 measurements for the different configurations of the apparatus. There are also measurements for the 30 dB attenuator used during the calibration procedures.
- **code:** This directory contains code for running the measurement apparatus, as well as code for storing, reading, calibrating, and processing measurement data. The directory also includes the sub-directory xy_code which contains the code for running the channel measurement apparatus.
- **pool:** This directory contains the raw data stored by the measurement apparatus. As will be described later there are two files for each measurement location; the results parameter file and the results data set file. The name for the data files uses the following simple structure "⟨MIT building⟩-⟨MIT room number⟩_Loc_⟨location index⟩"; for example measurements taken at location A in room 32, building D650 use the file name "32-D650_Loc_A".
- **pool processed:** This directory contains sub-directories for the processed measurement data, one directory for each type of processing that is done on the data. For example, data that has been processed using the search-subtract-readjust algorithm (described in Sec. 3.4.3) to extract path amplitudes and delays is in the SSR sub-directory.

2.3.3 Data Storage Format and Low-level Access Functions

A set of measurements from a measurement grid is stored in two files: the *results parameter file*, a .mat file which can be directly opened in MATLAB, and a corresponding *results data set file* with the extension .bin. The results parameter file contains details of the

Name	Description
filename	Full path of the file, as it was written by the host computer
location_info	A string used to describe general information regarding where the measurements were captured
results_info	A string used to describe the specific position where the measurements were captured along with other information about this particular data set
pt_param	Structure containing parameters for the positioning subsystem, details are given in Table 2.6
instr_param	Structure containing parameters for the channel measurement subsystem, details are given in Table 2.7
last_grid_pt	The last point measured in the measurement grid
fpoints	instr_param.n_fpoints × 1 vector of frequencies (in Hz) at which the channel measurement subsystem measures the frequency response
timestamp	Date and time when the measurements were collected

Table 2.5: Description of the contents of the results parameter (.mat) file used to store parameters of the measurements

particular experiment, as well as configuration parameters for the positioning and channel measurement subsystems. The results data set file consists of binary data records—one record for each captured channel realization.

The results parameter file contains seven variables that describe details of the measurements, as well as particular configuration settings for the positioning and channel measurement subsystems. These variables are described in Table 2.5. Of particular interest are the pt_param and instr_param structures which are described in Tables 2.6 and 2.7, respectively. During the measurement process these two structures are used to set up the channel measurement apparatus, ensuring that the state of the hardware is the same across all measurement locations.

Name	Description
n_grid_points	Number of points in the measurement grid
n_axes	Number of axes which can be positioned
grid_points	n_grid_pts × n_axes matrix containing coordinates in the positioning grid where channel realizations will be captured
coords	Structure containing three coordinates: tx_coord is the position of the transmitter for this set of measurements, rx_coord and rx_coord2 are coordinates of the measurement apparatus

Table 2.6: Description of the pt_param structure that is used to store positioning subsystem parameters

Name	Description
FStart	First frequency of the frequency response
FStop	Last frequency of the frequency response
n_fpoints	Number of frequencies to measure between FStart and FStop
IFBW	IF bandwidth
parameters	A list of parameters to be measured by the VNA and then stored by the host computer. These parameters appear as traces on the VNA.
FOM	If FOM=1 indicates that frequency offset mode should be used
SPC	If SPC=1 indicates that source power correction data should be applied
spc_data	Data for source power correction, determined during the source power calibration procedure
spc_offset	Offset for source power correction
S21cal	Default calibration data, applied when calibrating the stored measurement data

Table 2.7: Description of the instr_param structure that is used to store channel measurement subsystem parameters

The results data set file is a binary file consisting of data records, one for each captured measurement, stored sequentially. Each data record consists of six separate fields which are described in Table 2.8. Since each data record is of constant length, and this length can be calculated from parameters in the corresponding results parameter file, it is easy to quickly access a particular data record. The binary data is stored in little-endian byte ordering. It is necessary to specify the endian directly because the computer which initially stores the data may have a different architecture than the computer on which the data is accessed.

Utility functions are provided for writing the results parameter file, as well as for writing and reading data records from the results data set files. Since the results parameter file is a .mat file, it can be opened directly using the MATLAB load command. Details of the three utility functions are given below.

write_results_param

write_results_param(filename_mat, filename_bin, results_info, location_info, pt_param, instr_param, fpoints, last_grid_pt)

Writes the parameters of a results data set: results_info, location_info, pt_param, instr_param, fpoints, and last_grid_pt, to the results parameter (.mat) file using the MATLAB save command. For details on the contents of the file see Table 2.5.

get_results_dataset

drec = get_results_dataset(filename, pt_param, instr_param, idx)

Name	Type	Size (bytes)	Description
pt_indx	uint32	4	Index of the point in the measurement grid
pt_seq	uint32	4	Point sequence, used when multiple measurements are made at the same position
pt_time	double	8	Time at which the measurement was made
pt_desired	double	8 × pt_param.n_axes	Coordinates of the location for the desired measurement
pt_measured	double	8 × pt_param.n_axes	Coordinates for the measurement as returned by the positioning table
data	double	2 × length(instr_param.parameters) × instr_param.n_fpoints	Measurement data, stored as 2 × n_fpoints vector of doubles for each parameter measured by the VNA

Table 2.8: Specifications for the binary record format used when storing the measurement data in the results dataset (.bin) file

Reads record number idx from filename and returns a data record structure with fields as specified in Table 2.8. The parameters pt_param and instr_param, which are available in the corresponding results parameter (.mat) file, are structures that are used to determine the size of the data records. An error occurs if you attempt to access a record number greater than the length of the data file.

write_results_dataset

write_results_dataset(filename, pt_param, instr_param, pt_indx, pt_seq, pt_desired, pt_measured, data, idx)

Writes a binary data record to filename. As in read_results_dataset, the parameters pt_param and instr_param are used to determine the size of the data records. First, write_results_dataset seeks to the entry idx and then writes the record. When idx=-1 data is appended to the end of the file, otherwise record number idx is *overwritten*. An attempt to write to a record beyond the length of the file will generate an error. The parameters pt_idx, pt_seq, pt_desired, pt_measured, data are described in Table 2.8.

2.3.4 Accessing Calibrated Data

Calibrated channel realizations can be accessed using the functions open_exfile and postprocess. In order to access calibrated data, the following steps must be performed:

1. Open the desired data set using the open_exfile function. This returns a results parameter structure (with the same contents as the results parameter file described above) and a post-processing structure; and
2. Retrieve a calibrated channel realization from the opened data set using the postprocess function.

If multiple channel realizations are required from a given data set, the data set need only be opened once—the same post-processing structure can be used to retrieve all channel realizations in a particular data set at the same frequency range. This can save considerable computational time when accessing a large series of channel realizations. The open_exfile and postprocess functions are described in detail below:

open_exfile

`[rs, pp] = open_exfile(filename, varargin)`

Opens an experiment file, creates the necessary post-processing structure, and returns a results parameter structure (rs) along with the post-processing structure (pp). All arguments in varargin are passed directly to the make_pp_struct function. Based on the contents of filename this function determines the measurement location, sets the coordinates of the measurement location in the pt_param structure,[4] determines which calibration file to apply, and then calls the make_pp_struct function.

make_pp_struct

`pp_struct = make_pp_struct(res_struct, S21cal, varargin)`

This function is responsible for making the appropriate post-processing structure based on the measurement location and the optional frequency range specification set in varargin. The input parameter res_struct is a results parameter structure and the parameter S21cal is the S21 calibration data for the measurement subsystem to apply to the measurements for this experiment. If the varargin option is present, it is expected to consist of two frequency values in Hz; a starting value and a stopping value. These values must be within the range

---

[4] Although the pt_param structure present in the results parameter file for a particular measurement location contains coordinates for the measurement, in general the exact values of the coordinates were not known until after the measurement process, therefore they must be set correctly when opening the file.

over which the measurement data was originally collected. The corresponding starting and stopping indices in the res_struct.fpoints vector are computed and then used when creating the post-processing structure. The resulting post-processing structure consists of several fields which are described in Table 2.9.

postprocess

[x, y, drec] = postprocess(pp_struct, file, res_struct, ptidx, varargin)

This function is responsible for applying the final calibration data to a measurement and returning it in the desired form. Depending on the options specified, either time-domain or frequency-domain data is output and x and y will be set appropriately. For example, if time-domain data is desired x will correspond to the sampling instants and y will correspond to the time-domain amplitude samples. The input parameter pp_struct (returned from open_exfile) is a post-processing structure, containing the necessary data to perform proper calibration and post-processing. file specifies the file to read raw data from. res_struct is a results parameter structure which is also returned from open_exfile. The final parameter varargin contains optional arguments, which can include:

- time: produce time-domain data. The data will be real valued unless the baseband option is also specified.
- freq: produce complex-valued frequency-domain data.
- baseband: produce baseband data for the time-domain, has no effect if freq is specified above.
- nowindow: do not window the data, default is to window the data using a root-raised cosine function in the frequency domain.
- noantcal: do not calibrate for the magnitude and phase effects of the antennas.
- noantdelaycal: do not remove the delay introduced by the antennas.

If no options are specified, the default is to return windowed, and fully calibrated frequency-domain data.

Name	Description
fstart_idx	Index into res_struct.fpoints corresponding to the minimum frequency in the range of interest
fstop_idx	Index into res_struct.fpoints corresponding to the maximum frequency in the range of interest
fpoints	The frequencies in the range of interest, fpoints=res_struct.fpoints(fstart_idx:fstop_idx)
ant_cal	Calibration data for the combined response of the two antennas. This data is based on several measurements made by the channel measurement subsystem when the antennas were 1 m apart.
ant_delay_cal	Calibration data for the delay introduced by the antennas, based on the S11 measurement of each antenna.
meas_cal	Calibration data for the measurement subsystem, created by measuring the S21 parameter when the cables feeding both antennas are directly connected
window	The frequency response of a root-raised cosine window used if windowed data is desired

Table 2.9: Description of the instr_param structure that is used to store channel measurement subsystem parameters

Chapter 3

Measurement Campaign

Channel realizations were collected around the Laboratory for Information and Decision Systems on the 6th floor of the Ray and Maria Stata Center using the measurement apparatus described in Chapter 2. In this chapter we describe the measurement methodology, locations where measurements were collected, and the post-processing done prior to analysis of the data.

3.1 Measurement Parameters

Channel realizations were captured over a frequency range of 2–18 GHz, for a maximum bandwidth of 16 GHz. The VNA was set to capture the maximum number of points within these limits ($N_\mathrm{f} = 20001$), and operates by sampling the frequency response to produce N_f complex samples. This value of N_f, along with $f_\mathrm{min} = 2$ GHz and $f_\mathrm{max} = 18$ GHz, leads to a frequency sampling interval of

$$\Delta f = \frac{f_\mathrm{max} - f_\mathrm{min}}{N_\mathrm{f} - 1} = 0.8\,\mathrm{MHz}\,.$$

Using duality and ideas from time-domain sampling, one can understand the limitations of frequency sampling with a particular Δf. Sampling a frequency-domain signal at Δf will result in a periodic time-domain signal with period $1/\Delta f$. Wideband channels are characterized by dispersion known as multipath propagation. We denote the difference in delays between the first and last arriving multipath components as τ_max. One must ensure that Δf is small enough to guarantee that $\tau_\mathrm{max} < 1/\Delta f$, to avoid overlap of the time-domain replicas. A resolution of $\Delta f = 0.8\,\text{MHz}$ gives a maximum excess delay of 1250 ns, corresponding to a maximum distance range of 375 m.

Other important parameters of the measurements include the power calibrated at the input to the antennas and the IF bandwidth. The power calibrated at the input of the transmit antenna, using the source power calibration capability of the VNA, was $+16 \pm 0.1\,\text{dBm}$. The IF bandwidth of VNA was set to 10 kHz. The selection of a 10 kHz IF bandwidth gives a good performance / measurement speed trade-off; with this setting it takes approximately 10 s to measure each channel realization. Decreasing the IF bandwidth would lower the noise floor of the VNA, but will increase the measurement time.

3.2 Measurement Locations

The measurement campaign was carried out on the 6th floor of the Dreyfoos tower of the Stata Center on the MIT campus. This location was chosen because of its similarity to a large indoor office environment, and its proximity to the Wireless Lab, where the measurement apparatus was developed. The measurement area incorporates a variety of materials and propagation conditions, including concrete pillars, glass walls with aluminum frames, galvanized steel support beams, and wall coverings such as drywall and plywood. The floor plan of the environment is shown in Fig. 3-1.

Channel realizations were captured in a number of different locations in the measurement area. These specific points, referred to as *global points*, indicate the precise location of the measurement apparatus. The exact points where the receive antenna was located are referred to as the *local points*. The collection of local points associated with a global point, is referred to as a *local set*. The global points were chosen to provide good coverage of the measurement area, without any overlap of the local sets. Each of the global points are assigned a letter (A-U). The set of measurements collected at a particular global point, for example location A, is denoted as $\mathcal{H}^{\text{A}}$.

The majority of the measurement locations were located in the 6th floor lounge area (32-D650). Additional measurements were collected in the adjoining hallways near 32-D608 and 32-D675, and in the Wireless Lab (32-D675). In all, 21 sets of measurements were captured. The details of each measurement location, including coordinates, orientation, and propagation conditions, are given in Table 3.1. The next section describes the local

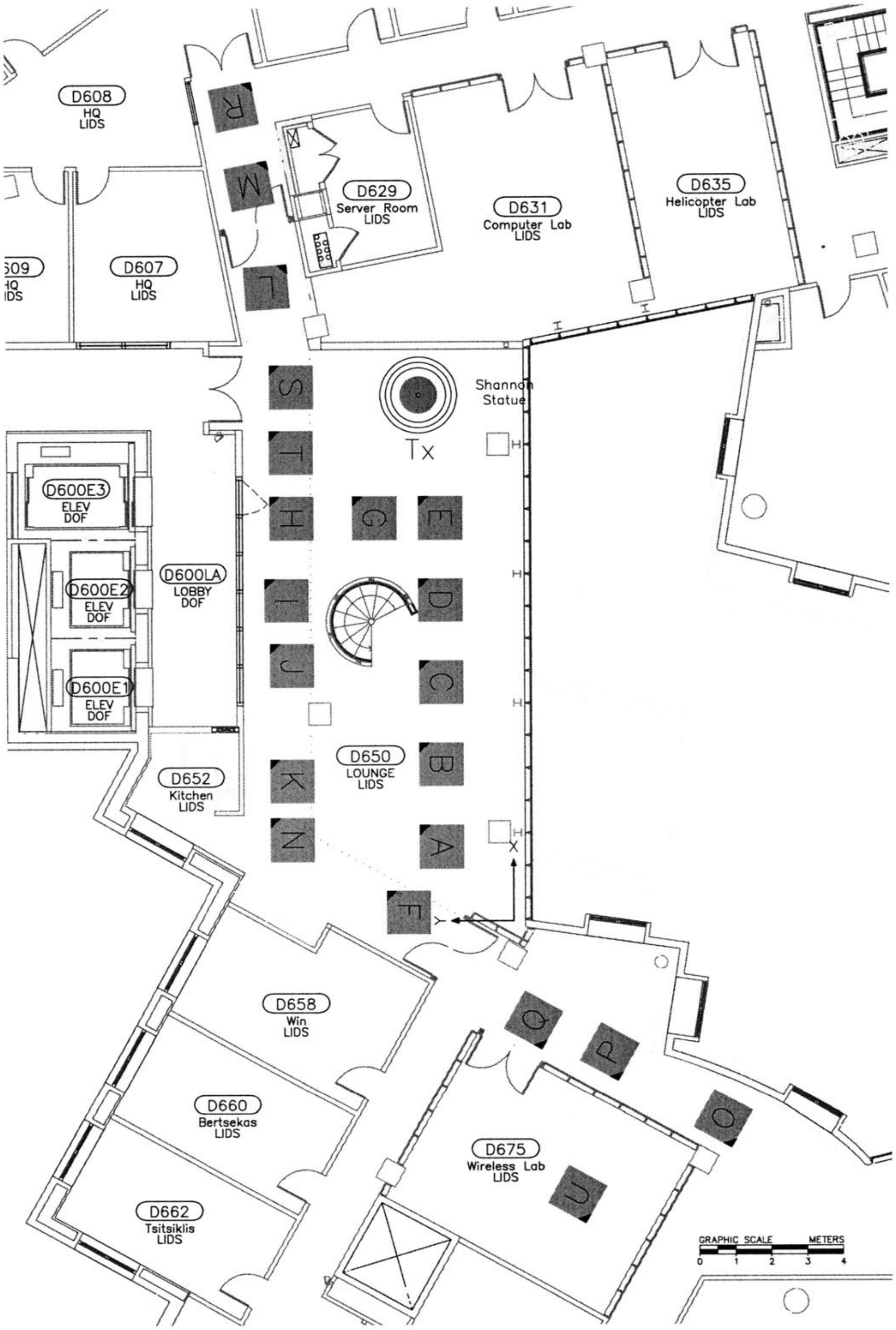

Figure 3-1: Measurements were made on the 6th floor of the Dreyfoos tower of the Ray and Maria Stata Center. The blue squares indicate the locations where channel responses were captured (in each location the black triangle depicts the origin of the measurement grid). In all, measurements at 21 locations were captured.

Location	Coordinates (m)	Orientation	Distance (m)		Conditions
			Min.	Max.	
A	(2.658, 2.580)	180°	12.073	13.346	LOS
B	(4.955, 2.584)	180°	12.124	13.503	LOS
C	(7.239, 2.579)	180°	12.555	14.090	LOS
D	(9.531, 2.591)	180°	13.356	14.993	LOS
E	(11.822, 2.591)	180°	14.488	16.182	LOS
F	(0.832, 3.504)	180°	11.286	12.724	LOS
G	(11.822, 4.417)	180°	13.007	14.720	LOS
H	(11.822, 6.710)	180°	11.292	13.015	LOS
I	(9.530, 6.854)	180°	9.680	11.387	LOS
J	(7.700, 6.706)	180°	8.854	10.502	Mixed
K	(4.495, 6.710)	180°	7.974	9.365	NLOS
L	(18.314, 6.218)	94°	16.171	17.849	NLOS
M	(21.196, 6.762)	101°	18.526	20.216	NLOS
N	(2.664, 6.708)	180°	7.945	9.239	NLOS
O	(-6.411, -6.034)	-29°	21.339	22.706	NLOS
P	(-4.503, -2.900)	-29°	17.715	19.115	NLOS
Q	(-3.604, -0.776)	-29°	15.409	16.817	NLOS
R	(23.403, 7.191)	101°	20.449	22.116	NLOS
S	(15.482, 6.702)	180°	14.134	15.828	LOS
T	(13.649, 6.714)	180°	12.653	14.367	LOS
U	(-8.543, -1.986)	-29°	18.728	20.016	NLOS
Transmitter	(2.584, 14.653)				

Table 3.1: Details of the measurement locations. Coordinates are given with reference to the origin shown in Fig. 3-1, the orientation angle is measured in a counter-clockwise direction from the x-axis of the origin to x-axis of the positioning grid, and the reported distances are with respect to the location of the transmitter (2.584, 14.653).

grid on which measurements were collected.

3.3 Measurement Grid

The grid over which measurements were captured was designed to enable the analysis of many phenomena, while at the same time keeping the total measurement time per grid manageable. The grid, which can be seen in Fig. 3-2, is multiscale in nature, that is, it contains several grids with different spacing. The first part of the measurement grid was designed to maximize the number of uncorrelated measurements that can be taken for each location of the positioning platform. In order to minimize correlation, it is recommended that measurements be taken at separations greater than $\lambda_{\max}/2 = c/(2f_{\min})$, where $\lambda_{\max}$ is the largest wavelength [42]. However, the antenna should also not overlap the space occupied by the antenna when it is in adjacent measurement locations. Thus,

$$d_{\text{sep}} = \max\{\lambda_{\max}/2,\ d_{\text{ant}}\} \tag{3.1}$$

where d_{ant} is the diameter of the antenna. For this measurement campaign $\lambda_{\max} = 150\,\text{mm}$, so $d_{\text{sep}} = d_{\text{ant}} = 101\,\text{mm}$. In order to fit the maximum number of measurements in the square measurement grid we used a circle packing arrangement, giving 188 measurements. We refer to this grid as the *main grid* and denote the measurements captured on that grid as $\mathcal{H}_0$. In addition to the 101 mm circle-packing grid, the grid also contains two sub-grids with finer spacing, for future investigations. The first sub-grid, located in the center of the measurement platform is a $d_{\text{sep}}/2 = 50.5\,\text{mm}$ circle-packed grid containing 187 points (141 of which do not coincide with the main grid). This grid is referred to as the *center sub-grid.* The second sub-grid consists of 7 × 7 square grids of points with spacing $\lambda_{\min}/2 = 8.33\,\text{mm}$ located at the four corners of the main grid. This grid is referred to as the *corner sub-grid.* The three grids combined give a total of 525 points, which can be measured in less than 2.5 hours. The points in each grid are measured from the lower left corner to the upper right corner. The two circle-packed grids are measured first, followed by the four square grids. Throughout this thesis the analysis will focus on measurements collected on the main grid ($\mathcal{H}_0$). The data collected in the additional sub-grids will be used to support future investigations.

3.4 Data Processing

This section describes the processing that is performed on the calibrated data prior to its use in evaluating the performance of wireless systems in subsequent chapters. Next we describe the set of possible center frequency–bandwidth pairs which define the frequency bands at which the data can be observed. Then, Sec. 3.4.2 discusses how the time-domain waveform is computed from the frequency-domain data. Finally, Sec. 3.4.3 describes the method used for extracting path delays and gains from wideband channels.

3.4.1 Center Frequency–Bandwidth Domain

As discussed earlier the measurements were captured in a variety of locations over the frequency range 2–18 GHz. This wide frequency ranges allows for the investigation of

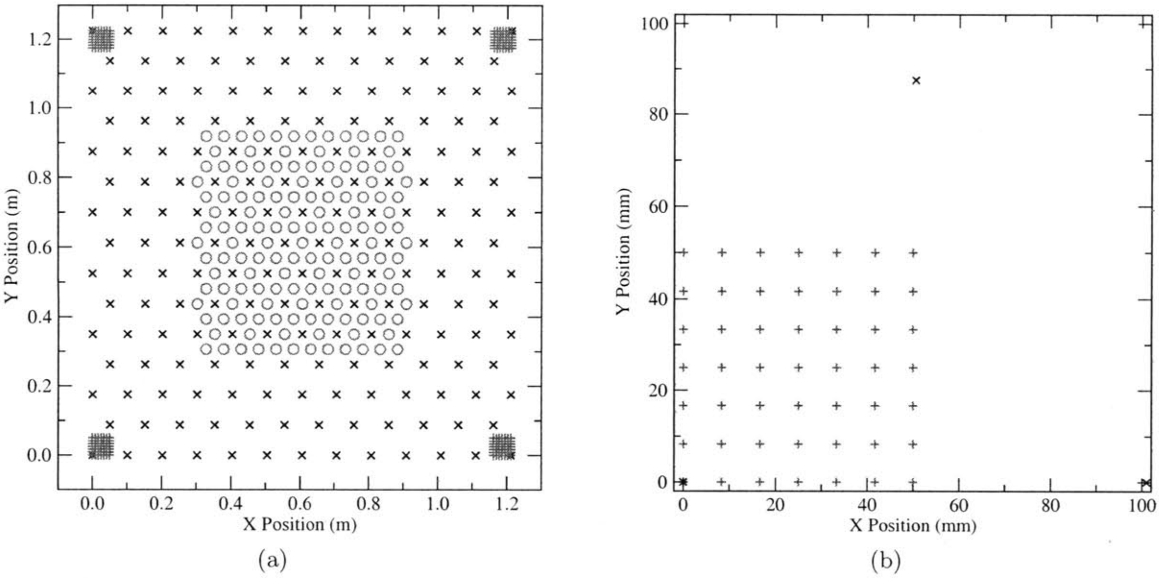

Figure 3-2: (a) The overall measurement grid: blue crosses make up the outermost grid of uncorrelated points, magenta circles make up an inner denser correlated grid, and green pluses make up small dense grids in the corners. (b) A detailed view of the lower left corner, showing the 49 points that make up this portion of the grid.

properties over different bandwidths and center frequencies. However, the range of possible bandwidths depends on the particular center frequency. Given a particular center frequency, $f_{\mathrm{c}} \in (f_{\min}, f_{\max})$, the bandwidth W must satisfy

$$W \leq \min\left\{2(f_{\max} - f_{\mathrm{c}}),\, 2(f_{\mathrm{c}} - f_{\min})\right\} . \tag{3.2}$$

This, combined with the fact that we are interested in $W > 0$ defines a triangular region for the domain of possible pairs of center frequency and bandwidth (f_{c}, W). This region is indicated in Fig. 3-3. For each point in the triangular region, a different waveform can be extracted from a single captured channel response (details of the extraction procedure are given below). To limit the number of possible waveforms, the triangular region was sampled on a rectangular grid with $\Delta f_{\mathrm{c}} = 2\,\mathrm{GHz}$, $\Delta W = 1\,\mathrm{GHz}$. Only the resulting set of 64 discrete pairs, denoted as $\mathcal{S}_{\mathrm{s}}$, will be considered in the subsequent analyses. These points are indicated by crosses in Fig. 3-3.

Throughout the thesis we will denote the resulting set of waveforms from a measurement location observed at a set of frequency bands (specified by the center frequency–bandwidth pairs $\mathcal{S}_{\mathrm{s}}$) as the set $\mathcal{H} \circledast \mathcal{S}_{\mathrm{s}}$. For example, the set of channel realizations collected on the main

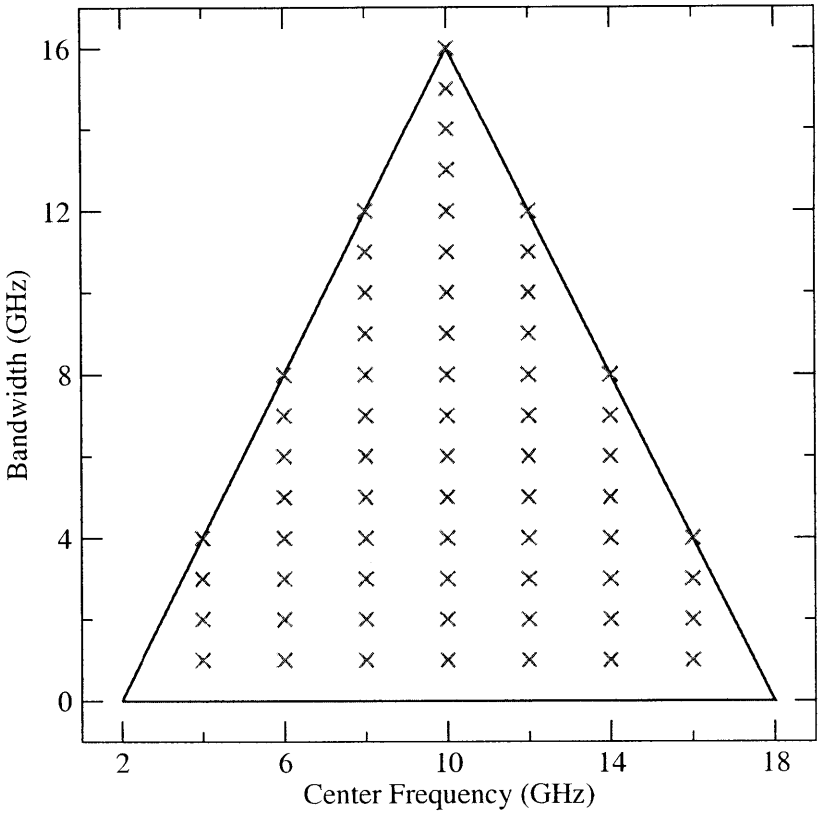

Figure 3-3: The set of possible center frequency and bandwidth pairs. The crosses indicate the discrete pairs that were considered ($\mathcal{S}_\mathrm{s}$).

grid at location A and observed at all center frequency–bandwidth pairs is given by the set $\mathcal{H}_0^\mathrm{A} \circledast \mathcal{S}_\mathrm{s}$. Note that $\left|\mathcal{H}_0^\mathrm{A} \circledast \mathcal{S}_\mathrm{s}\right| = \left|\mathcal{H}_0^\mathrm{A}\right| \times \left|\mathcal{S}_\mathrm{s}\right|$. The next section describes the procedure for extracting a waveform observed at a particular frequency band of interest.

3.4.2 Computation of the Time-Domain Representation

One of the strengths of frequency domain characterization is the ability to quickly generate time-domain responses for different frequency bands of interest. This enables an investigation of system and channel behavior at different transmission bandwidths. In this section details of the process for extracting waveforms in a particular frequency band are given along with some considerations.

Let the N_f frequency-domain samples from the VNA be given by $X_0, X_1, \ldots, X_{N_\mathrm{f}-1}$ with corresponding frequencies $f_0, f_1, \ldots, f_{N_\mathrm{f}-1}$. One way to form a time-domain version of the response is to perform an inverse discrete Fourier transform (IDFT), typically computed using the fast Fourier transform (FFT) algorithm, on the frequency-domain data.

Real Passband

In order to produce the time-domain signal with the proper frequency content, it is necessary to zero pad the frequency-domain samples:

$$\boldsymbol{Y} = [\mathbf{0}_L,\, \boldsymbol{X},\, \mathbf{0}_M]\,, \tag{3.3}$$

where $\boldsymbol{X} = [X_0,\, X_1,\, \ldots,\, X_{N_\mathrm{f}-1}]$ and $\mathbf{0}_L$ is an L-element vector of zeros. The value of L is given by $\lceil f_\mathrm{min}/\Delta f \rceil$ and serves to preserve the frequency offset of the measured data. If $f_\mathrm{min}/\Delta f$ is not an integer, it is necessary to account for the error in the frequency offset in the resulting time-domain data.[1] For efficiency in the computation of the IDFT, M should be chosen so that N, the length of Y, is a power of two. The resulting time-domain signal is $\boldsymbol{y}$, where [43]

$$y_n = \frac{1}{\sqrt{N}} \Re\left\{ \sum_{k=0}^{N-1} Y_k e^{j2\pi(nk/N)} \right\}, \quad n = 0, 1, \ldots, N-1\,. \tag{3.4}$$

Complex Baseband

In this case the vector $\boldsymbol{Y}$ is given by

$$\boldsymbol{Y} = \begin{cases} [\mathbf{0}_M,\, \boldsymbol{X},\, \mathbf{0}_M]\,, & \text{if } N_\mathrm{f} \text{ is even} \\ [\mathbf{0}_M,\, 0,\, \boldsymbol{X},\, \mathbf{0}_M]\,, & \text{if } N_\mathrm{f} \text{ is odd} \end{cases} \tag{3.5}$$

The complex, time-domain samples are then given by

$$y_n = \frac{1}{\sqrt{N}} \left(\sum_{k=0}^{N/2-1} Y_{k+N/2}\, e^{j2\pi(nk/N)} + \sum_{k=N/2}^{N-1} Y_{k-N/2}\, e^{j2\pi(nk/N)} \right), \quad n = 0, 1, \ldots, N-1\,, \tag{3.6}$$

where N is even.

The nth time-domain sample corresponds to a delay $\tau_n = n/(N\Delta f)$. In both the real passband and complex baseband cases the time-domain resolution, $1/(N\Delta f)$, improves as N is increased. That is adding zeros to the end of the measured frequency response

---

[1] The offset is given by $\Delta f_0 = \lceil f_\mathrm{min}/\Delta f \rceil \Delta f - f_\mathrm{min}$. Then, using the frequency shifting property, the nth time-domain sample must be multiplied by $f_n = e^{-j2\pi \Delta f_0 \tau_n}$.

$\mathbf{0}_M$ improves the resolution. To satisfy the sampling theorem and avoid aliasing we need $N > 2\lceil f_{N_\mathrm{f}-1}/\Delta f\rceil = 2N_\mathrm{f}$.

To form time-domain responses for smaller transmission bandwidths using measurement data that was captured during one measurement session, we can bandpass filter the data. Given that the measurement is performed in the frequency domain, this can be achieved by simply setting values of the measured frequency response to zero. As discussed earlier, the resulting frequency ranges are limited by the frequency ranges of the measured data, but there is also a limitation on the minimum bandwidth. One can overcome this limitation if the frequency response is re-measured at a finer resolution, i.e. smaller Δf, but for speed and accuracy of data collection, we would like to minimize re-measurement.

Let $\boldsymbol{H}$ be a frequency mask containing N_f samples, such that

$$H_k = \begin{cases} 1\,, & f_k \in [f_\mathrm{L},\, f_\mathrm{H}] \\ 0\,, & \text{otherwise} \end{cases}, \quad k = 0, 1, \ldots, N_\mathrm{f} - 1\,, \tag{3.7}$$

where f_L and f_H are the lower and upper frequencies of the band of interest. Then, the frequency response, restricted to the new frequency band, is given by

$$\boldsymbol{X}' = \boldsymbol{H} \cdot \boldsymbol{X} \tag{3.8}$$

and the time-domain response can be computed using the procedure described above.

The Fourier transform pair for a low pass filter with bandwidth W Hz is given by

$$\mathrm{sinc}(Wt) = \frac{\sin(\pi W t)}{\pi t} \longleftrightarrow \mathrm{rect}\left(\frac{f}{W}\right)\,. \tag{3.9}$$

Thus the operation in (3.8) corresponds to convolution with a modulated, time-scaled sinc function in the time domain. The scaled sinc function has a peak at zero equal to W with zero crossings at $1/W$. Since, the sinc function contains more than 96% of its energy in within the first 3 zero crossings, its support can be reasonably approximated to $\tau_\mathrm{W} = 6/W$. Thus, the support of the resulting filtered response in the time domain is increased by τ_W and we need

$$\tau_\mathrm{max} + \tau_\mathrm{W} < \frac{1}{\Delta f}\,. \tag{3.10}$$

The actual value of $\tau_{\max}$ will strongly depend on the transmission power and the distribution of objects in the environment. Typical values reported in the literature for UWB transmission are on the order of 100s of ns. In the environments where we performed experiments values were less than 600 ns. Thus, a very conservative estimate is $\tau_{\max} = 1000$ ns. Using these values gives:

$$W > \frac{6\Delta f}{1 - \tau_{\max}\Delta f} = 24\,\mathrm{MHz}\,. \tag{3.11}$$

The primary focus of this thesis is on transmission bandwidths equal to or beyond those used in UWB transmission. The minimum bandwidth for UWB transmission is 500 MHz, therefore the above constraint is satisfied.

3.4.3 Channel Parameter Extraction Methodology

This section describes the procedure for extracting the path delays and gains from measured channel realizations. While this procedure gives an estimate of the underlying channel parameters, the results of this algorithm are treated as the true channel parameters used in subsequent sections.

Consider the transmission of a wideband signal $p(t)$ with support T_p. In this case, the received waveform $r(t)$ is commonly modeled as [5, 6]

$$r(t) = \sum_{l=1}^{N_{\mathrm{d}}} h_l p(t - \tau_l) + n(t)\,, \tag{3.12}$$

where $n(t)$ is AWGN. Eqn. (3.12) states that the received waveform can be written as a sum of scaled and shifted replicas of the transmit pulse $p(t)$. Letting $\boldsymbol{h} \in \mathbb{C}^{N_{\mathrm{d}}}$, consisting of elements h_l, denote the vector of channel gains and $\boldsymbol{\tau} \in \mathbb{C}^{N_{\mathrm{d}}}$, consisting of elements τ_l, denote the vector of delays, the received waveform can alternatively be expressed as

$$r(t) = \boldsymbol{w}^T(t, \boldsymbol{\tau})\boldsymbol{h} + n(t)\,. \tag{3.13}$$

For fixed t, $\boldsymbol{w}(t, \boldsymbol{\tau}) \in \mathbb{C}^{N_{\mathrm{d}}}$ is given as

$$\boldsymbol{w}(t, \boldsymbol{\tau}) = [p(t - \tau_1),\ p(t - \tau_2),\ \cdots,\ p(t - \tau_{N_{\mathrm{d}}})]^T \tag{3.14}$$

and $n(t)$ is complex AWGN with zero mean and spectral density $N_0/2$ per dimension.

The objective of the channel parameter extraction procedure is to estimate the vectors of delays and gains while minimizing the mean square error (MSE) between the estimated channel response and the received response. The MSE is defined as

$$\mathcal{E} \triangleq \int_T |r(t) - \hat{r}(t)|^2 dt \tag{3.15}$$

where the integration is performed over a range of interest T and

$$\hat{r}(t) = \boldsymbol{w}^T(t, \hat{\boldsymbol{\tau}})\hat{\boldsymbol{h}} \tag{3.16}$$

with $\hat{\boldsymbol{h}}$ and $\hat{\boldsymbol{\tau}}$ denoting the estimated amplitude vector and estimated delay vector, respectively. Since $n(t)$ is modeled as AWGN, the minimum mean square error (MMSE) estimation criterion is equivalent to the maximum likelihood (ML) estimation criterion. Given an observed received signal $r(t)$, it can be shown that the ML estimates of $\hat{\boldsymbol{h}}$ and $\hat{\boldsymbol{\tau}}$ are given by [5]

$$\hat{\boldsymbol{\tau}} = \arg\max_{\boldsymbol{\tau}} \left\{ \boldsymbol{\chi}^\dagger(\boldsymbol{\tau})\mathbf{R}^{-1}(\boldsymbol{\tau})\boldsymbol{\chi}(\boldsymbol{\tau}) \right\} \tag{3.17}$$

$$\hat{\boldsymbol{h}} = \mathbf{R}^{-1}(\hat{\boldsymbol{\tau}})\boldsymbol{\chi}(\hat{\boldsymbol{\tau}}). \tag{3.18}$$

where $\mathbf{R}(\boldsymbol{\tau}) \in \mathbb{C}^{N_\mathrm{d} \times N_\mathrm{d}}$ is the correlation matrix of the pulse for a vector of delays $\boldsymbol{\tau}$ which is defined as

$$\mathbf{R}(\boldsymbol{\tau}) = \int_T \boldsymbol{w}(t, \boldsymbol{\tau})\boldsymbol{w}(t, \boldsymbol{\tau})^\dagger dt\,. \tag{3.19}$$

Each entry of the matrix is the correlation between the transmitted pulses at delays τ_i and τ_j, i.e.,

$$[\mathbf{R}(\boldsymbol{\tau})]_{ij} \triangleq R(\tau_i - \tau_j) = \int_T p(t - \tau_i)p^*(t - \tau_j)dt\,. \tag{3.20}$$

The vector $\boldsymbol{\chi}(\boldsymbol{\tau}) \in \mathbb{C}^{N_\mathrm{d}}$ is defined as the correlation between the received signal and the pulse at different delays, which is given by

$$\chi(\boldsymbol{\tau}) = \int_T \boldsymbol{w}^*(t, \boldsymbol{\tau}) r(t) dt. \tag{3.21}$$

Note that (3.17) and (3.18) indicate that the estimation of $\boldsymbol{\tau}$ and $\boldsymbol{h}$ are separable problems, that is, $\hat{\boldsymbol{h}}$ in (3.18) provides the optimal solution given any $\hat{\boldsymbol{\tau}}$. Thus, one can focus on solving (3.17) without being concerned with $\hat{\boldsymbol{h}}$. However, it is difficult to directly solve the optimization in (3.17). Instead, we use the optimal approach for the resolvable channel. A resolvable channel is one in which the individual multipath components do not overlap, hence the matrix $\mathbf{R}(\boldsymbol{\tau})$ becomes diagonal. For the general case this method is suboptimal, but it has significantly lower computational complexity. When the channel is resolvable the optimization problem becomes

$$\hat{\boldsymbol{\tau}} = \arg \max_{\boldsymbol{\tau}: |\tau_i - \tau_j| > T_p} \left\{ \sum_{i=1}^{L} \frac{(\chi(\tau_i))^2}{R(0)} \right\}. \tag{3.22}$$

This indicates that $\hat{\boldsymbol{\tau}}$ can be determined by iteratively finding the peak of the absolute value of the correlation of the received signal and the pulse. These ideas form the basis for a method referred to as the search-subtract-readjust algorithm in [36] which jointly estimates the delays and gains of the multipath components in the channel response. The algorithm is given below in Alg. 1.

The algorithm operates by iteratively searching for the location of strongest path, subtracting the contribution due to this path, and then repeating the process using the new signal. In step 4 and 5 the matched filter output, $z(t)$, is computed and $\hat{\tau}_i$ is set equal to the delay corresponding to the largest peak of the absolute value of $z(\tau)$. The measured response at 1 m, in the appropriate frequency range, is used as the template pulse for the matched filter (for details see Sec. 2.2.2). This ensures that the algorithm removes the effect of the two antennas from the measured responses. Step 6 is responsible for updating the template vector, autocorrelation matrix, and cross-correlation vector. Steps 7 and 8 calculate the vector of channel gain estimates and construct the estimated signal. Finally, in step 9 the estimated channel response is subtracted from the received signal. This process is repeated on the resulting signal and continues until the termination criterion is satisfied.

Algorithm 1 Search-Subtract-Readjust Algorithm

```
Require: $r(t)$ a measured channel response, and $p(t)$ a template pulse
Initialize $\hat{\boldsymbol{\tau}}^{(0)} \leftarrow \emptyset$ and $\boldsymbol{w}^{(0)}\left(t, \hat{\boldsymbol{\tau}}^{(0)}\right) \leftarrow \emptyset$
Set $i \leftarrow 1$ and $y^{(i)}(t) \leftarrow r(t)$
repeat
    Calculate the matched filter output $z(\tau) \leftarrow \int_{-\infty}^{\infty} y^{(i)}(t) p^*(t-\tau) dt$
    Set $\hat{\tau}_i \leftarrow \arg\max_{\tau} \left\{ |z(\tau)| \right\}$, and update $\hat{\boldsymbol{\tau}}^{(i)} \leftarrow [\hat{\boldsymbol{\tau}}^{(i-1)} \; \hat{\tau}_i]$
    Update $\boldsymbol{w}^{(i)}\left(t, \hat{\boldsymbol{\tau}}^{(i)}\right)$, $\mathbf{R}^{(i)}\left(\hat{\boldsymbol{\tau}}^{(i)}\right)$ and $\boldsymbol{\chi}^{(i)}\left(\hat{\boldsymbol{\tau}}^{(i)}\right)$:

        $\boldsymbol{w}^{(i)}\left(t, \hat{\boldsymbol{\tau}}^{(i)}\right) \leftarrow \left[ \left( \boldsymbol{w}^{(i-1)}\left(t, \hat{\boldsymbol{\tau}}^{(i-1)}\right) \right)^T \; p(t-\hat{\tau}_i) \right]^T \qquad (3.23)$
        $\mathbf{R}^{(i)}\left(\hat{\boldsymbol{\tau}}^{(i)}\right) \leftarrow \int_T \boldsymbol{w}^{(i)}\left(t, \hat{\boldsymbol{\tau}}^{(i)}\right) \left( \boldsymbol{w}^{(i)}\left(t, \hat{\boldsymbol{\tau}}^{(i)}\right) \right)^{\dagger} dt \qquad (3.24)$
        $\boldsymbol{\chi}^{(i)}\left(\hat{\boldsymbol{\tau}}^{(i)}\right) \leftarrow \int_T \left( \boldsymbol{w}^{(i)}\left(t, \hat{\boldsymbol{\tau}}^{(i)}\right) \right)^{*} r(t) dt \qquad (3.25)$

    Calculate the channel gain estimate: $\hat{\boldsymbol{h}}^{(i)} \leftarrow \left( \mathbf{R}^{(i)}\left(\hat{\boldsymbol{\tau}}^{(i)}\right) \right)^{-1} \boldsymbol{\chi}^{(i)}\left(\hat{\boldsymbol{\tau}}^{(i)}\right)$
    Construct the estimated signal: $\hat{r}^{(i)}(t) \leftarrow \left( \boldsymbol{w}^{(i)}\left(t, \hat{\boldsymbol{\tau}}^{(i)}\right) \right)^T \hat{\boldsymbol{h}}^{(i)}$
    Set $i \leftarrow i + 1$ and $y^{(i)}(t) \leftarrow r(t) - \hat{r}^{(i-1)}(t)$
until termination criterion is satisfied                    ▷ see Sec. 3.4.3
Set $N_{\mathrm{d}} \leftarrow i - 1$
```

Termination Criterion

As paths are added, the estimated signal captures an increasingly larger portion of the energy in the received signal. When the fraction of the uncaptured received signal energy becomes negligibly small, all the major paths of the received signal have been acquired, and then the algorithm can be stopped. Thus, the termination criterion is related to the fraction of received signal energy captured by the estimated signal. In particular, the *energy capture* (EC) is defined as

$$E_{\mathrm{C}}(\hat{\boldsymbol{\tau}}, \hat{\boldsymbol{h}}) = 1 - \frac{\int |r(t) - \hat{r}(t)|^2 dt}{\int |r(t)|^2 dt}. \tag{3.26}$$

The EC gives the fraction of energy captured by the current estimate of the channel response. In Step 10 of Alg. 1, the termination criterion is based on the difference of the EC, i.e., $\Delta E_{\mathrm{C}}^{(i)} = E_{\mathrm{C}}(\hat{\boldsymbol{\tau}}^{(i)}, \hat{\boldsymbol{h}}^{(i)}) - E_{\mathrm{C}}(\hat{\boldsymbol{\tau}}^{(i-1)}, \hat{\boldsymbol{h}}^{(i-1)})$. The criterion used is to stop at iteration i if

$$\frac{1}{K} \sum_{k=0}^{K-1} \mathbb{1}_{\left\{\Delta E_{\mathrm{C}}^{(i-k)} \leq \lambda\right\}} \geq \Lambda \tag{3.27}$$

where $K = 10$, $\lambda = 0.1\%$, and $\Lambda = 90\%$. For these specific values, the termination criterion can be interpreted as: the algorithm will stop adding additional paths if the change in EC ($\Delta E_{\mathrm{C}}^{(i)}$) was no greater than 0.1% for 9 out of 10 previous consecutive iterations. The minimum value of i which satisfies the above criterion is denoted as N_{d} for that particular measured waveform.

Algorithm Implementation

This section discusses implementation details of Alg. 1 and steps that were taken to maximize the efficiency of the computations involved. The next section gives details about signal discretization, followed by a discussion of frequency domain matched filtering, and finally details of how $\mathbf{R}$ and its inverse are computed efficiently.

Although the search-subtract-readjust algorithm given in Alg. 1 is for continuous signals, the implementation of the algorithm requires the discretization of all the signals. In particular, $r(t)$, $y(t)$, and $p(t)$ are represented as vectors $\boldsymbol{r} \in \mathbb{C}^{N_{\mathrm{s}}}$, $\boldsymbol{y} \in \mathbb{C}^{N_{\mathrm{s}}}$, and $\boldsymbol{p} \in \mathbb{C}^{N_{\mathrm{s}}}$, where r_k, y_k, and p_k are samples of the respective waveforms. The vector $\boldsymbol{w}^T(t, \boldsymbol{\tau})$ which is a function of the continuous parameter t can now be written as $\mathbf{W}(\boldsymbol{\tau}) \in \mathbb{C}^{N_s \times N_d}$ given by

$$\mathbf{W}(\boldsymbol{\tau}) = [\boldsymbol{w}(\tau_1),\ \boldsymbol{w}(\tau_2), \cdots,\ \boldsymbol{w}(\tau_{N_d})] \tag{3.28}$$

where $\boldsymbol{w}(\tau_i)$ is a vector consisting of samples of $p(t - \tau_i)$. Using the matrix $\mathbf{W}(\boldsymbol{\tau})$, the calculation of $\mathbf{R}(\boldsymbol{\tau})$, $\boldsymbol{\chi}(\boldsymbol{\tau})$ and $\boldsymbol{r}$ becomes

$$\mathbf{R}(\boldsymbol{\tau}) = \mathbf{W}^{\dagger}(\boldsymbol{\tau})\mathbf{W}(\boldsymbol{\tau}) \tag{3.29}$$

$$\boldsymbol{\chi}(\boldsymbol{\tau}) = \mathbf{W}^{\dagger}(\boldsymbol{\tau})\boldsymbol{r} \tag{3.30}$$

$$\boldsymbol{r} = \mathbf{W}(\boldsymbol{\tau})\boldsymbol{h}. \tag{3.31}$$

To determine the matched filter output in step 4, we need to calculate the convolution of the received signal $r(t)$ with the pulse $p^*(-t)$. In discrete time, this becomes the convolution of the vector $\boldsymbol{r}$ and $\boldsymbol{p}$. Since the vector $\boldsymbol{r}$ is very large in dimension, it is not efficient to directly compute the convolution in the time domain. To expedite the computation, the signals are first transformed to the frequency domain, the product of the two frequency-domain signal vectors is computed, and then the result is transform back to the time domain. In particular,

$$y_i(t) = r(t) * p(-t) \tag{3.32}$$

$$= \mathcal{F}^{-1}\left\{\mathcal{F}\{r(t)\} \times \mathcal{F}\{p(-t)\}\right\}, \tag{3.33}$$

where, in the discrete case, $\mathcal{F}$ and $\mathcal{F}^{-1}$ represent the Fourier transform (FT) and inverse Fourier transform (IFT), respectively.

The computation of $\hat{\boldsymbol{h}}^{(i)}$ in step 7 of Alg. 1 can be of high complexity if the quantity $\left((\mathbf{W}^{(i)})^{\dagger}\mathbf{W}^{(i)}\right)^{-1}$ is directly computed. However, it should be noted that the matrix $\mathbf{W}$ is updated by merely adding one column vector in each iteration, i.e.,

$$\mathbf{W}^{(i)} = [\mathbf{W}^{(i-1)}\ \boldsymbol{w}^{(i)}]. \tag{3.34}$$

The computation of $\mathbf{R}^{(i)} = \left(\mathbf{W}^{(i)}\right)^{\dagger}\mathbf{W}^{(i)}$ can be expedited by first computing the autocorrelation of $\boldsymbol{p}$ for all possible discretized values of τ_i. Then, instead of directly computing $\mathbf{R}^{(i)}$ in each iteration, values of the autocorrelation can determined via table lookup.

Also note that $\left(\mathbf{W}^{(i)}\right)^{\dagger}\mathbf{W}^{(i)}$ can be written as

$$\mathbf{R}^{(i)} = \left(\mathbf{W}^{(i)}\right)^{\dagger}\mathbf{W}^{(i)} = \begin{bmatrix} \mathbf{R}^{(i-1)} & \boldsymbol{b}^{(i)} \\ \left(\boldsymbol{b}^{(i)}\right)^{\dagger} & c^{(i)} \end{bmatrix}, \tag{3.35}$$

where $\mathbf{R}^{(i-1)} \in \mathbb{C}^{(i-1)\times(i-1)}$, $\boldsymbol{b}^{(i)} \in \mathbb{C}^{i-1}$ and $c^{(i)} \in \mathbb{R}$. Now, the inverse of the matrix $\mathbf{R}^{(i)}$ can be written as:

$$\left(\mathbf{R}^{(i)}\right)^{-1} = \begin{bmatrix} \mathbf{R}^{(i-1)} & \boldsymbol{b}^{(i)} \\ \left(\boldsymbol{b}^{(i)}\right)^{\dagger} & c^{(i)} \end{bmatrix}^{-1} = \begin{bmatrix} \mathbf{D}^{(i)} & \boldsymbol{d}^{(i)} \\ \left(\boldsymbol{d}^{(i)}\right)^{\dagger} & d^{(i)} \end{bmatrix}. \tag{3.36}$$

Then, the quantities $d^{(i)}$, $\mathbf{D}^{(i)}$, and $\boldsymbol{d}^{(i)}$ can be computed as follows:

$$d^{(i)} = 1/\left(c^{(i)} - \left(\boldsymbol{b}^{(i)}\right)^{\dagger}\left(\mathbf{R}^{(i-1)}\right)^{-1}\boldsymbol{b}^{(i)}\right) \tag{3.37}$$

$$\boldsymbol{d}^{(i)} = -d^{(i)}\left(\mathbf{R}^{(i-1)}\right)^{-1}\boldsymbol{b}^{(i)} \tag{3.38}$$

$$\mathbf{D}^{(i)} = \left(\mathbf{R}^{(i-1)}\right)^{-1} - \boldsymbol{d}^{(i)}\left(\boldsymbol{b}^{(i)}\right)^{\dagger}\left(\mathbf{R}^{(i-1)}\right)^{-1} \tag{3.39}$$

where $\left(\mathbf{R}^{(i-1)}\right)^{-1} = \left(\left(\mathbf{W}^{(i-1)}\right)^{\dagger}\mathbf{W}^{(i-1)}\right)^{-1}$ is the matrix inverse in the previous iteration. In general, the computational complexity of directly computing the matrix inverse $\left(\mathbf{R}^{(i)}\right)^{-1}$ is $\mathcal{O}(i^3)$, while the complexity of computing (3.37)–(3.39) is of order $\mathcal{O}(i^2)$.

3.5 Sample Channel Realizations

One sample realization from each of the representative locations is shown in Figs. 3-4 and 3-5. Fig. 3-4 shows the response at the full measurement bandwidth of 16 GHz. Here it can be seen that the line-of-sight (LOS) measurements (locations A and G) are characterized by very sharp peaks, while the non-line-of-sight (NLOS) measurements (locations M and O) show a much higher level of dispersion. In LOS scenarios, the sharp peaks present in the channel response contain a large portion of the total received energy, whereas in NLOS scenarios the dispersion accounts for a larger fraction of the total received energy. Fig. 3-5 shows the same realizations at a bandwidth of 1 GHz and a center frequency of 10 GHz. Similar to the 16 GHz case, this figure shows that there are very few dominant paths in NLOS environments. As expected, the dominant paths in the time-domain responses have

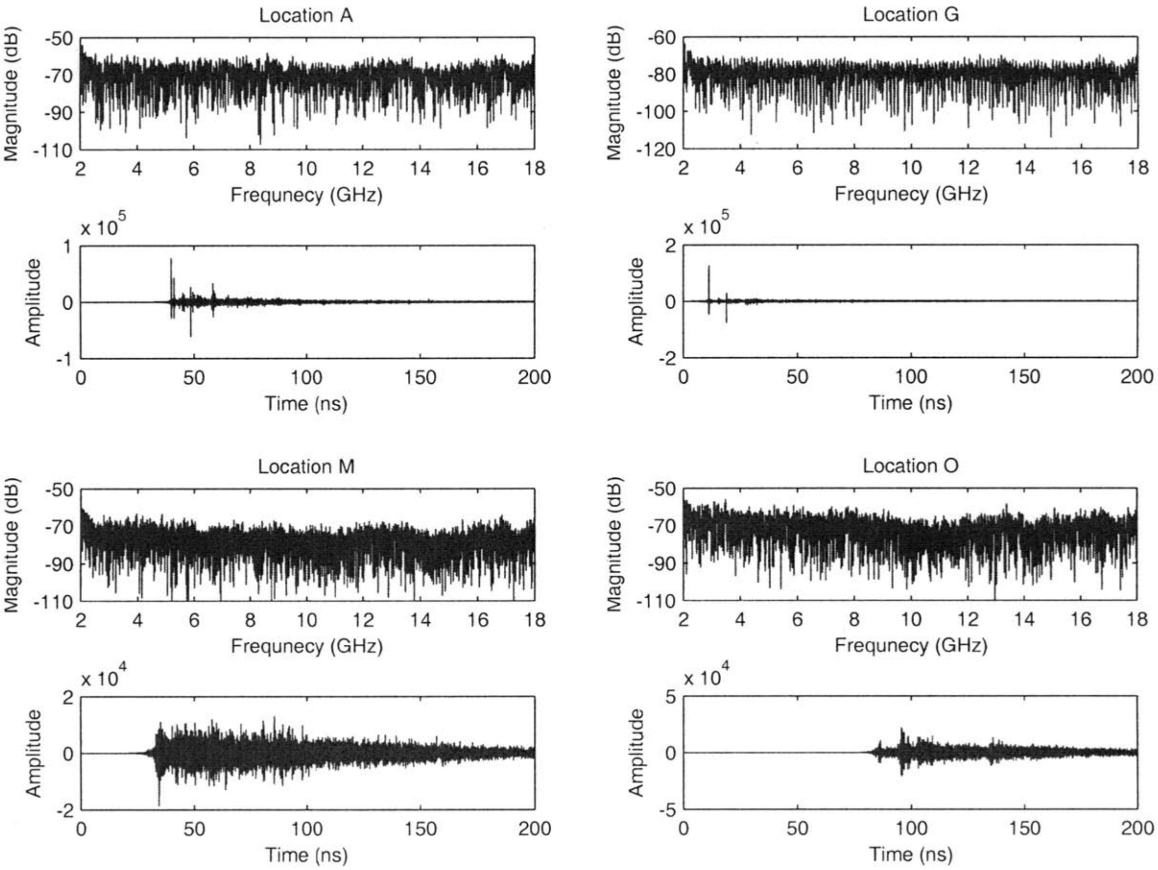

Figure 3-4: The magnitude of the frequency responses and the passband time-domain responses are shown for four sample realizations, normalized to have unit energy, at 16 GHz bandwidth with $f_c = 10\,\text{GHz}$.

widened, causing some averaging of the multipath components. In particular, for location A, it is no longer possible to distinguish the closely spaced initial paths present in the response at 16 GHz.

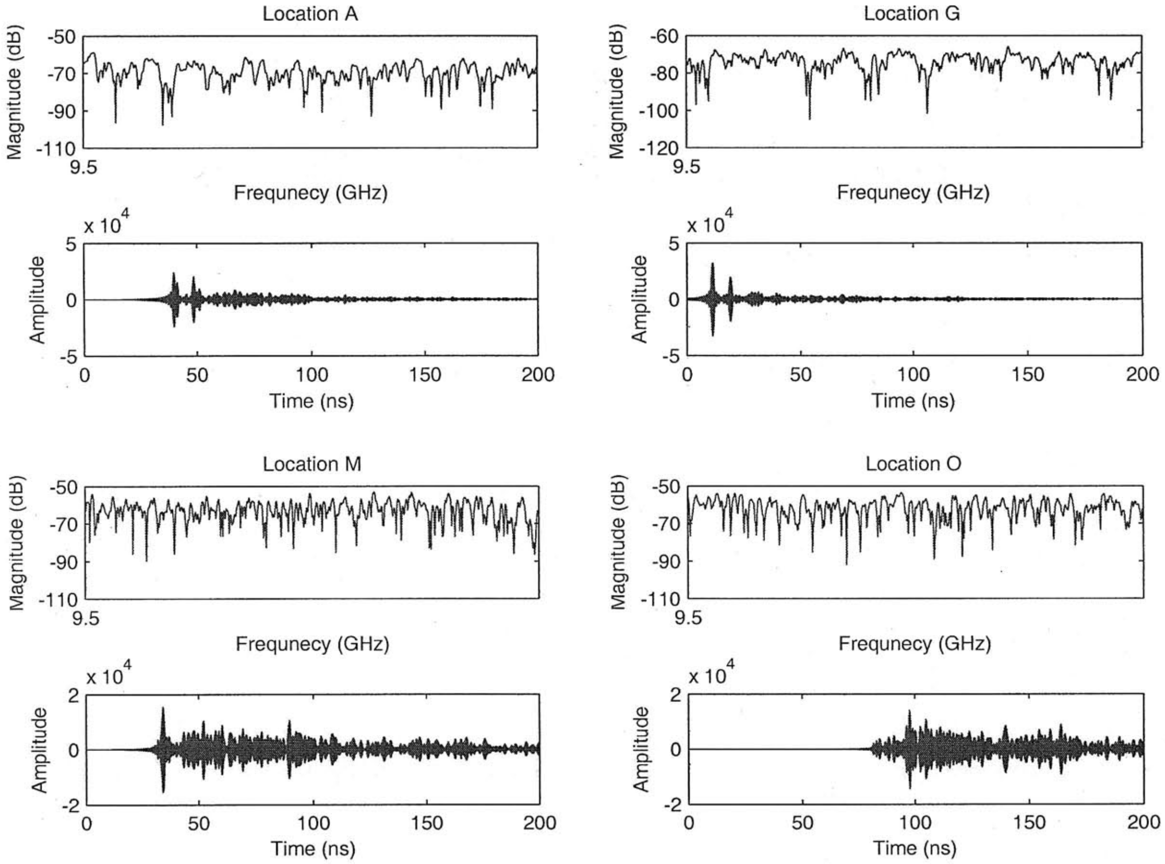

Figure 3-5: The magnitude of the frequency responses and the passband time-domain responses are shown for four sample realizations, normalized to have unit energy, at 1 GHz bandwidth with $f_c = 10\,\text{GHz}$.

Chapter 4

Wideband Subset Diversity Systems

Multipath diversity using spread spectrum (SS) signaling [18–23,25] has played an increasingly important role in current and future wireless systems. Wide transmission bandwidths available in SS systems allow receivers to resolve closely spaced multipath components. The detection of signals in multipath environments is typically done using a Rake receiver, where the components of a received signal (arriving at different times) are combined to provide diversity. Discussions on classical Rake architectures can be found in [18–21]. One version of the Rake receiver consists of multiple correlators (fingers), each correlator detecting the signal from one of the multipath components created by the channel. The outputs of the Rake fingers are then combined to achieve the benefits of multipath diversity.

Similarly, the matched filter version of a Rake receiver involves a matched front-end processor (MFEP) (matched *only* to the transmitted signature waveform) followed by a tapped delay line and a combiner. Multipath components with separation greater than the chip time T_c (approximately equal to the inverse of the spreading bandwidth) are resolved by the MFEP, which is synchronized with the initial path of the received signal. The MFEP output is passed through a tapped delay line filter with $N_\mathrm{d} = T_\mathrm{d}/T_\mathrm{c}$ taps, where T_d is the maximum excess delay from the first arriving path. The output of the taps provide N_d diversity paths, which must all be combined to achieve the best possible performance.

The all Rake (ARake) receiver describes a receiver with unlimited resources, so that it is capable of combining *all* of the available multipath components. For a dense multipath channel with a fixed T_d, the number of resolvable multipath components increases with the spreading bandwidth. However, the power consumption and cost of RF electronics typically limits the number of multipath components utilized in many receivers [4, 5].

These complexity and performance issues have motivated studies of multipath combining receivers that process only a *subset* of the available resolved multipath components, but achieve better performance than a single path (SP) receiver. We refer to such receivers as RSSD receivers. Note that the class of RSSD receivers includes the selective Rake (SRake) receiver, where the best L_d out of N_d multipath components are combined. Such subset based schemes are a way to reduce resource use in receiver designs while maintaining the benefits of increased diversity order [26–29].

Many previous studies of RSSD assumed that perfect channel knowledge is available at the receiver. However, practical RSSD receivers must estimate the channel gain affecting each multipath component, and thereby incur a performance loss [30–35]. In the case of non-ideal RSSD, the estimation plays a dual role; it affects *both* the selection process as well as the combining mechanism. Indeed, in an RSSD receiver the subset of multipath components chosen is based on the receiver's knowledge of the channel, i.e., the *estimated* channel gains. Therefore, there is a possibility that the receiver makes an erroneous selection.

This chapter develops a framework for evaluating the SEP of non-ideal RSSD for two cases of fading channels. Specifically, the cases considered are: 1) a wide-sense stationary uncorrelated scattering (WSSUS) channel with a constant power delay profile and complex Gaussian fading gains, and 2) channel realizations measured in a realistic propagation environment. The first case provide a benchmark and allows for the comparison with known results in the literature. The second case allows for a more accurate understanding of the performance in realistic fading channels at different bandwidths and center frequencies. In both cases, the framework is valid for transmission of symbols from an arbitrary two-dimensional signaling constellation.

This chapter is organized as follows. In the next section, the models for the system and estimator are presented. In Sec. 4.2 we evaluate the SEP of SSD systems with and without channel estimation error for Rayleigh fading. In Sec. 4.3 SEP expressions for SSD systems with and without estimation error are developed for a finite set of channel realizations. Sec. 4.4 gives numerical results based on channel realizations measured in a realistic propagation environment and then processed with the channel parameter extraction algorithm described in Sec. 3.4.3. Finally, in Sec. 4.5 we present concluding remarks.

4.1 System and Channel Model

This section describes the signaling model as well as the channel model. In particular, we will consider the transmission of signals with the form

$$s_m(t) = s_m s(t),$$

where $s_m \in \{s_1, s_2, \dots, s_M\}$ is a complex number representing the message symbol to be transmitted and $s(t)$ is the basic signature waveform. The signal $s(t)$ has support $[0, T_\mathrm{s})$ and unit energy, i.e. $\int_0^{T_\mathrm{s}} s^2(t)dt = 1$. The energy of the mth symbol and average energy are defined as $E_m \triangleq |s_m|^2$ and $E_\mathrm{s} \triangleq \sum_{m=1}^{M} p_m E_m$, respectively, where p_m is a priori probability that s_m is transmitted. For general SS modulation, the signal $s(t)$ is composed of several pulses or chips of duration T_c. We note that this model is applicable to the transmission of symbols from arbitrary two-dimensional signaling constellations, including QAM and PSK.

The received signal, in complex equivalent lowpass (ELP) form, can be written as

$$r(t) = \underbrace{\int_{-\infty}^{\infty} h(t,\tau)\, s_m(t-\tau)\, d\tau}_{\triangleq\, y(t)} + n(t),$$

where $n(t)$ is a complex baseband, circularly symmetric, AWGN process with power spectral density $N_0/2$. The channel, $h(t,\tau)$, is time varying, but the fading is slow enough so that one can estimate the channel. We consider a dense multipath channel, that arises in environments such as urban canyons, with uniform power delay profile.

The received signal is passed through a MFEP filter with ELP impulse response

$$f_\mathrm{M}(t) \triangleq \begin{cases} s(T_\mathrm{s} - t), & \text{for } 0 < t < T_\mathrm{s} \\ 0, & \text{otherwise.} \end{cases}$$

The MFEP output can be written as

$$\begin{aligned} r_{\mathrm{M}}(t) &= \int_0^{\infty} r(t-\alpha) f_{\mathrm{M}}(\alpha)\, d\alpha \\ &= y_{\mathrm{M}}(t) + n_{\mathrm{M}}(t), \end{aligned}$$

where the contribution of the signal and noise, $y_{\mathrm{M}}(t)$ and $n_{\mathrm{M}}(t)$, are given by

$$\begin{aligned} y_{\mathrm{M}}(t) &= \int_0^{\infty}\int_0^{\infty} h(t-\alpha,\tau)\, s_m(t-\alpha-\tau)\, f_{\mathrm{M}}(\alpha)\, d\tau d\alpha \\ n_{\mathrm{M}}(t) &= \int_0^{\infty} n(t-\alpha) f_{\mathrm{M}}(\alpha)\, d\alpha. \end{aligned}$$

The MFEP output is sampled at appropriate time instants, t_k's, to produce complex outputs, r_k, where

$$r_k = h_k s_m + n_k, \tag{4.1}$$

where h_k is an effective gain introduced by the channel and the pulse shape, and n_k is a circularly symmetric, complex Gaussian random variable (RV) with variance $N_0/2$ per dimension. The variance of h_k is denoted as $\mathbb{V}\{h_k\} = 2\sigma_h^2$. In this case no specific properties of the underlying channel $h(t,\tau)$ have been assumed. This model makes the most sense when considering channel realizations that were measured in a realistic environment.

One particular case of interest, which has been frequently studied in the literature, is when the time-varying channel $h(t,\tau)$ is modeled as a complex circularly symmetric Gaussian process with zero mean. Since $y_{\mathrm{M}}(t)$ is a linear transformation of $h(t,\tau)$, it is also a complex Gaussian process with zero mean. For a slowly varying WSSUS channel with a constant power delay profile, the correlation of the signal contribution satisfies [27–29]

$$\mathbb{E}\left\{y_{\mathrm{M}}^{*}(t_i)\, y_{\mathrm{M}}(t_j)\right\} = \begin{cases} \beta\frac{T_{\mathrm{c}}}{T_{\mathrm{d}}}E_m, & |t_i - t_j| = 0 \\ \tilde{\beta}\frac{T_{\mathrm{c}}}{T_{\mathrm{d}}}E_m, & |t_i - t_j| = T_{\mathrm{c}} \\ 0, & |t_i - t_j| \geq 2T_{\mathrm{c}}, \end{cases}$$

where β and $\tilde{\beta}$ are multiplicative factors that depend on the pulse shape. It was shown in [27–29] that $\tilde{\beta}$ is small. Hence, as in [22, 23], we treat the sampled outputs, $\{y_{\mathrm{M}}(t_k)\}$, as uncorrelated RVs. For this channel model, note that h_k is a zero-mean, complex, circularly symmetric Gaussian RV with $\mathbb{E}\{|h_k|^2\} = 2\sigma_h^2 = \beta T_c/T_d$. The fact that the $y_M(t_k)$'s are uncorrelated implies that the h_k's are indeed independent.

In this chapter two models for h_k will be considered. In the first case, the h_k will be modeled as independent, zero-mean, complex, circularly-symmetric Gaussian RVs. This model is equivalent to the IID Rayleigh fading case commonly used in the literature. In the second case, the properties of h_k will not be known, but a set of realizations will be available from measurements collected in realistic propagation environments.

4.1.1 Ideal Maximal-ratio Combining

If the channel gains, $\boldsymbol{h} = [h_1 \ h_2 \ \cdots \ h_{N_d}]$, are known to the receiver, using the above model we can write the likelihood function that message symbol s_i was transmitted as:

$$f_{\boldsymbol{r}}(\boldsymbol{r}|\boldsymbol{h}, s_i) = \left(\frac{1}{\pi N_0}\right)^{N_d} \exp\left\{-\frac{\sum_{k=1}^{N_d} |r_k - h_k s_i|^2}{N_0}\right\}.$$

The ML receiver operates by choosing the message symbol s_i that maximizes the likelihood above, or minimizes the quantity $\sum_{k=1}^{N_d} |r_k - h_k s_i|^2$. This is equivalent to the receiver that seeks to determine the message symbol s_i which minimizes the quantity

$$\left|D - \|\boldsymbol{h}\|^2 s_i\right|^2 \tag{4.2}$$

where we have defined the complex-valued decision variable

$$D \triangleq \sum_{k=1}^{N_d} h_k^* r_k . \tag{4.3}$$

Note that the rule described in (4.2) and (4.3) is equivalent to choosing the s_i for which $\|\boldsymbol{h}\|^2 s_i$ is closest to D. For the case of maximal-ratio combining (MRC) the rule in (4.2) is optimal in the ML sense and it further reduces to a minimum distance decision rule. Subsequent sections will consider the case where a subset of the diversity branches are selected and combined under different levels of receiver knowledge.

4.1.2 Ideal Selection and Combining

For ideal selection and combining, the receiver again has access to the true channel gains. Thus, the decision variable is given by

$$D \triangleq \sum_{k \in \mathcal{O}_{\mathrm{I}}} h_k^* r_k \,, \tag{4.4}$$

where $\mathcal{O}_{\mathrm{I}}$ is a set of indices indicating which subset of branches to combine. Note that $\mathcal{O}_{\mathrm{I}} \subseteq \{1, 2, \ldots, N_{\mathrm{d}}\}$.

The selection process for this method operates on the squared magnitude of the true channel gain $g_k \triangleq |h_k|^2$. The vector of *ordered* magnitudes is then defined as

$$\boldsymbol{g}_{[N_{\mathrm{d}}]} \triangleq \left[g_{[1]} \;\; g_{[2]} \;\; \cdots \;\; g_{[N_{\mathrm{d}}]}\right]^T ,$$

where $\{g_{[i]}\}$ is the ordered set of $\{g_i\}$ such that $g_{[1]} > g_{[2]} > \ldots > g_{[N_{\mathrm{d}}]}$. Note that the possibility of at least two equal $g_{[l]}$'s is excluded, since $g_{[l]} \neq g_{[m]}$ *almost surely* for continuous RVs $g_{[l]}$'s [44, 45].

When the selection is based on $\boldsymbol{g}_{[N_{\mathrm{d}}]}$, the corresponding index set denoted by $\mathcal{O}_{\mathrm{I}}$ is determined by a binary-valued selection vector, $\boldsymbol{a}$, with lth element $a_l \in \{0, 1\}$ that indicates which of the diversity branches are included in the combining process. For example, $a_l = 1$ indicates that $g_{[l]}$ is included in the combining process. In particular,

$$\mathcal{O}_{\mathrm{I}} \triangleq \left\{k \,:\, a_{\chi(k)} = 1\right\} ,$$

where $\chi(\cdot)$ is the bijective mapping from the indices of the unordered physical branches to the indices of the ordered branches. In this case the ordering is with respect to the g_k's, derived from ideal channel state information. It is convenient to define the total contribution of the channel gains as

$$\gamma_{\mathrm{I}} \triangleq \sum_{k \in \mathcal{O}_{\mathrm{I}}} |h_k|^2 = \sum_{l=1}^{N_{\mathrm{d}}} a_l g_{[l]} = \langle \boldsymbol{a},\, \boldsymbol{g}_{[N_{\mathrm{d}}]} \rangle \,.$$

Note that γ_{I} is the norm-square of the vector whose elements are from the selected subset of fading gains. Note that ideal selection and combining is equivalent to ideal MRC when

$\boldsymbol{a} = \mathbf{1}_{N_\mathrm{d}}$. The performance analysis for ideal selection and combining is given in Section 4.2.

4.1.3 Non-ideal Selection and Combining

In practical systems the vector of channel gains $\boldsymbol{h}$ must first be estimated by the receiver. Thus, in this case the combiner output is

$$D = \sum_{k \in \mathcal{O}_\mathrm{N}} \hat{h}_k^* r_k \,, \tag{4.5}$$

where $\hat{h}_k$ is the estimate of the multiplicative gain, h_k, of the kth branch. Note that, as indicated by (4.5), we are considering a receiver that utilizes the same structure as (4.4), but must first estimate the channel gains. Depending on the nature of the underlying channel gains this structure may not be optimal, but it is practical and can be implemented in real systems. It can also be used to model the case where the underlying assumptions about the channel gains and the estimation process are not ideal. Clearly, the performance of this combining scheme greatly depends on the quality of the estimate $\hat{h}_k$. Note also that the set of selected branches is indicated by $\mathcal{O}_\mathrm{N}$, where, in this case, the branches are chosen based on their estimated channel gains.

One way to estimate the channel gains is by using pilot symbols

$$p_{k,j} = \sqrt{E_\mathrm{p}} h_k + n_{k,j} \,,$$

where $p_{k,j}$ represents the pilot received on the kth branch during the jth previous signaling interval and E_p is the energy of the pilot symbol. An estimate can be formed by averaging N_p pilot symbols received within the coherence time of the channel[1]

$$\hat{h}_k = \frac{\sum_{j=1}^{N_\mathrm{p}} p_{k,j}}{\sqrt{E_\mathrm{p}} N_\mathrm{p}} = h_k + e_k \,.$$

In this case e_k is the complex Gaussian estimation error with zero mean and variance $\sigma_e^2 = N_0/(2E_\mathrm{p}N_\mathrm{p})$ per dimension. The pilot energy is related to the signal energy through the quantity $\varepsilon = E_\mathrm{p}/E_\mathrm{s}$. It is important to stress that N_p represents the number of *received*

---

[1] Note that the channel estimation process is carried out to track changes in the channel, and thus pilot symbols need only be transmitted with a rate suitable to track the fading.

pilot symbols used in forming an estimate of each branch. Depending on the choice of transmitter and receiver architectures of a SSD system, the actual number of transmitted pilots may need to be larger to guarantee an estimate of each branch based on N_{p} pilots.[2]

The non-ideal selection mechanism operates on the squared magnitude of the channel gain estimates, defined as $\widetilde{g}_k \triangleq \left|\hat{h}_k\right|^2$. The vector of *ordered* magnitudes is defined as

$$\widetilde{\boldsymbol{g}}_{[N_{\mathrm{d}}]} \triangleq \left[\widetilde{g}_{[1]} \;\; \widetilde{g}_{[2]} \;\; \cdots \;\; \widetilde{g}_{[N_{\mathrm{d}}]}\right]^T ,$$

such that $\widetilde{g}_{[1]} > \widetilde{g}_{[2]} > \ldots > \widetilde{g}_{[N_{\mathrm{d}}]}$. Again, note that the possibility of at least two equal $\widetilde{g}_{[l]}$'s is excluded, since $\widetilde{g}_{[l]} \neq \widetilde{g}_{[m]}$ *almost surely* for continuous RVs $\widetilde{g}_{[l]}$'s.

When the selection is based on $\widetilde{\boldsymbol{g}}_{[N_{\mathrm{d}}]}$, the corresponding index set denoted by $\mathcal{O}_{\mathrm{N}}$ is determined by a binary-valued selection vector, $\boldsymbol{a}$, with lth element $a_l \in \{0, 1\}$ that indicates which of the diversity branches are included in the combining process. For example, $a_l = 1$ indicates that $\widetilde{g}_{[l]}$ is included in the combining process. In particular,

$$\mathcal{O}_{\mathrm{N}} \triangleq \left\{k \, : \, a_{\widetilde{\chi}(k)} = 1\right\} ,$$

where $\widetilde{\chi}(\cdot)$ is the bijective mapping from the indices of the unordered physical branches to the indices of the ordered branches. In this case the ordering is done with respect to the $\widetilde{g}_k$'s, derived from the estimated channel state information. The total contribution of the channel estimates is defined as

$$\gamma_{\mathrm{N}} \triangleq \sum_{k \in \mathcal{O}_{\mathrm{N}}} \left|\hat{h}_k\right|^2 = \sum_{l=1}^{N_{\mathrm{d}}} a_l \widetilde{g}_{[l]} = \langle \boldsymbol{a}, \, \widetilde{\boldsymbol{g}}_{[N_{\mathrm{d}}]} \rangle \, .$$

Note that γ_{N} is the norm-square of the vector whose elements consist of the selected subset of *estimated* fading gains. Later, for both ideal and non-ideal selection and combining, it will be shown that particular diversity combining schemes, such as hybrid selection/maximal-ratio combining (H-S/MRC) with non-ideal channel estimation, reduce to special cases of the selection vector $\boldsymbol{a}$. Fig. 4-1 provides a conceptual view of a SSD system utilizing non-ideal channel estimates.

The main goal of the analysis is to obtain insights into the effect of non-ideal selection

---

[2] For example, in the case of a diversity receiver with $L_{\mathrm{d}} < N_{\mathrm{d}}$ receiver chains it may not be possible to receive the transmitted pilots on all branches simultaneously. It can be shown that $\lceil N_{\mathrm{d}}/L_{\mathrm{d}} \rceil \, N_{\mathrm{p}}$ pilots need to be transmitted to ensure at least N_{p} pilots are received for estimation on each of the N_{d} branches.

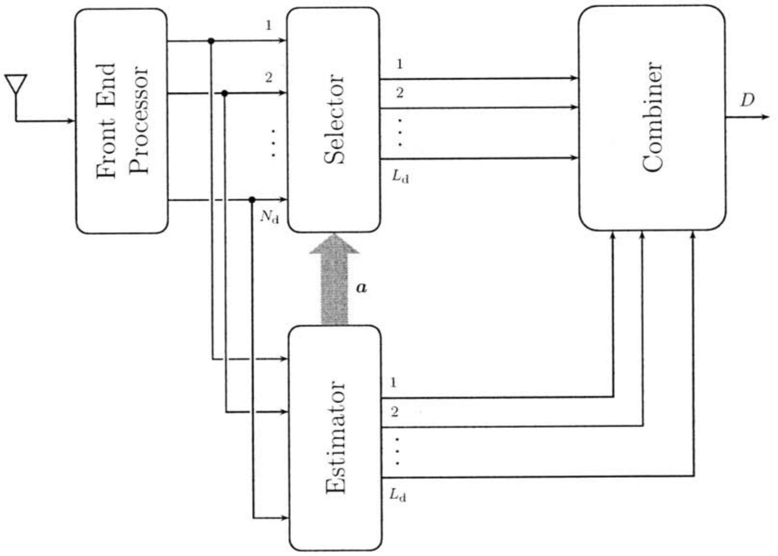

Figure 4-1: The basic structure of a RSSD receiver.

and non-ideal combining, where the diversity branches are chosen based on the estimate of the channel state at the receiver.

4.2 Analysis for Subset Diversity in Rayleigh Fading

In this section the specific case of IID Rayleigh fading will be considered. In particular, each channel gain can be written as a circularly symmetric complex Gaussian RV, $h_k = h_{k,\mathrm{r}} + \jmath h_{k,\mathrm{i}}$, with $\mathbb{E}\{h_k\} = 0$ and $\mathbb{E}\left\{|h_k|^2\right\} = \mathbb{E}\left\{|h_{k,\mathrm{r}}|^2\right\} + \mathbb{E}\left\{|h_{k,\mathrm{i}}|^2\right\} = 2\sigma_h^2$. First, results for the ideal case are reviewed. Second, the case of non-ideal selection and combining is considered. Then the moment generating functions (MGFs) of γ_I and γ_N are given. Finally, the exact SEP expressions are given for some specific cases of interest.

4.2.1 Ideal Selection and Combining

This section gives a brief overview of the conditional SEP, as well as the exact SEP for the case of ideal selection and combining in IID Rayleigh fading. For more details, the interested reader is directed to [46, 47]. In this case, the decision variable D is given by

(4.4), expanding gives:

$$D = \sum_{k \in \mathcal{O}_\mathrm{I}} h_k^* r_k = \sum_{k \in \mathcal{O}_\mathrm{I}} \left(|h_k|^2 s_i + h_k^* n_k \right) \tag{4.6}$$

The set of channel gains utilized in the combining process is denoted as:

$$\mathcal{S}_\mathrm{I} \triangleq \{ h_k : k \in \mathcal{O}_\mathrm{I} \} \ .$$

Theorem 1. *Conditioning on the set and a particular s_i, D is a circularly symmetric complex Gaussian RV with conditional mean and variance given by*

$$\mathbb{E}\{D | \mathcal{S}_I, s_i\} = s_i \gamma_I \tag{4.7}$$

$$\mathbb{V}\{D | \mathcal{S}_I, s_i\} = \mathbb{V}\{\Re\{D\} \,|\, \mathcal{S}_N, s_i\} + \mathbb{V}\{\Im\{D\} \,|\, \mathcal{S}_N, s_i\} = N_0 \gamma_I , \tag{4.8}$$

where $\gamma_I = \sum_{k \in \mathcal{O}_I} |h_k|^2$.

Proof. The proof follows directly from the expansion of the decision variable D in (4.6). ☐

Using the results of Thm. 1, the conditional SEP can be written as [48, 49]

$$\Pr\{\mathrm{e} | \mathcal{S}_\mathrm{I}, s_i\} = \frac{1}{2\pi} \sum_{j \in \mathcal{B}_i} \int_0^{\phi_{i,j}} \exp\left[-\frac{E_\mathrm{s} w_{i,j} \gamma_\mathrm{I}}{4 N_0 \sin^2(\theta + \psi_{i,j})} \right] d\theta \, . \tag{4.9}$$

Note that the conditional SEP expression in (4.9) makes no assumptions about the distribution of the channel gains, therefore it is valid for any distribution. This fact will be used in Sec. 4.3.1 to derive the SEP in realistic fading channels. Averaging the conditional SEP over the distribution of γ_I gives the exact SEP:

$$\begin{aligned} \Pr\{\mathrm{e} | s_i\} &= \frac{1}{2\pi} \sum_{j \in \mathcal{B}_i} \int_0^{\infty} \int_0^{\phi_{i,j}} \exp\left[-x \frac{w_{i,j} E_\mathrm{s}}{4 N_0 \sin^2(\theta + \psi_{i,j})} \right] f_{\gamma_\mathrm{I}}(x) \, d\theta \, dx \\ &= \frac{1}{2\pi} \sum_{j \in \mathcal{B}_i} \int_0^{\phi_{i,j}} M_{\gamma_\mathrm{I}} \left[-\frac{w_{i,j} E_\mathrm{s}}{4 N_0 \sin^2(\theta + \psi_{i,j})} \right] d\theta \, , \end{aligned} \tag{4.10}$$

where $M_{\gamma_\mathrm{N}}(s) \triangleq \mathbb{E}\{e^{s \gamma_\mathrm{N}}\}$ is the MGF of γ_I. Finally, the overall error probability can be determined by averaging $\Pr\{\mathrm{e}|s_i\}$ over the *a priori* probability that symbol s_i is transmitted:

$$P_{\mathrm{e,\,ISIC}}(\Gamma) = \sum_{i=1}^{M} p_i \sum_{j \in \mathcal{B}_i} \frac{1}{2\pi} \int_0^{\phi_{i,j}} M_{\gamma_{\mathrm{I}}} \left[-\frac{w_{i,j} E_{\mathrm{s}}}{4 N_0 \sin^2(\theta + \psi_{i,j})} \right] d\theta \,. \tag{4.11}$$

The subscript ISIC means "ideal selection with ideal combining" and is used to indicate that both the selection process and combining mechanism are based on perfect knowledge of the channel. Note that the expression in (4.11) is valid for SSD in IID Rayleigh fading with an arbitrary two-dimensional signaling constellation: we simply need to characterize the MGF of γ_{I} in Sec. 4.2.3.

4.2.2 Non-ideal Selection and Combining

We begin by determining the SEP conditioned on the set of channel estimates as determined by the index set $\mathcal{O}_{\mathrm{N}}$ through the selection vector $\boldsymbol{a}$. Then we average over the distribution of the channel estimates to obtain the unconditional SEP. This analysis is valid when the receiver makes decisions based on a minimum distance criterion.

Conditional SEP

The decision variable, D, is given by

$$D = \sum_{k \in \mathcal{O}_{\mathrm{N}}} \hat{h}_k^* r_k = \sum_{k \in \mathcal{O}_{\mathrm{N}}} \hat{h}_k^* \left[\left(\hat{h}_k - e_k \right) s_i + n_k \right] , \tag{4.12}$$

where we have used the fact that $\hat{h}_k = h_k + e_k$. It is convenient to define the set $\mathcal{S}_{\mathrm{N}}$ which consists of the channel estimates for the branches included in the combining process as

$$\mathcal{S}_{\mathrm{N}} \triangleq \left\{ \hat{h}_k : k \in \mathcal{O}_{\mathrm{N}} \right\} .$$

Theorem 2. *The decision variable, D, when conditioned on the set $\mathcal{S}_N$ and the transmitted symbol s_i, is a circularly symmetric complex Gaussian RV with conditional mean and*

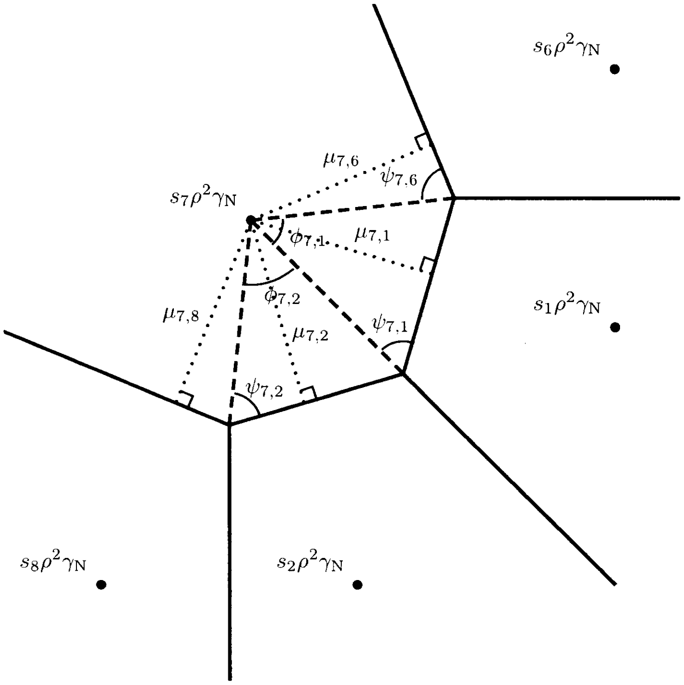

Figure 4-2: A portion of the received signal constellation, and its associated decision regions.

variance given by

$$\mathbb{E}\{D|\,\mathcal{S}_N,\, s_i\} = s_i\rho^2\gamma_N \tag{4.13}$$

$$\begin{aligned}\mathbb{V}\{D|\,\mathcal{S}_N,\, s_i\} &= \mathbb{V}\{\Re\{D\}\,|\,\mathcal{S}_N,\, s_i\} + \mathbb{V}\{\Im\{D\}\,|\,\mathcal{S}_N,\, s_i\} \\ &= 2\left(\frac{N_0}{2} + |s_i|^2\,\sigma_e^2\rho^2\right)\gamma_N,\end{aligned} \tag{4.14}$$

where $\gamma_N = \sum_{k\in\mathcal{O}_N}\left|\hat{h}_k\right|^2$ *and we have defined* $\rho^2 \triangleq \frac{\sigma_h^2}{\sigma_e^2+\sigma_h^2}$.

Proof. See the Appendix A. ☐

Note that the set $\mathcal{S}_{\mathrm{N}}$ consists of the channel *estimates* included in the combining process; that is, the choice of which branches are combined is solely based on the receiver's knowledge of the channel. This differs from conventional analyses where it is often assumed that the receiver has perfect knowledge of the channel. In general, a set of branches chosen based on the noisy estimates may be different from a set chosen based on the true channel gains. Such a difference is important to include in the analysis of a practical diversity system.

The result of Thm. 2 indicates that the received signaling constellation has points of the original transmitted signaling constellation scaled by a factor $\rho^2\gamma_{\mathrm{N}}$. In general, for an arbitrary two-dimensional signaling constellation, the decision variable can be represented in polar form as $D = R\,e^{j\Theta}$ and we can write the conditional SEP as [48, 49]

$$\Pr\{\mathrm{e}|\mathcal{S}_{\mathrm{N}},\, s_i\} = \sum_{j\in\mathcal{B}_i} \int_0^{\phi_{i,j}} \int_{r_{i,j}(\theta)}^{\infty} f_{R,\Theta|\mathcal{S}_{\mathrm{N}}}(r,\theta)\, dr\, d\theta\,, \tag{4.15}$$

where $\mathcal{B}_i$ is the set consisting of the indices for the signaling points that share a decision boundary with s_i and $f_{R,\Theta|\mathcal{S}_{\mathrm{N}}}(r,\theta)$ is the joint distribution of the magnitude and phase of the decision variable D given $\mathcal{S}_{\mathrm{N}}$. The computation in (4.15) can be interpreted in the following way. The error probability conditioned on the set of channel fading gains and a particular transmitted symbol s_i can be determined by integrating wedge-like regions corresponding to each neighbor sharing a decision boundary with s_i. The resulting probability is the probability that the received decision variable is closer to a neighboring symbol than the one actually transmitted, and hence the receiver will make an error. For example, in Fig. 4-2 the point corresponding to s_7 has four neighbors, with each neighbor giving rise to a wedge-like region. If, assuming s_7 was transmitted, the decision variable crosses any of the perpendicular bisectors of the lines drawn between s_7 and its four neighbors, an error will occur.

Since $D|\mathcal{S}_{\mathrm{N}}$ is a complex, circularly symmetric Gaussian RV, R and Θ are conditionally independent, and

$$f_{R,\Theta|\mathcal{S}_{\mathrm{N}}}(r,\theta) = \frac{r}{2\pi\sigma^2}\exp\left[-\frac{r^2}{2\sigma^2}\right], \qquad 0 \le \theta < 2\pi\,, \tag{4.16}$$

where $\sigma^2 = \left(\frac{N_0}{2} + |s_i|^2\,\sigma_e^2\rho^2\right)\gamma_{\mathrm{N}}$. Substituting (4.16) into (4.15) gives

$$\Pr\{\mathrm{e}|\mathcal{S}_{\mathrm{N}},\, s_i\} = \frac{1}{2\pi}\sum_{j\in\mathcal{B}_i}\int_0^{\phi_{i,j}} \exp\left[-\frac{\mu_{i,j}^2}{2\sigma^2\sin^2(\theta+\psi_{i,j})}\right] d\theta\,, \tag{4.17}$$

where we have used $r_{i,j}(\theta) = \frac{\mu_{i,j}}{\sin(\theta+\psi_{i,j})}$ and $\phi_{i,j}$, $\psi_{i,j}$ are angles that describe the decision region corresponding to s_i (see Fig. 4-2 for an example[3]). Using the law of cosines, the

---

[3] Note that the decision region for s_7 is semi-infinite, that is, there are no boundaries to the upper left. For the purposes of calculation of (4.17) in this special case, we use $\phi_{7,6} = \pi - \psi_{7,6}$, $\phi_{7,8} = \pi - \sin^{-1}\left(\frac{\mu_{7,8}}{\mu_{7,2}}\sin\psi_{7,2}\right)$, and $\psi_{7,8} = 0$.

quantity $\mu_{i,j}$ is related to the transmitted signal points after reception as

$$\mu_{i,j} = \frac{1}{2}\sqrt{E_{\mathrm{s}} w_{i,j}}\rho^2 \gamma_{\mathrm{N}} \,,$$

where $w_{i,j} = \xi_i + \xi_j - 2\sqrt{\xi_i \, \xi_j} \cos(\theta_i - \theta_j)$ and the signal points are represented in polar form as $s_i = \sqrt{\xi_i E_{\mathrm{s}}}\, e^{j\theta_i}$ with $\xi_i \triangleq \frac{E_i}{E_{\mathrm{s}}}$. Simplifying gives

$$\Pr\{\mathrm{e}|\mathcal{S}_{\mathrm{N}},\, s_i\} = \frac{1}{2\pi} \sum_{j \in \mathcal{B}_i} \int_0^{\phi_{i,j}} \exp\left[-\gamma_{\mathrm{N}} \frac{w_{i,j} E_{\mathrm{s}} \rho^4}{8\left(\frac{N_0}{2} + |s_i|^2 \sigma_e^2 \rho^2\right) \sin^2(\theta + \psi_{i,j})} \right] d\theta \,. \tag{4.18}$$

Exact SEP

Since the conditional SEP in (4.18) depends on $\mathcal{S}_{\mathrm{N}}$ only through γ_{N}, the SEP is found by averaging (4.18) over the distribution of γ_{N}:

$$\begin{aligned} \Pr\{\mathrm{e}|s_i\} &= \frac{1}{2\pi} \sum_{j \in \mathcal{B}_i} \int_0^{\infty} \int_0^{\phi_{i,j}} \exp\left[-x \frac{w_{i,j} E_{\mathrm{s}} \rho^4}{8\left(\frac{N_0}{2} + |s_i|^2 \sigma_e^2 \rho^2\right) \sin^2(\theta + \psi_{i,j})} \right] f_{\gamma_{\mathrm{N}}}(x)\, d\theta\, dx \\ &= \frac{1}{2\pi} \sum_{j \in \mathcal{B}_i} \int_0^{\phi_{i,j}} M_{\gamma_{\mathrm{N}}} \left[-\frac{w_{i,j} E_{\mathrm{s}} \rho^4}{8\left(\frac{N_0}{2} + |s_i|^2 \sigma_e^2 \rho^2\right) \sin^2(\theta + \psi_{i,j})} \right] d\theta \,, \end{aligned} \tag{4.19}$$

where $M_{\gamma_{\mathrm{N}}}(s) \triangleq \mathbb{E}\{e^{s\,\gamma_{\mathrm{N}}}\}$ is the MGF of γ_{N}. The overall error probability can be determined by averaging $\Pr\{\mathrm{e}|s_i\}$ over the *a priori* probability that symbol s_i is transmitted:

$$P_{\mathrm{e,\,NSNC}}(\Gamma) = \sum_{i=1}^{M} p_i \sum_{j \in \mathcal{B}_i} \frac{1}{2\pi} \int_0^{\phi_{i,j}} M_{\gamma_{\mathrm{N}}} \left[-\frac{w_{i,j} \Upsilon_i(\Gamma) \frac{\rho^2}{\sigma_h^2}}{8 \sin^2(\theta + \psi_{i,j})} \right] d\theta \,, \tag{4.20}$$

where

$$\Upsilon_i(\Gamma) \triangleq \frac{\Gamma N_{\mathrm{p}}\, \varepsilon}{\frac{1}{\Gamma} + N_{\mathrm{p}}\, \varepsilon + \xi_i} \,,$$

and $\Gamma = \mathbb{E}\left\{|h_k|^2\right\} \frac{E_{\mathrm{s}}}{N_0}$ is the average SNR per branch. The subscript NSNC denotes "non-ideal selection with non-ideal combining" and indicates that both the branch selection process and combining mechanism are based solely on the estimated channel knowledge. Note that the expression in (4.20) is valid for SSD in IID Rayleigh fading with an arbitrary two-dimensional signaling constellation: we simply need to characterize the MGF of γ_{N} in

4.2.3 Expressions for the Moment Generating Function of γ_{I} and γ_{N}

Regardless of the selection mechanism, whether ideal or non-ideal, we are interested in finding the MGF of γ, $M_\gamma(\cdot)$, where

$$\gamma = \langle \boldsymbol{a},\, \boldsymbol{z}_{[N]} \rangle$$
$$\boldsymbol{z}_{[N]} \triangleq [z_{[1]} \;\; z_{[2]} \;\; \cdots \;\; z_{[N]}]^T$$

and $\{z_{[i]}\}$ is the ordered set of $\{z_i\}$, denoting the squared magnitudes of IID complex Gaussian RVs, such that $z_{[1]} > z_{[2]} > \ldots > z_{[N]}$.

In general direct analysis of γ is prohibitively complicated, involving N nested integrals. However, this can be alleviated by applying the results of the Virtual Branch technique [46], which will be reviewed below. The ordered set of squared magnitudes, $\boldsymbol{z}_{[N]}$, can be related to a new set of *virtual branch* squared magnitudes, V_n's, using

$$\boldsymbol{z}_{[N]} = \mathbf{T}_{\mathrm{VB}} \boldsymbol{V}_N,$$

where $\mathbf{T}_{\mathrm{VB}} : \mathbb{R}^N \to \mathbb{R}^N$ is the upper triangular virtual branch transformation matrix given by

$$\mathbf{T}_{\mathrm{VB}} = \begin{bmatrix} 1 & \frac{1}{2} & \cdots & \frac{1}{N} \\ & \frac{1}{2} & \cdots & \frac{1}{N} \\ & & \ddots & \vdots \\ & & & \frac{1}{N} \end{bmatrix} \tag{4.21}$$

and $\boldsymbol{V}_N \triangleq [V_1,\, V_2,\, \ldots,\, V_N]^T$. Since $\mathbf{T}_{\mathrm{VB}}$ is upper triangular, the Jacobian of the transformation is easily obtained, and one can then show that the virtual branch variables are IID with MGF given by

$$M_{V_n}(s) \triangleq \mathbb{E}\{e^{s\,V_n}\} = \frac{1}{1 - \mathbb{E}\{z_n\}\, s}\,.$$

Noting that $\gamma = \langle \boldsymbol{a},\, \mathbf{T}_{\mathrm{VB}} \boldsymbol{V}_N \rangle$ and using the fact that the virtual branch variables are independent, it can be shown that

$$M_{\gamma}(s) = \prod_{n=1}^{N} M_{V_n}(b_n s)\,,$$

where b_n is the nth element of $\boldsymbol{b} = \boldsymbol{T}_{\mathrm{VB}}^{T}\boldsymbol{a}$. Applying the above result to the case of ideal and non-ideal selection, respectively, gives:

$$M_{\gamma_{\mathrm{I}}}(s) = \prod_{n=1}^{N_{\mathrm{d}}} \frac{1}{1 - \mathbb{E}\left\{|h|^2\right\} b_n s} = \prod_{n=1}^{N_{\mathrm{d}}} \frac{1}{1 - 2\sigma_h^2 b_n s} \tag{4.22}$$

$$M_{\gamma_{\mathrm{N}}}(s) = \prod_{n=1}^{N_{\mathrm{d}}} \frac{1}{1 - \mathbb{E}\left\{\left|\hat{h}\right|^2\right\} b_n s} = \prod_{n=1}^{N_{\mathrm{d}}} \frac{1}{1 - 2\frac{\sigma_h^2}{\rho^2} b_n s}\,, \tag{4.23}$$

where b_n is the nth element of the vector $\boldsymbol{b}$.

4.2.4 Error Probability Expressions

Using the results of Secs. 4.2.2–4.2.3, expressions for the exact SEP of SSD with ISIC and NSNC in Rayleigh fading can be formulated. These expressions can also be specialized for specific modulation formats, such as M-PSK and M-QAM.

In particular, combining (4.11) and (4.22) yields the exact SEP for ISIC

$$P_{\mathrm{e,\,ISIC}}(\Gamma) = \sum_{i=1}^{M} p_i \sum_{j \in \mathcal{B}_i} \frac{1}{2\pi} \int_0^{\phi_{i,j}} \prod_{n=1}^{N_{\mathrm{d}}} \left(1 + b_n \frac{w_{i,j}\Gamma}{4\sin^2(\theta + \psi_{i,j})}\right)^{-1} d\theta \tag{4.24}$$

Similarly, combining (4.20) and (4.23) gives the exact SEP for NSNC

$$P_{\mathrm{e,\,NSNC}}(\Gamma) = \sum_{i=1}^{M} p_i \sum_{j \in \mathcal{B}_i} \frac{1}{2\pi} \int_0^{\phi_{i,j}} \prod_{n=1}^{N_{\mathrm{d}}} \left(1 + b_n \frac{w_{i,j}\Upsilon_i(\Gamma)}{4\sin^2(\theta + \psi_{i,j})}\right)^{-1} d\theta \tag{4.25}$$

We can further specialize (4.25) for the cases of M-PSK and M-QAM. For the case of M-PSK, where the symbols have equal energy, (4.25) reduces to[4]

$$P_{\mathrm{e,\,NSNC}}^{\mathrm{MPSK}}(\Gamma) = \frac{1}{\pi} \int_0^{\frac{M-1}{M}\pi} \prod_{n=1}^{N_{\mathrm{d}}} \left(1 + b_n \frac{\Upsilon(\Gamma)\, c_{\mathrm{MPSK}}}{\sin^2\theta}\right)^{-1} d\theta\,, \tag{4.26}$$

---

[4] For M-PSK $\xi_i = 1\ \forall i$, thus $\Upsilon_i(\Gamma)$ does not depend on i, in which case we simply write $\Upsilon(\Gamma)$.

where $c_{\mathrm{MPSK}} = \sin^2(\frac{\pi}{M})$. Note that in (4.26) we have used the fact that $w_{i,j} = 2 - 2\cos\left(\frac{2\pi}{M}\right) = 4\sin^2(\frac{\pi}{M})$. For the case of M-QAM,

$$P_{\mathrm{e,\,NSNC}}^{\mathrm{MQAM}}(\Gamma) = \frac{1}{M}\sum_i \frac{\omega_i^{\mathrm{a}}}{2\pi}\int_0^{\frac{\pi}{2}} \prod_{n=1}^{N_{\mathrm{d}}} \left(1 + b_n \frac{\Upsilon_i(\Gamma)\, c_{\mathrm{MQAM}}}{\sin^2\left(\theta + \frac{\pi}{4}\right)}\right)^{-1} d\theta$$
$$+ \frac{\omega_i^{\mathrm{b}}}{2\pi}\int_0^{\frac{3\pi}{4}} \prod_{n=1}^{N_{\mathrm{d}}} \left(1 + b_n \frac{\Upsilon_i(\Gamma)\, c_{\mathrm{MQAM}}}{\sin^2\theta}\right)^{-1} d\theta\,, \tag{4.27}$$

where $c_{\mathrm{MQAM}} = 3/(2(M-1))$ and ω_i^{a}, ω_i^{b}, and ξ_i are given in Table 4.1 for $M = \{4,\, 16,\, 64,\, 256\}$. Note that the summation in (4.27) is performed over the nonzero terms given in Table 4.1 in the column corresponding to a particular value of M. Eqn. (4.24) may also be specialized for the cases of M-PSK and M-QAM. The results will be identical to those in (4.26) and (4.27) with $\Upsilon(\Gamma)$ and $\Upsilon_i(\Gamma)$ replaced by Γ.

4.2.5 Special Cases

In this section we characterize the SEP for SSD with non-ideal selection and combining for a few specific selection policies. Specifically, we examine the case of H-S/MRC, MRC, and SD.

H-S/MRC

In H-S/MRC the receiver combines the signals from the L_{d} antennas with the largest estimated channel gain magnitude out of N_{d} available antennas. For this selection policy

$$\mathbf{a} = [\underbrace{1\ 1\ \cdots\ 1}_{L_{\mathrm{d}}\ \text{terms}}\ 0\ 0\ \cdots\ 0]^T$$

and

$$b_n = \begin{cases} 1\,, & n \le L_{\mathrm{d}} \\ \frac{L_{\mathrm{d}}}{n}\,, & \text{otherwise.} \end{cases}$$

i	ξ_i				ω_i^{a}	ω_i^{b}
	$M = 4$	$M = 16$	$M = 64$	$M = 256$		
1	1	9/5	7/3	45/17	0	8
2		1	37/21	197/85	8	16
3		1/5	25/21	169/85	16	0
4			29/21	173/85	8	16
5			17/21	29/17	32	0
6			3/7	121/85	16	0
7			25/21	9/5	8	16
8			13/21	25/17	32	0
9			5/21	101/85	32	0
10			1/21	81/85	16	0
11				137/85	8	16
12				109/85	32	0
13				1	32	0
14				13/17	32	0
15				49/85	16	0
16				25/17	8	16
17				97/85	32	0
18				73/85	32	0
19				53/85	32	0
20				37/85	32	0
21				5/17	16	0
22				117/85	8	16
23				89/85	32	0
24				13/17	32	0
25				9/17	32	0
26				29/85	32	0
27				1/5	32	0
28				9/85	16	0
29				113/85	8	16
30				1	32	0
31				61/85	32	0
32				41/85	32	0
33				5/17	32	0
34				13/85	32	0
35				1/17	32	0
36				1/85	16	0

Table 4.1: Parameters for MQAM signaling constellations

	MPSK	MQAM
H-S/MRC	$\frac{1}{\pi}\int_0^{\frac{M-1}{M}\pi}\left(1+\frac{\Upsilon(\Gamma)\,c_{\mathrm{MPSK}}}{\sin^2\theta}\right)^{-L_{\mathrm{d}}}$ $\times\prod_{n=L_{\mathrm{d}}+1}^{N_{\mathrm{d}}}\left(1+\frac{L_{\mathrm{d}}}{n}\frac{\Upsilon(\Gamma)\,c_{\mathrm{MPSK}}}{\sin^2\theta}\right)^{-1}d\theta$	$\frac{1}{M}\sum_i\frac{\omega_i^{\mathrm{a}}}{2\pi}\int_0^{\frac{\pi}{2}}\left(1+\frac{\Upsilon_i(\Gamma)\,c_{\mathrm{MQAM}}}{\sin^2\left(\theta+\frac{\pi}{4}\right)}\right)^{-L_{\mathrm{d}}}$ $\times\prod_{n=L_{\mathrm{d}}+1}^{N_{\mathrm{d}}}\left(1+\frac{L_{\mathrm{d}}}{n}\frac{\Upsilon_i(\Gamma)\,c_{\mathrm{MQAM}}}{\sin^2\left(\theta+\frac{\pi}{4}\right)}\right)^{-1}d\theta$ $+\frac{\omega_i^{\mathrm{b}}}{2\pi}\int_0^{\frac{3\pi}{4}}\left(1+\frac{\Upsilon_i(\Gamma)\,c_{\mathrm{MQAM}}}{\sin^2\theta}\right)^{-L_{\mathrm{d}}}$ $\times\prod_{n=L_{\mathrm{d}}+1}^{N_{\mathrm{d}}}\left(1+\frac{L_{\mathrm{d}}}{n}\frac{\Upsilon_i(\Gamma)\,c_{\mathrm{MQAM}}}{\sin^2\theta}\right)^{-1}d\theta$
MRC	$\frac{1}{\pi}\int_0^{\frac{M-1}{M}\pi}\left(1+\frac{\Upsilon(\Gamma)\,c_{\mathrm{MPSK}}}{\sin^2\theta}\right)^{-N_{\mathrm{d}}}d\theta$	$\frac{1}{M}\sum_i\frac{\omega_i^{\mathrm{a}}}{2\pi}\int_0^{\frac{\pi}{2}}\left(1+\frac{\Upsilon_i(\Gamma)\,c_{\mathrm{MQAM}}}{\sin^2\left(\theta+\frac{\pi}{4}\right)}\right)^{-N_{\mathrm{d}}}d\theta$ $+\frac{\omega_i^{\mathrm{b}}}{2\pi}\int_0^{\frac{3\pi}{4}}\left(1+\frac{\Upsilon_i(\Gamma)\,c_{\mathrm{MQAM}}}{\sin^2\theta}\right)^{-N_{\mathrm{d}}}d\theta$
SD	$\frac{1}{\pi}\int_0^{\frac{M-1}{M}\pi}\left(1+\frac{\Upsilon(\Gamma)\,c_{\mathrm{MPSK}}}{\sin^2\theta}\right)^{-1}$ $\times\prod_{n=2}^{N_{\mathrm{d}}}\left(1+\frac{1}{n}\frac{\Upsilon(\Gamma)\,c_{\mathrm{MPSK}}}{\sin^2\theta}\right)^{-1}d\theta$	$\frac{1}{M}\sum_i\frac{\omega_i^{\mathrm{a}}}{2\pi}\int_0^{\frac{\pi}{2}}\left(1+\frac{\Upsilon_i(\Gamma)\,c_{\mathrm{MQAM}}}{\sin^2\left(\theta+\frac{\pi}{4}\right)}\right)^{-1}$ $\times\prod_{n=2}^{N_{\mathrm{d}}}\left(1+\frac{1}{n}\frac{\Upsilon_i(\Gamma)\,c_{\mathrm{MQAM}}}{\sin^2\left(\theta+\frac{\pi}{4}\right)}\right)^{-1}d\theta$ $+\frac{\omega_i^{\mathrm{b}}}{2\pi}\int_0^{\frac{3\pi}{4}}\left(1+\frac{\Upsilon_i(\Gamma)\,c_{\mathrm{MQAM}}}{\sin^2\theta}\right)^{-1}$ $\times\prod_{n=2}^{N_{\mathrm{d}}}\left(1+\frac{1}{n}\frac{\Upsilon_i(\Gamma)\,c_{\mathrm{MQAM}}}{\sin^2\theta}\right)^{-1}d\theta$

Table 4.2: Expressions for $P_{\mathrm{e,\,NSNC}}(\Gamma)$ under specific selection policies and modulation formats

Using the resulting b_n gives

$$P_{\mathrm{e,\,H\text{-}S/MRC}}(\Gamma) = \sum_{i=1}^{M} p_i \sum_{j \in \mathcal{B}_i} \frac{1}{2\pi} \int_0^{\phi_{i,j}} \left(1 + \frac{w_{i,j} \Upsilon_i(\Gamma)}{4\sin^2(\theta + \psi_{i,j})}\right)^{-L_\mathrm{d}} \times \prod_{n=L_\mathrm{d}+1}^{N_\mathrm{d}} \left(1 + \frac{L_\mathrm{d}}{n} \frac{w_{i,j} \Upsilon_i(\Gamma)}{4\sin^2(\theta + \psi_{i,j})}\right)^{-1} d\theta \,. \tag{4.28}$$

For MPSK and MQAM signaling, (4.28) reduces to the expressions shown in Table 4.2.

MRC

In the case of MRC, the receiver combines the signals from all the available antennas. This selection policy amounts to setting $\mathbf{a}$ to a vector of ones;

$$\mathbf{a} = [\underbrace{1 \;\; 1 \;\; \cdots \;\; 1}_{L_\mathrm{d} = N_\mathrm{d} \text{ terms}}]^T ,$$

giving $b_n = 1 \;\; \forall n$. Using this selection policy gives

$$P_{\mathrm{e,\,MRC}}(\Gamma) = \sum_{i=1}^{M} p_i \sum_{j \in \mathcal{B}_i} \frac{1}{2\pi} \int_0^{\phi_{i,j}} \left(1 + \frac{w_{i,j} \Upsilon_i(\Gamma)}{4\sin^2(\theta + \psi_{i,j})}\right)^{-N_\mathrm{d}} d\theta \,. \tag{4.29}$$

For MPSK and MQAM signaling, (4.29) reduces to the expressions shown in Table 4.2. These results can also be obtained by setting $L_\mathrm{d} = N_\mathrm{d}$ in the equations given for H-S/MRC.

SD

For SD, the receiver uses only the signal from the antenna with the largest estimated channel gain magnitude. This amounts to using the following selection vector

$$\mathbf{a} = [1 \;\; \underbrace{0 \;\; 0 \;\; \cdots \;\; 0}_{N_\mathrm{d} - 1 \text{ terms}}]^T ,$$

and

$$b_n = \begin{cases} 1 \,, & n = 1 \\ \frac{1}{n} \,, & \text{otherwise.} \end{cases}$$

Using this policy, the SEP is given by

$$P_{\mathrm{e,SD}}(\Gamma) = \sum_{i=1}^{M} p_i \sum_{j \in \mathcal{B}_i} \frac{1}{2\pi} \int_0^{\phi_{i,j}} \left(1 + \frac{w_{i,j} \Upsilon_i(\Gamma)}{4 \sin^2(\theta + \psi_{i,j})}\right)^{-1} \times \prod_{n=2}^{N_\mathrm{d}} \left(1 + \frac{1}{n} \frac{w_{i,j} \Upsilon_i(\Gamma)}{4 \sin^2(\theta + \psi_{i,j})}\right)^{-1} d\theta \,. \tag{4.30}$$

For MPSK and MQAM signaling, (4.30) reduces to the expressions shown in Table 4.2. These results can also be obtained by setting $L_\mathrm{d} = 1$ in the equations given for H-S/MRC.

4.3 Analysis for Subset Diversity in Realistic Fading Channels

In this section we give expressions for the SEP for SSD based on both the ideal and non-ideal selection and combining schemes outlined above. These expressions given below are referred to as *semi-analytical.* That is, they involve Monte-Carlo averaging of the analytical conditional probability expressions. As discussed above, those expressions require only the evaluation of single integrals with finite limits.

A Monte-Carlo based approach is necessary since exact expressions for the SEP are difficult to obtain. This is due to fact that the SEP of interest is for operation in channels where the probability distributions of the channel gains are not known. In particular, numerical results given in Sec. 4.4 are based on channel gains extracted from measured channel responses. Furthermore, computation of the MGF for γ_I or γ_N in closed form, as in Section 4.2.3, is in general very difficult for distributions with non-identically distributed components. This method offers some advantages over a purely Monte-Carlo approach. Since it requires the generation of fewer random samples than a purely Monte-Carlo approach, the computational complexity is reduced. Also, since fewer random samples are required, convergence to the true error probability happens more quickly.

The approach taken here is to consider a finite set of channel realizations which have been extracted from measured channel responses. Let $\boldsymbol{h}^{(i)} \in \mathcal{H}$ be a vector of channel gains extracted from a channel realization, where $\mathcal{H}$ is a finite set of channel gain vectors. In this case the SEP can be evaluated as

$$P_{\mathrm{e}} = \frac{1}{|\mathcal{H}|} \sum_{k \in \mathcal{H}} \Pr\left\{ \mathrm{e} | \boldsymbol{h}^{(k)} \right\}, \tag{4.31}$$

where $\Pr\left\{ \mathrm{e} | \boldsymbol{h}^{(k)} \right\}$ is the appropriate expression for the conditional error probability, given a particular channel realization of the system under consideration. In subsequent sections the case of ideal and non-ideal selection and combining will be considered.

4.3.1 Ideal Selection and Combining

For the case of ideal selection and combining the evaluation of $\Pr\left\{ \mathrm{e} | \boldsymbol{h}^{(k)} \right\}$ is straightforward. The SEP is computed by averaging the conditional SEP expression (4.9), which is valid for any distribution of the channel gains, over the signaling constellation:

$$\Pr\left\{ \mathrm{e} | \boldsymbol{h}^{(m)} \right\} = \sum_{i=1}^{M} p_i \Pr\left\{ \mathrm{e} | \mathcal{S}_{\mathrm{I}}^{(m)}, s_i \right\}, \tag{4.32}$$

where $\mathcal{S}_{\mathrm{I}}^{(m)} = \left\{ h_l^{(k)} : l \in \mathcal{O}_{\mathrm{I}} \right\}$. The SEP evaluation procedure for the case of ideal selection and combining is given below in Alg. 2. The procedure can then be repeated to evaluate the SEP at other SNRs of interest.

Algorithm 2 Computation of $P_{\mathrm{e}}(\Gamma)$ for ideal selection and combining

```
Require: A set of channel gain vectors $\mathcal{H}$, a selection vector $\boldsymbol{a}$, and an operating SNR $\Gamma$
$P_{\mathrm{e}} \leftarrow 0$
for $\boldsymbol{h}^{(m)} \in \mathcal{H}$ do
    Determine $\mathcal{O}_{\mathrm{I}}^{(m)}$ based on $\boldsymbol{h}^{(m)}$ and $\boldsymbol{a}$
    $P_{\mathrm{e}} \leftarrow P_{\mathrm{e}} + \frac{1}{|\mathcal{H}|} \Pr\{\mathrm{e}|\boldsymbol{h}^{(m)}\}$        ▷ evaluated using (4.32)
end for
```

4.3.2 Non-ideal Selection and Combining

Evaluating the conditional SEP for the case of non-ideal selection and combining is more difficult. Direct use of (4.18) is not possible, since that expression uses the assumption of Rayleigh distributed channel gains. The approach taken here is to first condition on $\boldsymbol{h}$ and $\boldsymbol{e}$. Then, Monte-Carlo based averaging of the resulting conditional expression over $\boldsymbol{e}$ is used to formulate $\Pr\left\{ \mathrm{e} | \boldsymbol{h}^{(k)} \right\}$ in (4.31).

Conditional SEP

In this section the conditional expressions for the SEP are derived when the decision variable is conditioned on $\boldsymbol{h}$, $\boldsymbol{e}$, and s_i.

Theorem 3. *The decision variable, D, when conditioned on the vectors $\boldsymbol{h}$ and $\boldsymbol{e}$, as well as the transmitted symbol s_i, is a circularly symmetric complex Gaussian RV with conditional mean and variance given by*

$$\mathbb{E}\{D|\,\boldsymbol{h},\,\boldsymbol{e},\,s_i\} = s_i \sum_{k\in\mathcal{O}_N} (h_k + e_k)^* h_k \tag{4.33}$$

$$\begin{aligned}\mathbb{V}\{D|\,\boldsymbol{h},\,\boldsymbol{e},\,s_i\} &= \mathbb{V}\{\Re\{D\}\,|\,\boldsymbol{h},\,\boldsymbol{e},\,s_i\} + \mathbb{V}\{\Im\{D\}\,|\,\boldsymbol{h},\,\boldsymbol{e},\,s_i\} \\ &= N_0 \sum_{k\in\mathcal{O}_N} |h_k + e_k|^2 = N_0\gamma_N\,. \end{aligned} \tag{4.34}$$

Proof. The proof follows from the expansion of D given in (4.5) in terms of $\boldsymbol{h}$ and $\boldsymbol{e}$. When conditioned on $\boldsymbol{h}$ and $\boldsymbol{e}$, the only remaining random quantity in D is the AWGN $\boldsymbol{n}$, which itself is circularly symmetric. □

Using the fact that D is circularly symmetric complex Gaussian RV the conditional error probability can be evaluated using a procedure similar to the one described in Sec. 4.2.2 with a significant modification. The error probability must be computed with respect to the receiver's knowledge, that is, the error probability computation must be based on a decision rule that is available to a receiver which only has knowledge of $\hat{\boldsymbol{h}}$. While the result of Thm. 3 gives the properties of $D|\boldsymbol{h},\,\boldsymbol{e}$, the actual decision boundaries used by the receiver must be based on $D|\hat{\boldsymbol{h}}$. Similar to Sec. 4.2.2, a minimum distance decision rule derived from the set $\left\{\mathbb{E}\left\{D|\hat{\boldsymbol{h}},\,s_i\right\}\right\}_{i=1}^{M}$. The added difficulty in the computation of the SEP in this case comes from the fact that the mean of the decision variable, conditioned on $\boldsymbol{h}$, $\boldsymbol{e}$, and s_i, $\mathbb{E}\{D|\,\boldsymbol{h},\,\boldsymbol{e},\,s_i\}$, may not lie within the decision region for s_i.

For notational convenience the mean of decision variable conditioned on $\hat{\boldsymbol{h}}$ and s_i can be written as

$$\alpha s_i = \mathbb{E}\left\{D|\hat{\boldsymbol{h}}, s_i\right\} = s_i \sum_{k\in\mathcal{O}_\mathrm{N}} \left(\left|\hat{h}_k\right|^2 - \hat{h}_k^*\mathbb{E}\left\{e_k|\hat{h}_k\right\}\right)\,. \tag{4.35}$$

Note that the conditional expectation on the right is the least squares estimate (LSE) of e_k given $\hat{h}_k$. Evaluation of this quantity requires the complete characterization of the joint distribution of e and $\hat{h}$. This was possible when the underlying distribution of h was assumed to be complex Gaussian (as in Sec. 4.2.2), but in the case of using data extracted from measured channel responses this distribution is unknown. Instead, one can consider using the linear least squares estimate (LLSE) [50]:

$$\begin{aligned} LLSE(e_k|\hat{h}_k) &= \mathbb{E}\{e_k\} + \operatorname{Cov}\left\{e_k, \hat{h}_k\right\} \left(\mathbb{V}\left\{\hat{h}_k\right\}\right)^{-1} \left(\hat{h}_k - \mathbb{E}\left\{\hat{h}_k\right\}\right) \\ &= 2\sigma_e^2 \left(\mathbb{V}\left\{\hat{h}_k\right\}\right)^{-1} \left(\hat{h}_k - \mathbb{E}\left\{\hat{h}_k\right\}\right) . \end{aligned} \tag{4.36}$$

Using this expression in place of $\mathbb{E}\left\{e_k \middle| \hat{h}_k\right\}$ in (4.35) gives

$$\alpha = \sum_{k \in \mathcal{O}_{\mathrm{N}}} \left[\left|\hat{h}_k\right|^2 \left(1 - 2\sigma_e^2 \left(\mathbb{V}\left\{\hat{h}_k\right\}\right)^{-1}\right) + 2\sigma_e^2 \mathbb{E}\left\{\hat{h}_k\right\} \left(\mathbb{V}\left\{\hat{h}_k\right\}\right)^{-1} \hat{h}_k^* \right] . \tag{4.37}$$

The quantities $\mathbb{E}\left\{\hat{h}_k\right\}$ and $\mathbb{V}\left\{\hat{h}_k\right\}$ can be calculated by the receiver from data it receives, while the value of σ_e^2 is based on the estimation model considered in Sec. 4.1.3. The mean of decision variable conditioned on $\boldsymbol{h}$, $\boldsymbol{e}$, and s_i can be written as

$$\tilde{\alpha} s_i = \mathbb{E}\{D \big| \boldsymbol{h}, \boldsymbol{e}, s_i\} = s_i \sum_{k \in \mathcal{O}_{\mathrm{N}}} (h_k + e_k)^* h_k . \tag{4.38}$$

The second equality in (4.38) is due to Thm. 3. In general α and $\tilde{\alpha}$ will be complex scalars.

As discussed earlier, the receiver under consideration is one that makes decisions based on a minimum distance criteria. Under this criteria the set of points $\{\alpha s_i\}_{i=1}^{M}$ defines a polygonal decision region for each αs_i. If the decision variable falls within the region corresponding to αs_i, the receiver decides that s_i was transmitted. In this case, however, the SEP computation must taken into account the fact that the mean of the conditional decision variable, $\tilde{\alpha} s_i$, may fall either inside or outside the decision region for αs_i.

Given that s_i was transmitted, the SEP evaluation must integrate the complex Gaussian decision variable D, with mean $\tilde{\alpha} s_i$, over the decision region corresponding to s_i. The SEP computation will utilize integrals of the form

$$\frac{1}{2\pi} \int_0^{\tilde{\phi}_{ij}} \exp\left(- \frac{(\tilde{\mu}_{ij})^2}{2\sigma^2 \sin^2(\theta + \tilde{\psi}_{ij})} \right) d\theta \tag{4.39}$$

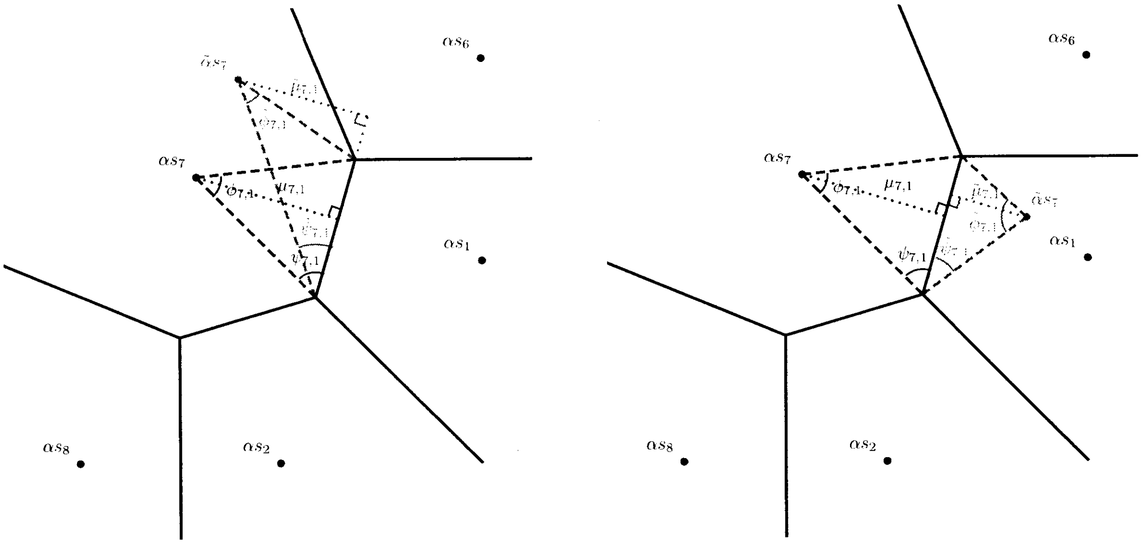

(a) (b)

Figure 4-3: A portion of the received signal constellation, and its associated decision regions for the non-ideal case. In this example, consider the transmission of the symbol s_7. The conditional SEP is computed with respect to the point $\tilde{\alpha} s_7$ which can either fall inside the decision region for s_7 (a), or outside the decision region for s_7 (b).

where $\tilde{\mu}_{ij}$, $\tilde{\psi}_{ij}$ and $\tilde{\phi}_{ij}$ are related to the edge that forms the decision boundary between αs_i and αs_j, and $\sigma^2 = \frac{N_0}{2}\gamma_{\mathrm{N}}$. For an example, see Fig. 4-3. When $\tilde{\alpha} s_i$ falls within the decision region of s_i the above integral is related to the probability that the decision variable falls outside the decision region along that edge. However, when $\tilde{\alpha} s_i$ falls outside the decision region, the above integral is related to the probability that the decision variable crosses the decision boundary into the decision region.

Using this fact, the SEP for an arbitrary two-dimensional signaling constellation, conditioned on a particular $\boldsymbol{h}^{(m)}$, $\boldsymbol{e}^{(n)}$, and s_i, can be shown to be

$$\begin{aligned}\Pr\{\mathrm{e}|\boldsymbol{h}^{(m)}, \boldsymbol{e}^{(n)}, s_i\} = \mathbb{1}&_{\left\{\bigcup_{j\in\mathcal{B}_i} f_{ij}(\alpha,\tilde{\alpha})<0\right\}} \\ &+ \frac{1}{2\pi}\sum_{j\in\mathcal{B}_i} f_{ij}(\alpha,\tilde{\alpha}) \int_0^{\tilde{\phi}_{ij}} \exp\left(-\frac{(\tilde{\mu}_{ij})^2}{2\sigma^2\sin^2(\theta+\tilde{\psi}_{ij})}\right) d\theta \end{aligned} \tag{4.40}$$

where, for a proposition A,

$$\mathbb{1}_{\{A\}} = \begin{cases} 1, & \text{if } A \text{ is true,} \\ 0, & \text{otherwise} \end{cases} \tag{4.41}$$

and

$$f_{ij}(\alpha,\tilde{\alpha}) = \operatorname{sgn}\left(|\alpha s_j - \tilde{\alpha} s_i|^2 - |\alpha - \tilde{\alpha}|^2 |s_i|^2\right) \tag{4.42}$$

where $\operatorname{sgn}(x)$ denotes the sign of x. The function $f_{ij}(\alpha,\tilde{\alpha}) \geq 0$ denotes that $\tilde{\alpha} s_i$ and αs_i are on same side of the decision boundary shared by αs_i and αs_j. If $\tilde{\alpha} s_i$ is on the same side as αs_i for all the boundaries of the decision region for s_i, the first term in (4.40), $\mathbb{1}_{\left\{\bigcup_{j\in\mathcal{B}_i} f_{ij}(\alpha,\tilde{\alpha})<0\right\}}$, is equal to zero, and the second term, i.e., the summation, is $\Pr\left\{\mathrm{e}\middle|\,\boldsymbol{h}^{(m)},\, \boldsymbol{e}^{(n)},\, s_i\right\}$. If there are one or more boundaries for which $\tilde{\alpha} s_i$ and αs_i are not on the same side, i.e., $\tilde{\alpha} s_i$ lies outside the decision region for s_i, the first term becomes 1, and the second term is equal to $-\left(1 - \Pr\left\{\mathrm{e}\middle|\,\boldsymbol{h}^{(m)},\, \boldsymbol{e}^{(n)},\, s_i\right\}\right)$.

The three parameters $\tilde{\mu}_{ij}$, $\tilde{\psi}_{ij}$ and $\tilde{\phi}_{ij}$ in (4.40) are defined as

$$\tilde{\mu}_{ij} = \frac{1}{4\mu_{ij}} \left| |\alpha s_j - \tilde{\alpha} s_i|^2 - |\alpha - \tilde{\alpha}|^2 |s_i|^2 \right| \tag{4.43}$$

$$\tilde{\psi}_{ij} = \arccos\left(\frac{\Re\left\{(v_{ij}^1)^* v_{ij}^2\right\}}{\left|v_{ij}^1\right| \left|v_{ij}^2\right|}\right) \tag{4.44}$$

$$\tilde{\phi}_{ij} = \arccos\left(\frac{\Re\left\{(v_{ij}^2)^* v_{ij}^3\right\}}{\left|v_{ij}^2\right| \left|v_{ij}^3\right|}\right) \tag{4.45}$$

where

$$v_{ij}^1 = -\jmath\alpha(s_j - s_i) \tag{4.46}$$

$$v_{ij}^2 = -\jmath\alpha(s_j - s_i) + [(\alpha - 2\tilde{\alpha})s_i + \alpha s_j]\tan\psi_{ij} \tag{4.47}$$

$$v_{ij}^3 = \jmath\alpha(s_j - s_i) + [(\alpha - 2\tilde{\alpha})s_i + \alpha s_j]\tan(\pi - \phi_{ij} - \psi_{ij}) \tag{4.48}$$

are direction vectors. The first vector v_{ij}^1 is the vector that points from αs_i to αs_j rotated 90 degrees clockwise. The second and third vectors are point from $\tilde{\alpha} s_i$ to the vertices of edge shared between αs_i and αs_j. Equations (4.47) and (4.48) require the value of ψ_{ij} and ϕ_{ij}. Note that for a given pair of s_i and s_j, there exist two possible values of ψ_{ij} since each edge of the decision boundary has two vertices. The ψ_{ij} used in (4.47) and (4.48) is the angle associated with the vertex which is pointed to by $-\jmath\alpha(s_j - s_i)$. If the vertex is at infinity, we let $\psi_{ij} = 0$. This is equivalent to choosing the angle to be the one associated with the first vertex of the edge when visiting each edge of the decision region for αs_i in a counter-clockwise direction.

Finally, the conditional error probability averaged over the signaling points is then given by

$$\Pr\{\mathrm{e}|\boldsymbol{h}^{(m)}, \boldsymbol{e}^{(n)}\} = \sum_{i=1}^{M} p_i \Pr\{\mathrm{e}|\boldsymbol{h}^{(m)}, \boldsymbol{e}^{(n)}, s_i\}\,. \tag{4.49}$$

Evaluation Procedure

The evaluation procedure for the case of non-ideal selection and combining is given below in Alg. 3. The procedure can then be repeated to evaluate the SEP at other SNRs of interest.

Algorithm 3 Computation of $P_\mathrm{e}(\Gamma)$ for non-ideal selection and combining

```
Require: A set of channel gain vectors $\mathcal{H}$, a selection vector $\boldsymbol{a}$, and an operating SNR $\Gamma$
$P_\mathrm{e} \leftarrow 0$
for $\boldsymbol{h}^{(m)} \in \mathcal{H}$ do
    $P_{\mathrm{e}|h} \leftarrow 0$
    Generate a set of error vectors $\mathcal{E}$                          ▷ according to Sec. 4.1.3
    for $\boldsymbol{e}^{(n)} \in \mathcal{E}$ do
        Determine $\mathcal{O}_\mathrm{N}$ based on $\hat{\boldsymbol{h}} = \boldsymbol{h}^{(m)} + \boldsymbol{e}^{(n)}$, and $\boldsymbol{a}$
        Determine $\alpha$ and $\tilde{\alpha}$ based on $\mathcal{O}_\mathrm{N}$                    ▷ using (4.37) and (4.38)
        $P_{\mathrm{e}|h} \leftarrow P_{\mathrm{e}|h} + \frac{1}{|\mathcal{E}|}\Pr\{\mathrm{e}|\boldsymbol{h}^{(m)}, \boldsymbol{e}^{(n)}\}$                ▷ using (4.49)
    end for
    $P_\mathrm{e} \leftarrow P_\mathrm{e} + \frac{1}{|\mathcal{H}|} P_{\mathrm{e}|h}$
end for
```

4.4 Numerical Results and Discussion

This section gives numerical results for the SEP for RSSD in wideband channels. First comparisons are made between the semi-analytical expressions in Secs. 4.3 and the exact analytical results in Secs. 4.2 to show the efficacy of our semi-analytical approach. Then, empirical results for the number of multipath components, N_d, present in the measured channel responses are discussed. Finally, detailed SEP results are given for four representative locations in the measurement environment. The results are based on channel parameters, the path delays and amplitudes, extract from the measured waveforms using the method described in Sec. 3.4.3. In this section, the analysis will focus on four representative locations: A, G, M, and O. Locations A and G are both LOS, with G short range

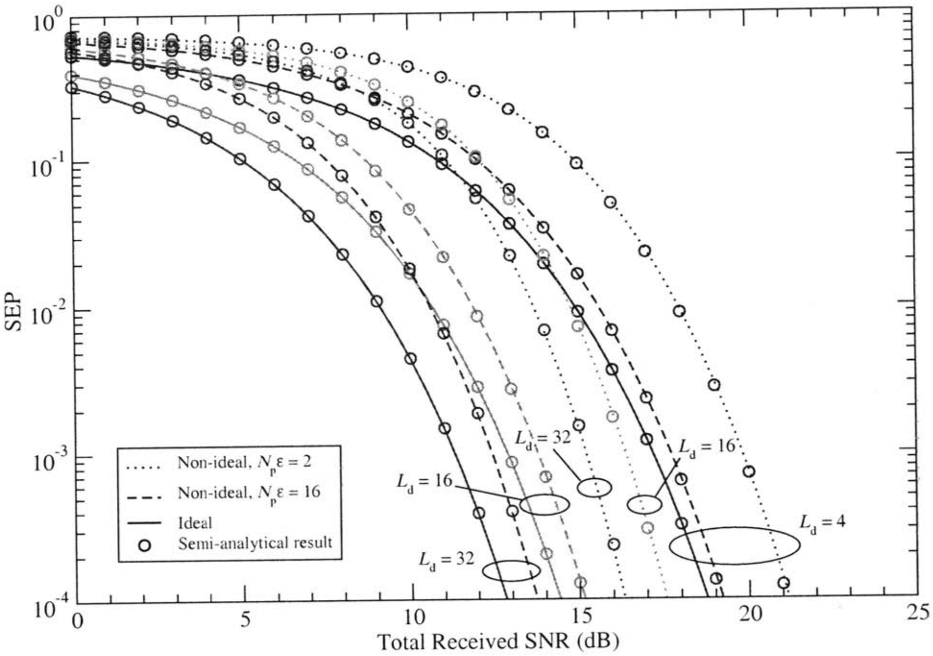

Figure 4-4: Exact analytical and semi-analytical SEP results for IID Rayleigh fading with $N_\mathrm{d} = 64$ paths, $L_\mathrm{d} = 4$, 16, 32 and $N_\mathrm{p}\,\varepsilon = 2$, 16. Semi-analytical results agree with exact analytical expressions.

and A long range. Locations M and O are NLOS, with M short range and O long range.

4.4.1 Comparison between Exact Analytical and Semi-analytical Results

To show that the semi-analytical expressions developed in Sec. 4.3 agree with the exact analytical results of Sec. 4.2, comparisons between the two are made for the case of IID Rayleigh fading channels. Specifically, Fig. 4-4 considers the case of QPSK transmission in channels with $N_\mathrm{d} = 64$ paths and $L_\mathrm{d} = 4$, 16, and 32 paths for both ISIC and NSNC. For the semi-analytical case, 5000 channel vectors were generated to evaluate the performance of ISIC, while 100 channel vectors and 50 error vectors were generated to evaluate the performance of NSNC. In the NSNC case, $N_\mathrm{p}\,\varepsilon = 2$ and 16 are considered. The quantity $N_\mathrm{p}\,\varepsilon$ can be viewed as the energy devoted to estimation of the channel gains. When $\varepsilon = 1$, this quantity corresponds to the transmission of N_p pilot symbols with energy equal to the data symbols. The figure shows that in all cases the semi-analytical results, indicated by circles, closely agree with the exact analytical expressions. From the figure, one can also note that as the quantity $N_\mathrm{p}\,\varepsilon$ increases, the NSNC curves approach the ISIC curves. This behavior was discussed in [51], and quantified in detail for a variety of systems in [52].

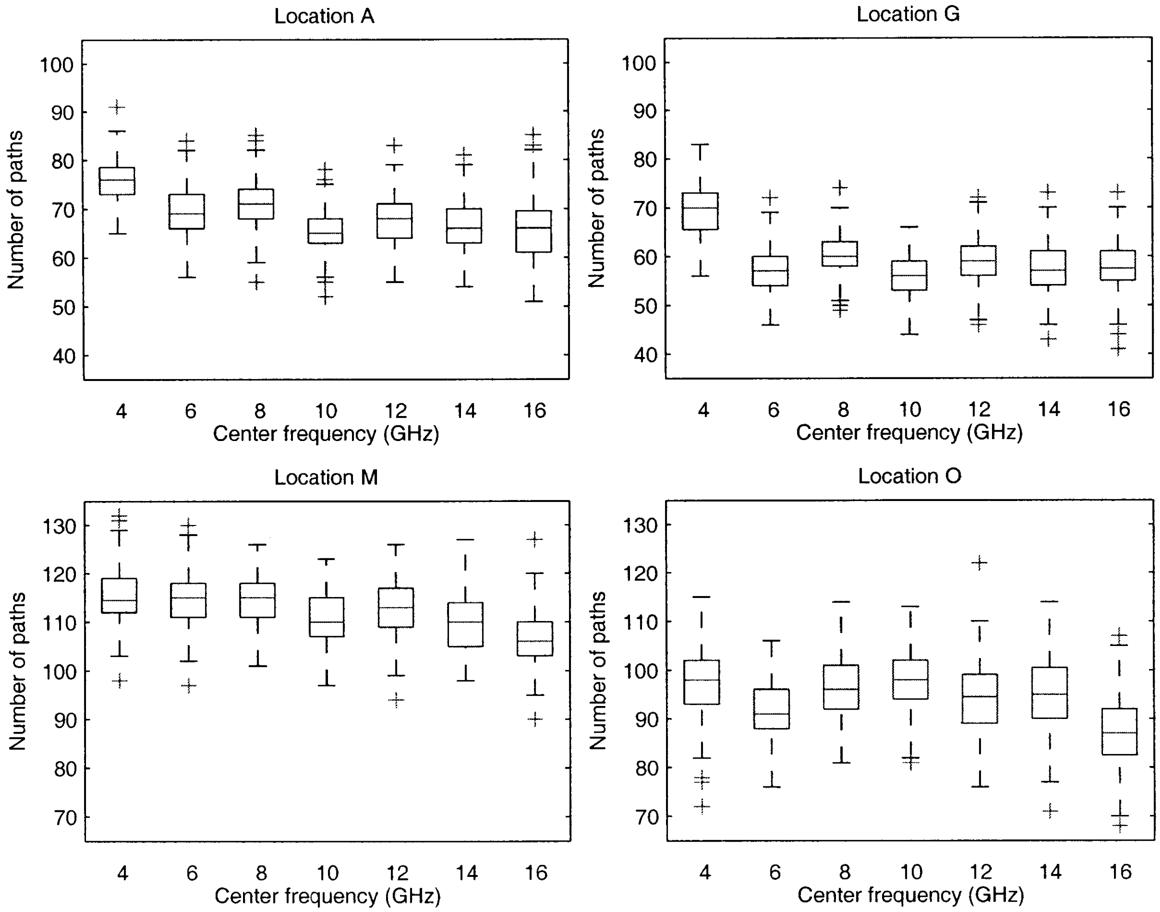

Figure 4-5: Number of paths output by the search-subtract-readjust algorithm for four representative locations in the measurement environment at a fixed bandwidth of 1 GHz. There are only minor variations in the number of paths as a function of center frequency.

4.4.2 Number of Multipath Components

An important aspect of wideband diversity systems is the number of multipath components present in the channel, as this has an impact on the available level of diversity. The WSSUS model with IID complex Gaussian fading assumes the use of approximately $T_\mathrm{d}/T_\mathrm{c}$ taps. Since T_c is approximately equal to the inverse of the spreading bandwidth, this model implies that the diversity available in the channel scales linearly with bandwidth.

Using the large number of channel realizations captured with the measurement apparatus described in Ch. 2, it is possible to analyse the number of multipath components present in realistic propagation channels. Figs. 4-5–4-7 depict box and whisker plots of the value N_d resulting from the channel parameter extraction algorithm, Sec. 3.4.3, which serves as

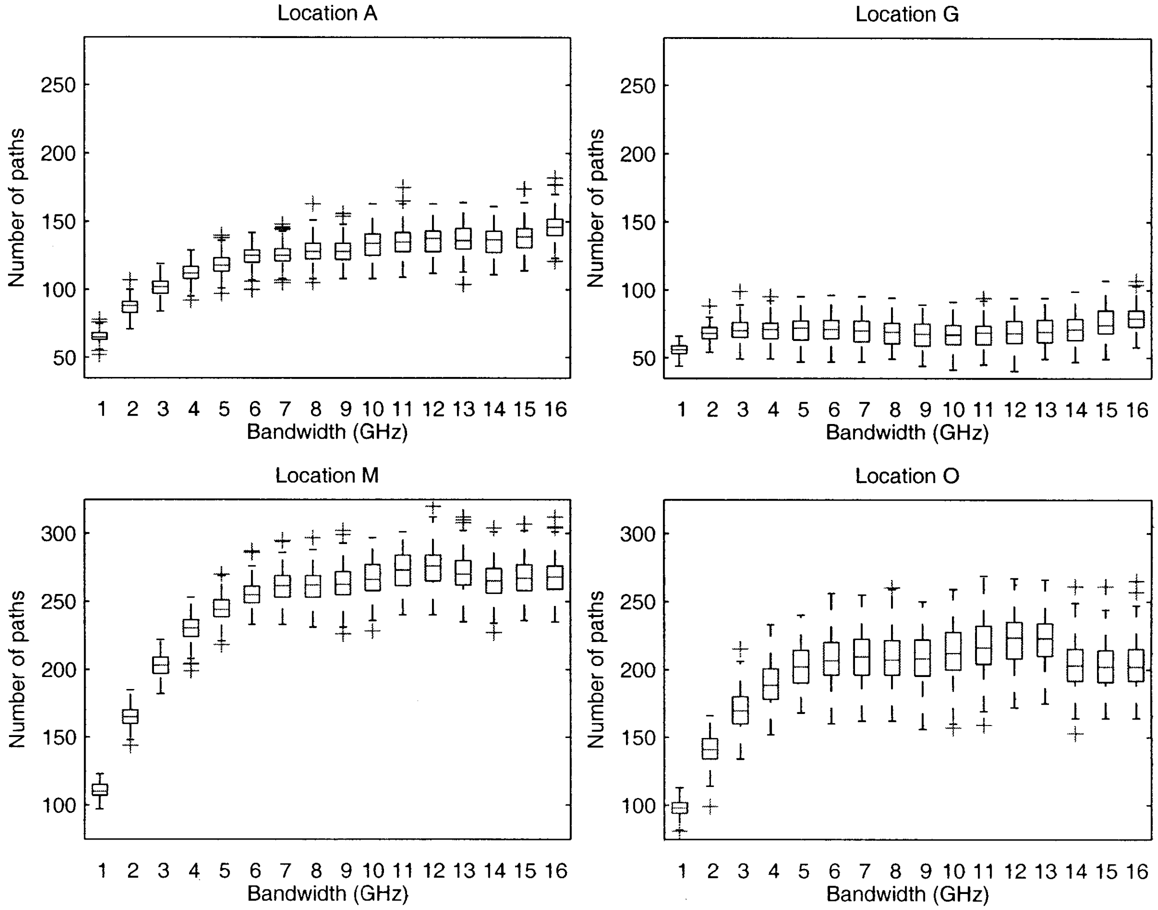

Figure 4-6: Number of paths output by the search-subtract-readjust algorithm for four representative locations in the measurement environment at a fixed center frequency 10 GHz. The curves display a saturation phenomena as bandwidth is increased, and the effect is more pronounced in dispersive environments.

a measure of the number of multipath components in a particular channel realization.[5] Fig. 4-5 considers the values of N_{d} for measurements from the four representative locations for a fixed bandwidth of $W = 1\,\mathrm{GHz}$. Mathematically, the upper-left corner of Fig. 4-5 considers the set $\left\{ {N_{\mathrm{d}}}^{(k)} \,\middle|\, h^{(k)} \in \mathcal{H}_0^{\mathrm{A}} \circledast \mathcal{S}_{\mathrm{s}}\{W = 1\} \right\}$, where $\mathcal{S}_{\mathrm{s}}\{W = x\}$ denotes a subset of center frequency–bandwidth pairs with fixed bandwidth equal to x:

$$\mathcal{S}_{\mathrm{s}}\{W = x\} = \left\{ (f_{\mathrm{c}}, W) \,\middle|\, (f_{\mathrm{c}}, W) \in \mathcal{S}_{\mathrm{s}},\, W = x \right\} .$$

---

[5] The horizontal red line in a box and whisker plot indicates the median value, while the bottom and the top of the box indicate the first and third quartiles. The lines above and below the box, known as whiskers, extend to the most extreme data point within 1.5 times the inter-quartile distance (the distance between the first and third quartiles). Any data points lying beyond the whiskers are considered outliers and are shown as red pluses [53].

The quantity $h^{(k)}$ denotes the kth channel realization and $\mathcal{H}_0^{\mathrm{A}}$ is the set of channel realizations collected at location G. Similar sets can be defined for the other locations: G, M, and O. As shown in the figure, there is little variation in the number of resolved multipath components as a function of center frequency for the four representative locations. The ability to resolve the multipath components present in a wideband channel is related to the support of the transmitted pulse (in the time domain). Transmitted pulses with larger time-domain support will average or smear closely spaced multipath components, reducing the apparent number of multipath components. Since the time-domain support is not related to the center frequency of the transmitted pulse, significant variations in the number of multipath components as a function of center frequency are not expected to occur.

In contrast, Fig. 4-6 indicates that in some cases there are significant variations in the number of resolved multipath components as a function of bandwidth. Fig. 4-6 considers the values of N_{d} for measurements from the four representative locations for a fixed center frequency of $f_{\mathrm{c}} = 10\,\mathrm{GHz}$. Mathematically, the upper-left corner considers the set $\left\{ {N_{\mathrm{d}}}^{(k)} \,\middle|\, h^{(k)} \in \mathcal{H}_0^{\mathrm{A}} \circledast \mathcal{S}_{\mathrm{s}}\{f_{\mathrm{c}} = 10\} \right\}$, where $\mathcal{S}_{\mathrm{s}}\{f_{\mathrm{c}} = x\}$ denotes a subset of center frequency–bandwidth pairs with fixed center frequency equal to x:

$$\mathcal{S}_{\mathrm{s}}\{f_{\mathrm{c}} = x\} = \left\{ (f_{\mathrm{c}}, W) \,\middle|\, (f_{\mathrm{c}}, W) \in \mathcal{S}_{\mathrm{s}},\, f_{\mathrm{c}} = x \right\} .$$

Here, it can be seen that the number of multipath components tends to increase with bandwidth but becomes saturated at some point. Bandwidths beyond this point do not yield significantly more paths. Furthermore, the effect is more prominent in NLOS environments. In particular, in the NLOS case increases from around 100 multipath components at 1 GHz to over 200 paths at 16 GHz can be seen for both locations M and O. In location G the effect is much more subtle as the increase is from slightly more than 50 paths to only 80 paths. This can be attributed to the fact that location G is very close to the transmitter, and hence has paths that contain a high percentage of the total energy present in the channel response. On the other hand, in more dispersive environments (i.e. the NLOS case) there are many paths with small amounts of energy. The figure also shows that there is more dispersion, indicated by the size of the boxes and length of the whiskers, in the distribution of the number of paths for a fixed bandwidth in the NLOS case.

Finally, Fig. 4-7 shows five box and whisker plots for the sets of channel realizations

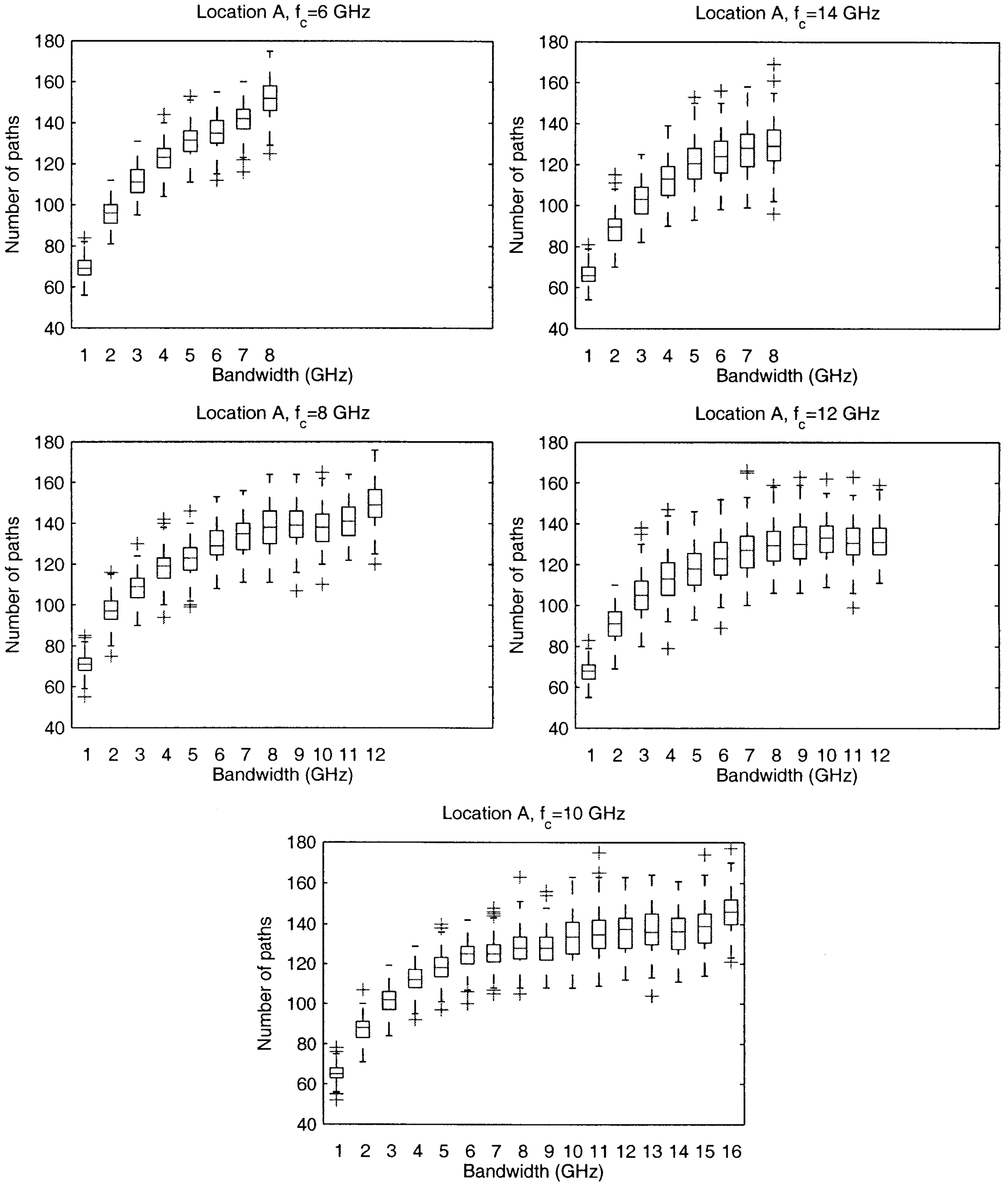

Figure 4-7: Number of paths output by the search-subtract-readjust algorithm for location A as a function of bandwidth for five different center frequencies. The curves display a similar saturation phenomena as bandwidth is increased, regardless of center-frequency.

$\mathcal{H}_0^{\mathrm{A}} \circledast \mathcal{S}_{\mathrm{s}}\{f_{\mathrm{c}} = 6\}$, $\mathcal{H}_0^{\mathrm{A}} \circledast \mathcal{S}_{\mathrm{s}}\{f_{\mathrm{c}} = 8\}$, $\mathcal{H}_0^{\mathrm{A}} \circledast \mathcal{S}_{\mathrm{s}}\{f_{\mathrm{c}} = 10\}$, $\mathcal{H}_0^{\mathrm{A}} \circledast \mathcal{S}_{\mathrm{s}}\{f_{\mathrm{c}} = 12\}$, and $\mathcal{H}_0^{\mathrm{A}} \circledast \mathcal{S}_{\mathrm{s}}\{f_{\mathrm{c}} = 14\}$.[6] These plots further confirm that as bandwidth increases the number of multipath

---

[6] Note that for some center frequencies, all values of bandwidth are not available. This is a consequence

components increases, irrespective of the center frequency.

4.4.3 SEP Performance in Realistic Channels

Now we consider the SEP in the four representative measurement locations. For each location we consider the transmission of QPSK with NSNC and $L_\mathrm{d} = 4$, 8, 16, and 32 paths. The SEP is evaluated using the results of applying the algorithm described in Sec. 3.4.3 to extract the true channel parameters from a set of measurements. The estimated channel gain vectors are then constructed by adding complex Gaussian estimation error to the gains resulting from the extraction procedure. This allows for the evaluation of the performance for different levels of estimation accuracy according to the model described in Sec. 4.1.3.

We plot the SEP as a function of total received SNR, that is $\Gamma_\mathrm{tot} = E_\mathrm{s}/N_0\mathbb{E}\left\{\|\boldsymbol{h}\|^2\right\}$. For each location we consider the measurements from the main grid observed at a center frequency of 10 GHz, $\mathcal{H}_0 \circledast \mathcal{S}_\mathrm{s}\{f_\mathrm{c} = 10\}$. For each center frequency–bandwidth pair, the set of channel responses is normalized to have average unit energy, i.e.

$$\frac{1}{|\mathcal{H}_0 \otimes \{(f_\mathrm{c}, W)\}|} \sum_{\boldsymbol{h}^{(k)} \in \mathcal{H}_0 \otimes \{(f_\mathrm{c}, W)\}} \|\boldsymbol{h}^{(k)}\|^2 = 1\,,$$

where $|\mathcal{H}_0 \otimes \{(f_\mathrm{c}, W)\}| = 188$. The values of $\mathbb{V}\left\{\hat{h}_k\right\}$ and $\mathbb{E}\left\{\hat{h}_k\right\}$ used when computing α in (4.35) are based on the 188 realizations of $\hat{\boldsymbol{h}} = \boldsymbol{h} + \boldsymbol{e}$, where each realization of $\boldsymbol{h}$ is corrupted by a different error vector $\boldsymbol{e}$ according to the model in Sec. 4.1.3.

Fig. 4-8 shows the mean path energy capture as a function of L_d for the four representative locations at 1 GHz and 18 GHz. Path energy capture for a particular channel realization $\boldsymbol{h}$, is defined as

$$E_\mathrm{C}^\mathrm{path}(L_\mathrm{d}) \triangleq \frac{1}{\|\boldsymbol{h}\|^2} \sum_{l=1}^{L_\mathrm{d}} \left|h_{[l]}\right|^2\,, \tag{4.50}$$

where $h_{[l]}$ is the channel gain with the lth largest magnitude. The mean path energy capture is computed by taking the mean of the path energy capture over the set of considered channel realizations. The path energy capture can be viewed as the percentage of energy captured by an L_d path ISIC receiver, and can give insights into the behavior of the SEP. The figure indicates that the LOS locations G and A have a much sharper rise in path energy

---

of the measurement setup and the set of possible center frequency–bandwidth pairs.

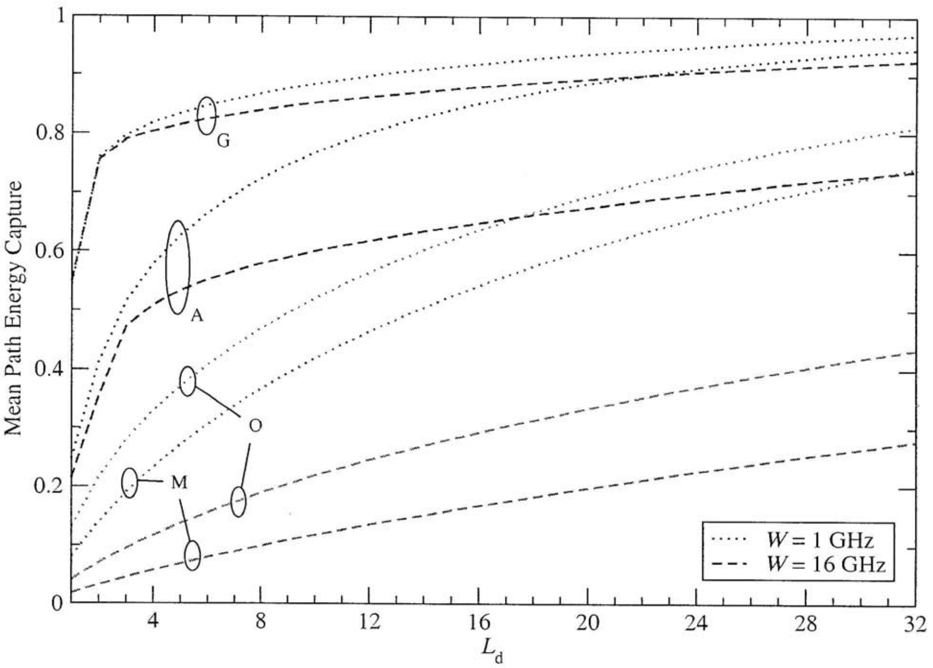

Figure 4-8: Path energy capture for measurement locations A, G, M, and O.

capture for low values of L_d. On the other hand the NLOS locations M and O show a much smoother and even increase in path energy capture as L_d increases. The figure also gives evidence that there is a more significant difference in path energy capture for different bandwidths in the NLOS case. For example, at $L_\mathrm{d} = 8$ there is less than a 10% difference between 1 GHz and 18 GHz at location G, while for location O this difference is almost 30%.

Figs. 4-9–4-12 show the SEP of NSNC for locations A, G, M, and O. In particular, $L_\mathrm{d} = 4$, 16, and 32 are considered at a bandwidth of $W = 1\,\mathrm{GHz}$ with $N_\mathrm{p}\,\varepsilon = 2$ and 16. As expected, the SEP curves for $N_\mathrm{p}\,\varepsilon = 16$ fall below the corresponding curves for $N_\mathrm{p}\,\varepsilon = 2$. That is, as the energy devoted to channel estimation increases, the SEP performance improves. The SEP results also indicate that, in general, as L_d increases the SEP decreases. From the plots one can also clearly see the effect of the dispersive nature of the NLOS propagation channels (locations M and O). Recall that in these channels the path energy capture increases more gradually than in the LOS case. This indicates that additional paths contribute a significant amount of energy to the total received SNR. Thus, the SEP curves are spread more evenly as L_d increases. On the other hand, for the LOS case (locations A and G) the SEP curves are significantly closer. This can be attributed to the fact that, as indicated by the path energy capture, the paths beyond $L_\mathrm{d} = 4$ only contribute small amounts of additional energy. The physical interpretation for this phenomenon is as follows:

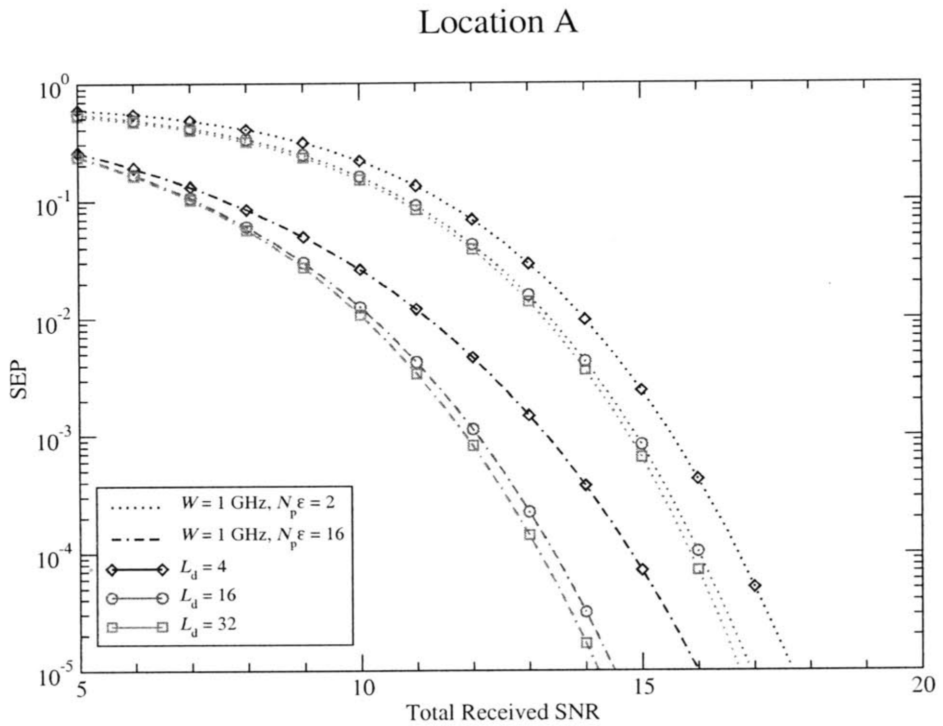

Figure 4-9: SEP at location A for 1 GHz bandwidth, $N_\mathrm{p}\,\varepsilon = 2$, 16 and $L_\mathrm{d} = 4$, 16, 32.

in LOS environments, although there may be many paths (see, for example, location A in Fig. 4-6), there are only a few dominant paths. When an SSD receiver combines these few dominant paths, the majority of the energy is captured.

Fig. 4-13 depicts the SEP performance of the four representative locations with $N_\mathrm{p}\,\varepsilon = 2$ and bandwidths 1 and 16 GHz. The results indicate that NSNC at $W = 1$ GHz outperforms NSNC at $W = 16$ GHz. To understand this further, Fig. 4-14 investigate the SEP performance at a fixed total received SNR of 15 dB as a function of bandwidth, for $L_\mathrm{d} = 2$, 4, 8, 16, and 32 paths and $N_\mathrm{p}\,\varepsilon = 2$ and 16. From the figure, it can be seen that in the majority of cases $W = 1$ GHz, provides the lowest SEP. As indicated by Fig. 4-8, at lower bandwidths the initial combined paths contain a higher percentage of the total energy, but the diversity available in the channel is decreased (see Fig. 4-6). One might expect a trade-off to exist between the bandwidth (i.e., level of diversity) and the energy collected by the number of combined paths, leading to an optimal bandwidth. However, in this case for the SNRs of interest, the results imply that the energy collected plays a more important role.

For the case of location G, however, the optimal bandwidth is approximately 10 GHz for $N_\mathrm{p}\,\varepsilon = 2$ and $L_\mathrm{d} = 2$, 4, and 8. There is also another interesting phenomenon which occurs at location G. Unlike the other locations, where increases in L_d generally decrease

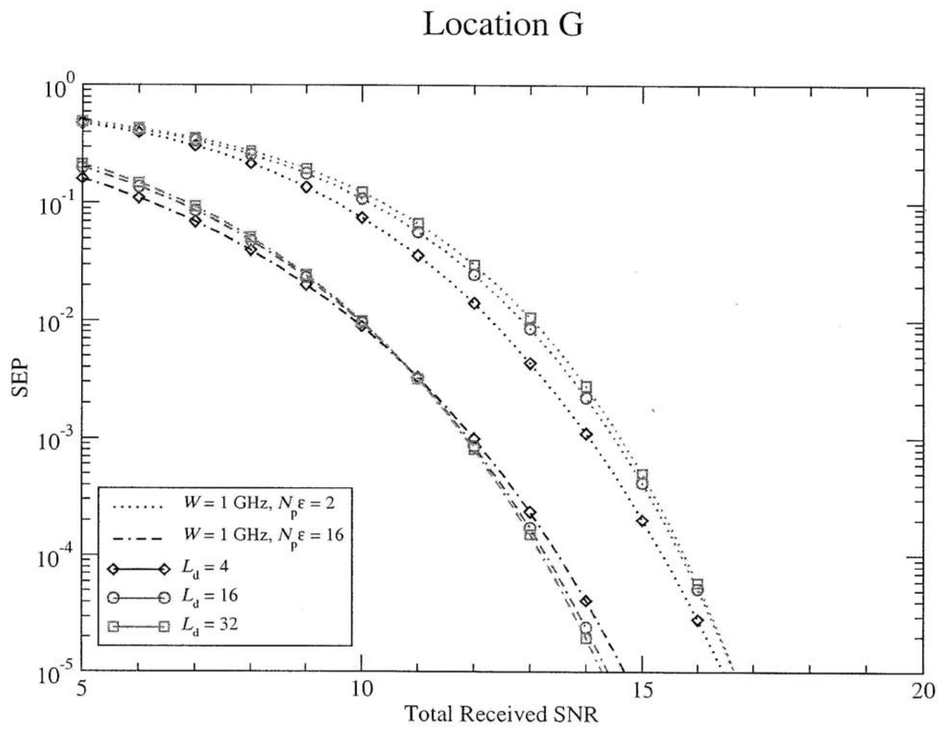

Figure 4-10: SEP at location G for 1 GHz bandwidth, $N_\mathrm{p}\,\varepsilon = 2$, 16 and $L_\mathrm{d} = 4$, 16, 32.

the SEP, in the upper portion of the plot for location G (corresponding to the $N_\mathrm{p}\,\varepsilon = 2$ case) it can be seen that increasing L_d increases the SEP. This can be explained as follows: from the path energy capture curve (Fig. 4-8) it can be seen that the paths beyond $L_\mathrm{d} = 2$ contain small amounts of energy. Inclusion of these paths in an NSNC receiver increases the SEP because the path gains can not be reliably estimated for paths with such small energy. When $N_\mathrm{p}\,\varepsilon = 16$ (depicted in the lower portion of the plot for location G) the paths can be estimated more reliably, and we see that increasing L_d decreases the SEP.

4.5 Conclusion

This chapter developed a complete framework for evaluating the SEP for ideal and non-ideal RSSD systems operating in a variety of multipath channels. In particular, we considered the case of a WSSUS channel model, where the magnitude of the channel gains are Rayleigh distributed, as well as the case where only a set of measured channel realizations, from an unknown distribution, are available. The non-ideal system that was studied was one in which the channel gains were estimated using the transmission of pilot symbols. The SEP expressions developed for the case where only a set of channel realizations are available

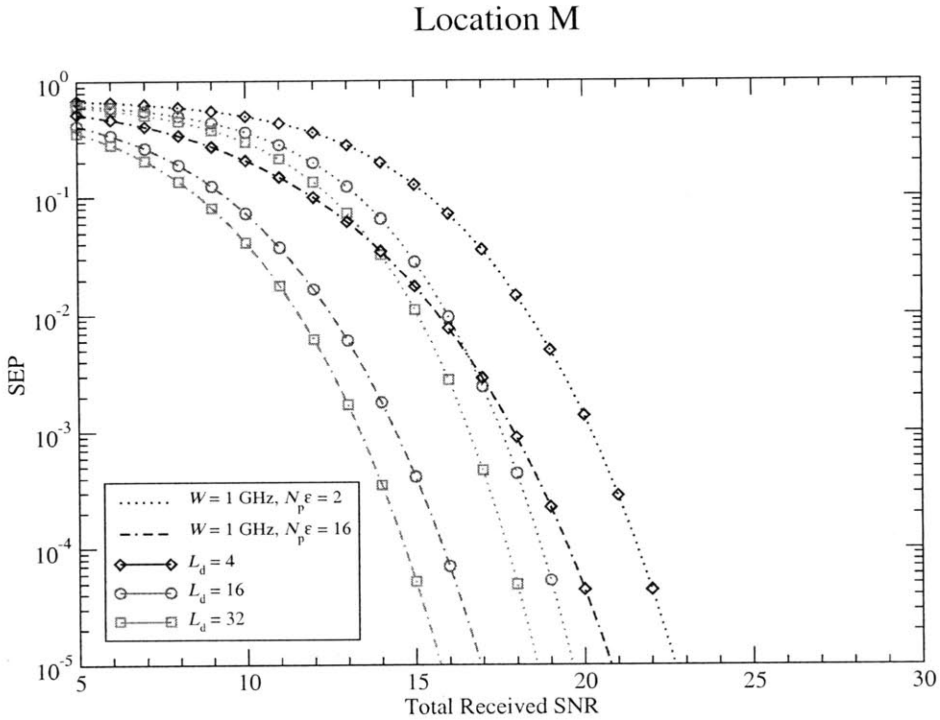

Figure 4-11: SEP at location M for 1 GHz bandwidth, $N_\mathrm{p}\,\varepsilon = 2$, 16 and $L_\mathrm{d} = 4$, 16, 32.

are semi-analytical in nature. That is, they make use of Monte-Carlo averaging of exact conditional expressions. Comparisons between exact results for the Rayleigh fading case and the semi-analytical expressions showed excellent agreement.

Using the developed framework, this chapter investigated the SEP performance based on measurements from four representative locations in the measurement environment. The numerical results showed that as bandwidth is increased the channel responses contain more multipath components. Results also indicated that there are significant differences in the mean path energy capture under different propagation conditions. These differences can give insights into the SEP performance. In particular, in LOS conditions the SEP curves were much closer for different L_d, while in NLOS conditions the SEP curves were much more spread. Finally, the numerical results indicated that, based on the measurement data considered, 1 GHz bandwidth provides the best performance.

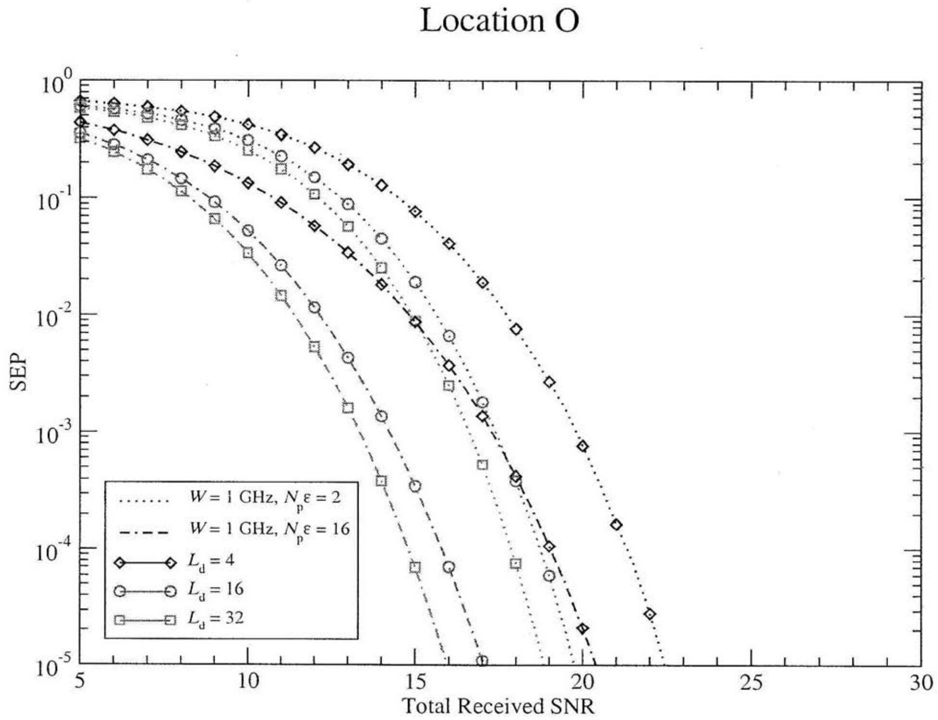
Location O

Figure 4-12: SEP at location O for 1 GHz bandwidth, $N_{\mathrm{p}}\,\varepsilon = 2$, 16 and $L_{\mathrm{d}} = 4$, 16, 32.

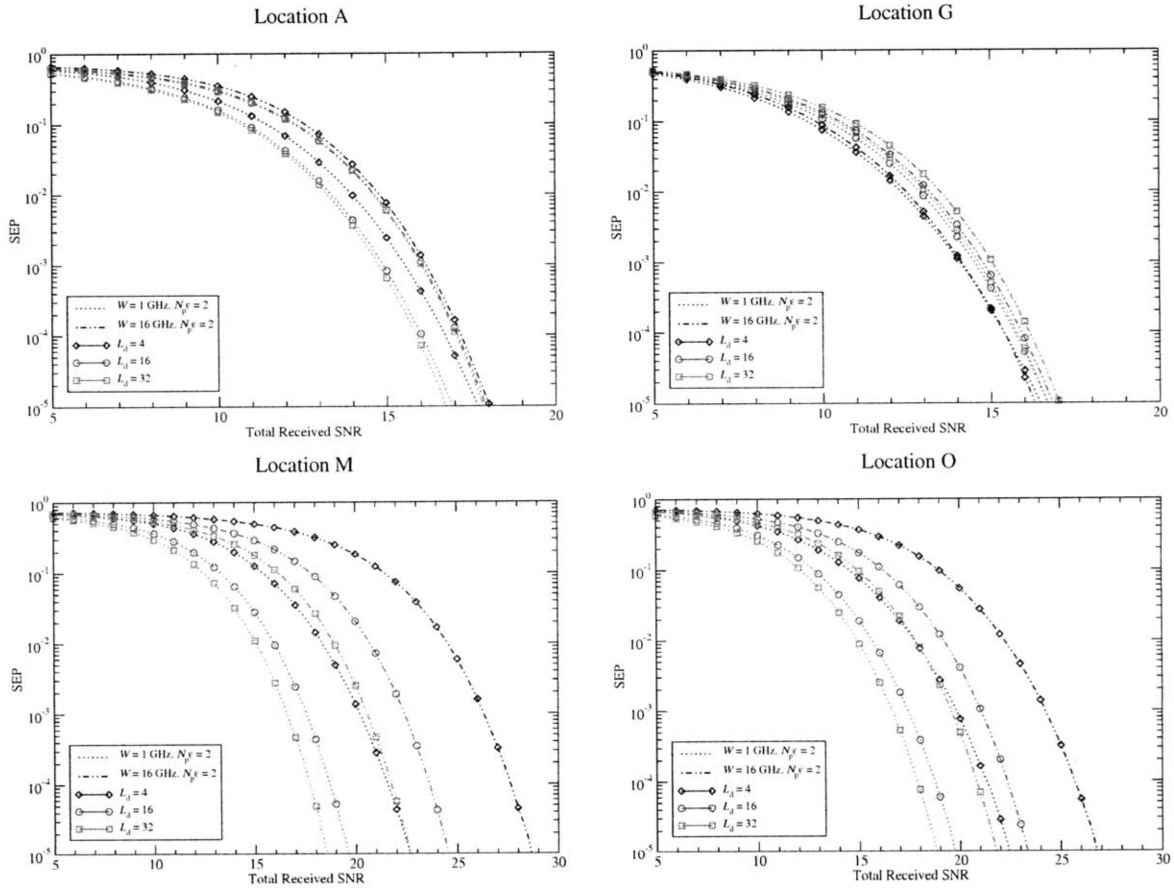

Figure 4-13: SEP at locations A, G, M, and O. Curves are shown for $N_\text{p}\,\varepsilon = 2$ at 1 GHz and 16 GHz bandwidths with $L_\text{d} = 2$, 4, 16, 32.

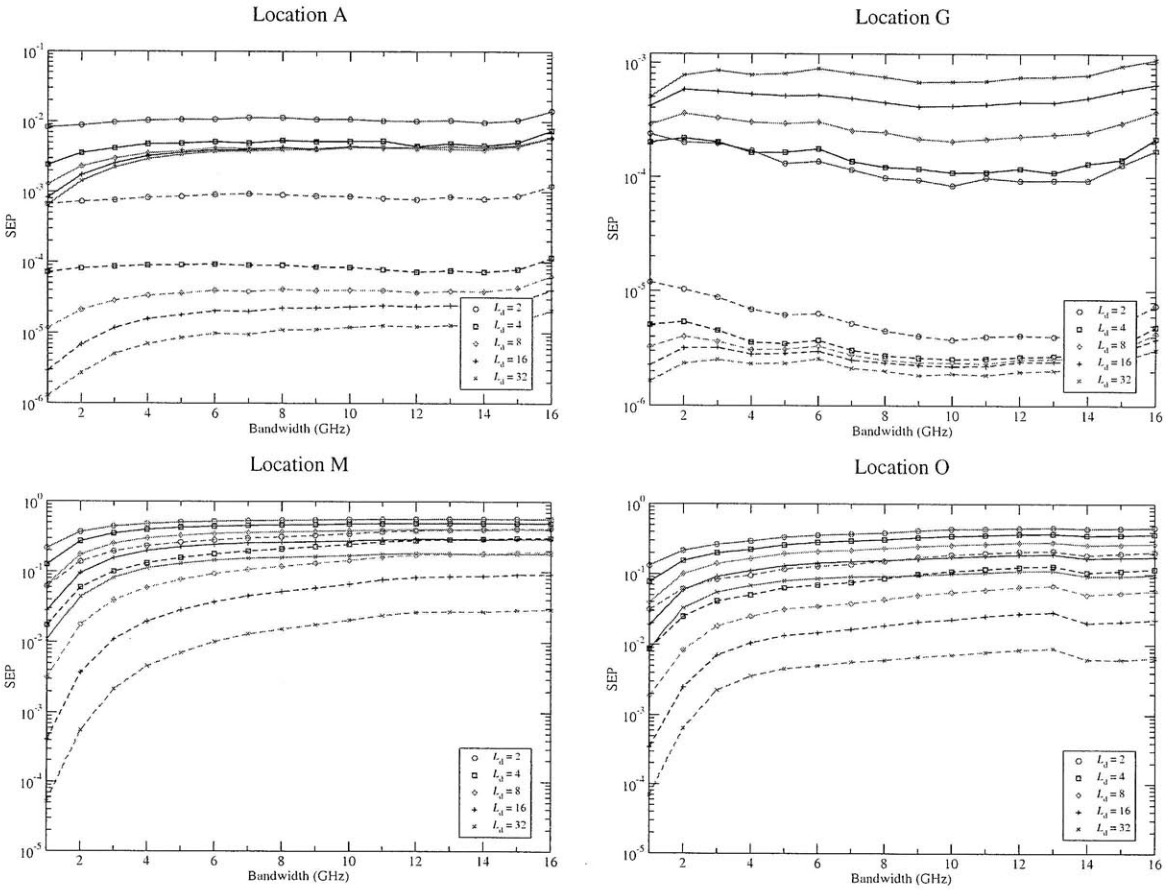

Figure 4-14: SEP as a function of bandwidth at $\Gamma_{\text{tot}} = 15\,\text{dB}$ at locations A, G, M, and O. Curves are shown for $N_{\text{p}}\,\varepsilon = 2$ (solid lines) and $N_{\text{p}}\,\varepsilon = 16$ (dashed lines) with $L_{\text{d}} = 2, 4, 8, 16, 32$.

Chapter 5

Improved Lower Bounds on Time-of-Arrival Estimation Error

Location-awareness is quickly becoming important in many commercial, public safety, and military applications. One key example is the integration of Global Positioning System (GPS) into cellular phones and mobile devices, which, in conjunction with WiFi localization, has ignited a new era of ubiquitous location awareness [54]. The coming years will see the emergence of applications which require localization systems to operate with sub-meter accuracy in harsh, cluttered propagation environments where GPS typically fails.

Among the different localization techniques, those based on distance estimation (ranging) are most suitable for high localization accuracy when constraints require the use of low complexity devices. We refer the reader to [55–59] for more information on the variety of localization techniques. One fundamental approach to distance estimation is through the use of several signal TOA measurements. In general the ranging accuracy of TOA measurements increases with signal bandwidth and hence the use of wideband or UWB signals is attractive for ranging applications. In particular, UWB technology offers the potential of achieving high ranging accuracy even in cluttered environments [36, 56, 60–67], due to its ability to resolve closely-spaced multipath components and penetrate obstacles [3–6,17,68,69]. These TOA estimation techniques operate by estimating the time at which the first signal path arrives, and are primarily affected by noise, multipath propagation, obstruction of the direct path, interference, and clock drift [56,60,65]. In realistic propagation environments the first multipath component is frequently not the strongest, making TOA estimation even more challenging [70–72].

Several papers address TOA estimation in the presence of multipath (e.g., [36, 70, 73]). The problem of TOA estimation in multipath environments is closely related to channel estimation, where amplitudes and delays of the multipath components are jointly estimated using, for example, a ML approach [5, 74] or a generalized ML technique [37]. While the performance of a specific TOA estimation algorithm can be evaluated, estimation error bounds play a fundamental role since they can serve as useful performance benchmarks for the design of TOA estimators.

The CRB has been widely used as a performance benchmark for assessing estimation error. Its use is justified by asserting that the performance of the ML estimator approaches the CRB asymptotically for sufficiently long observation times or for high SNRs [75]. It is well known, however, that the CRB is not accurate at low and moderate SNR. In fact, the performance of the TOA estimator, like all non-linear estimators, is characterized by the presence of distinct SNR regions (i.e., low, medium, and high SNRs) corresponding to different modes of operation. This behavior is referred to as the *threshold effect* and it has been studied in a variety of contexts (e.g., [76–81]). In the low SNR region (also known as the *a priori region*), the MSE is close to that obtained solely from the a priori information about the TOA and signal observations provide little additional information. In the high SNR region (also known as the *asymptotic region*), the MSE is accurately predicted by the CRB. Between these two extremes, there may be an additional region (also known as the *transition region* or *ambiguity region*) where observations are subject to ambiguities that are not accounted for by the CRB [75].

Although the CRB accurately predicts the MSE in the asymptotic region, operating in such a region is often impractical due to constraints on observation times or power levels. Therefore other bounds, which are more complicated but tighter than the CRB, have been proposed in the literature. In particular, the Barankin bound identifies the SNR values (thresholds) that distinguish the ambiguity region [82,83]. The Ziv-Zakai bound (ZZB) [84], with its improved versions such as the Bellini-Tartara bound [85] and the Chazan-Zakai-Ziv bound [86], as well as the Weiss-Weinstein bound (WWB) [79] are more accurate than the Barakin bound. They can be applied to a wider range of SNRs and account for both ambiguity effects and a priori information of the parameter to be estimated. However, in many cases they may not be analytically tractable or require more complicated evaluations compared to the CRB, especially when operating in the presence of multipath [87–90].

In [91] the expression for the CRB for multipath environments is given starting from the joint estimation of channel parameters. In [90] the approach developed in [76, 77] for the estimation of the relative delay between two sensors emitting noise-like signals is extended to that emitting UWB signals. The work [92] evaluates the ZZB for Gaussian signals assuming perfect channel knowledge at the receiver. A few results are presented for the case where the receiver has partial or no knowledge about the channel [88, 89]. In particular, in [88] the Ziv-Zakai Bellini-Tartara (ZZBT) bound is investigated using measured data as well as Monte Carlo generated channel pulse responses (CPRs). In [89] the ZZB is derived using a second order statistics approach by modeling the received signal as a non-stationary Gaussian random process.

The aim of this chapter is to investigate theoretical bounds on the MSE of TOA estimation in wideband and UWB ranging systems operating in realistic multipath environments. To allow for a comprehensive overview of the problems, some previous results are also reviewed and briefly discussed when necessary. The main contributions of this chapter are as follows:

- Derivation of analytical expressions for the CRB and ZZB for TOA estimation for wideband and UWB ranging systems operating in realistic multipath environments under different a priori knowledge of the multipath phenomena;
- Extension of the bounds to the case where a finite set of channel realizations (e.g., from channel responses measured in realistic environments) is available;
- Demonstration that the ZZB, unlike the classical CRB, properly accounts for the effect of multipath and provides improved bounds for a wider range of SNRs; and
- Investigation of the impact of multipath channel characteristics, as well as a priori knowledge about the multipath phenomena for measured wideband channels at various bandwidths.

The remainder of this chapter is organized as follows. In Sec. 5.1 the signal and channel models are introduced. The ZZB is reviewed briefly in Sec. 5.2 and compared to the CRB in the ideal AWGN scenario in Sec. 5.3. The CRB and ZZB are derived for realistic multipath environments under different operating conditions in Secs. 5.4 and 5.5. Numerical results based on the multipath channel model we consider, as well as for data collected in realistic environments are presented in Sec. 5.6. Finally, conclusions are given in Sec. 5.7.

5.1 Signal and Channel Models

We will consider the transmission of a single band-limited pulse $p(t)$ with bandwidth W and energy E_p.[1] In practice, $p(t)$ is generated starting from a baseband pulse $g(t)$ that is modulated to a center frequency f_c:

$$p(t) = \sqrt{2\,E_\mathrm{p}}\,\Re\Big\{g(t)e^{\jmath 2\pi f_\mathrm{c} t}\Big\} \tag{5.1}$$

where $g(t)$ has unit energy. Let us define

$$\rho_p(z) = \frac{1}{E_\mathrm{p}}\int_{-\infty}^{\infty} p(t)\,p^*(t-z)\,dt \tag{5.2}$$

as the normalized autocorrelation function of $p(t)$.[2] The normalized autocorrelation function of $g(t)$, $\rho_g(z)$, can be defined in a similar way. We will consider the case when $g(t)$ is a real signal, as is usual in impulse radio systems, and therefore we can write

$$p(t) = \sqrt{2\,E_\mathrm{p}}\,g(t)\,\cos\left(2\pi f_\mathrm{c} t\right). \tag{5.3}$$

When $p(t)$ is transmitted through a multipath channel, the received signal can be represented as

$$r(t) = s(t-\tau) + n(t)\,, \tag{5.4}$$

where $s(t)$ is the CPR, τ is the TOA of the received signal to be estimated, and $n(t)$ is zero-mean AWGN with two-sided spectral density $N_0/2$.

The goal is to obtain an estimate $\hat{\tau}$ of τ by observing $r(t)$ in the interval $[0, T_\mathrm{ob})$ in the presence of signal distortion due to multipath. In the absence of other information, we assume τ to be unknown and randomly distributed in the interval $[0, T_\mathrm{a})$, with $T_\mathrm{a}+T_\mathrm{d} < T_\mathrm{ob}$, where T_d is the dispersion of the channel, so that all the multipath components fall within the observation interval T_ob.

Several techniques can be adopted to solve this problem (see for example [60] and the references therein). In this paper the CRB and improved bounds based on the ZZB for TOA estimation are derived and discussed under different a priori knowledge of the multipath

---

[1] In general $p(t)$ can represent a multiple access signal such as direct sequence or time-hopping (TH) [1,2].

[2] Since a band-limited signal cannot also be time-limited, we assume it can be truncated in time to a duration T_p with some small approximation error.

phenomena. These bounds are applied to the case where $s(t)$ is a sample of a random process with an uncountably infinite ensemble of realizations and, in some specific cases, when the random process has a finite ensemble of realizations.

5.1.1 Infinite Ensemble of Channel Realizations

In the infinite ensemble case, $s(t)$ belongs to a random process with an uncountably infinite number of CPR realizations. Typically the random process is modeled as a function of a finite set of continuous random parameters. We will consider a multipath channel given by

$$h(t) = \sum_i \alpha_i \delta(t - \tau_i) \tag{5.5}$$

where α_i is the real gain of the ith multipath component. After the transmission of a bandpass pulse, $p(t)$, the response is given by

$$\begin{aligned} s(t) &= \sqrt{2E_{\mathrm{p}}}\Re\left\{\left[\sum_i \alpha_i e^{-\jmath 2\pi f_{\mathrm{c}}\tau_i} g(t-\tau_i)\right] e^{\jmath 2\pi f_{\mathrm{c}} t}\right\} & (5.6)\\ &= \underbrace{\sqrt{2E_{\mathrm{p}}}\sum_i \alpha_i \cos(2\pi f_{\mathrm{c}}\tau_i) g(t-\tau_i)}_{I(t)} \cos(2\pi f_{\mathrm{c}} t) - \underbrace{\sqrt{2E_{\mathrm{p}}}\sum_i \alpha_i \sin(2\pi f_{\mathrm{c}}\tau_i) g(t-\tau_i)}_{Q(t)} \sin(2\pi f_{\mathrm{c}} t) & (5.7)\end{aligned}$$

Noting that the bandlimited pulse $g(t)$ can be represented as

$$g(t) = \sum_l g\left(\frac{l}{W}\right) \operatorname{sinc}\left(W\left(t - \frac{l}{W}\right)\right), \tag{5.8}$$

we can express $I(t)$ and $Q(t)$ as

$$I(t) = \sum_l g\left(t - \frac{l}{W}\right) h_{\mathrm{I}}\left(\frac{l}{W}\right) \tag{5.9}$$

$$Q(t) = \sum_l g\left(t - \frac{l}{W}\right) h_{\mathrm{Q}}\left(\frac{l}{W}\right). \tag{5.10}$$

Here, $h_{\mathrm{I}}(\cdot)$ and $h_{\mathrm{Q}}(\cdot)$ are in the in-phase and quadrature components, respectively, of the baseband channel observed with a bandwidth of $W/2$, and are given by

$$h_{\mathrm{I}}(t) = \sum_i \alpha_i \cos(2\pi f_c \tau_i) \mathrm{sinc}\left(W\left(t-\tau_i\right)\right) \tag{5.11}$$

$$h_{\mathrm{Q}}(t) = \sum_i \alpha_i \sin(2\pi f_c \tau_i) \mathrm{sinc}\left(W\left(t-\tau_i\right)\right) \,. \tag{5.12}$$

In a dense multipath scenario, (5.11) and (5.12) indicate that the samples of $h_{\mathrm{I}}(\cdot)$ and $h_{\mathrm{Q}}(\cdot)$ contain contributions from many paths. Under an uncorrelated scattering assumption, each of the samples will consist of many independent contributions. Hence, we model the samples of $h_{\mathrm{I}}(\cdot)$ and $h_{\mathrm{Q}}(\cdot)$ as independent Gaussian random variables.[3] Setting $\mathsf{v}_l = h_{\mathrm{I}}\left(\frac{l}{W}\right)$ and $\mathsf{v}_{L+l} = h_{\mathrm{Q}}\left(\frac{l}{W}\right)$, gives

$$s(t) = \sqrt{2E_{\mathrm{p}}} \sum_{l=1}^{L} \left[\mathsf{v}_l \cos(2\pi f_c t) - \mathsf{v}_{L+l} \sin(2\pi f_c t)\right] g\left(t-(l-1)\Delta\tau\right) \,, \tag{5.13}$$

where L is chosen to capture the multipath spread of the channel and $\Delta\tau \triangleq 1/W$. We denote the average power gain of the lth path as $\Gamma_l = \mathbb{E}\left\{\mathsf{v}_l^2\right\} + \mathbb{E}\left\{\mathsf{v}_{L+l}^2\right\}$, where $\mathbb{E}\left\{\cdot\right\}$ is the statistical expectation operator. Without loss of generality we assume $\sum_{l=1}^{L}\Gamma_l = 1$, so that E_{p} represents the average received energy per transmitted pulse. For each set of channel parameters $\boldsymbol{v} = \{v_1, v_2, \ldots, v_{2L}\}$ we obtain a realization $s(t, \boldsymbol{v})$ of the random process. We denote the joint probability density function (PDF) of the vector $\mathbf{v}$ as $f_{\mathbf{v}}(\boldsymbol{v})$.

The considerations above lead to the widely used Rayleigh/Rice multipath channel model, where $f_{\mathbf{v}}(\boldsymbol{v})$ is a $2L$-dimensional joint Gaussian PDF. The v_l are independent RVs with

$$\mu_l = \mathbb{E}\left\{\mathsf{v}_l\right\} = \begin{cases} s_l & 1 \le l \le L, \\ 0 & L < l \le 2L \end{cases} \tag{5.14}$$

---

[3] Throughout we use the following notation: sanserif font is used to indicate RVs, normal math font is used to indicate a sample value of a RV, vectors are indicated with boldfaced lowercase letters, and matrices are indicated by boldfaced uppercase letters. For example: x indicates a scalar RV, while x indicates a sample value of that RV.

and

$$\mathbb{V}\{\mathsf{v}_l\} = \mathbb{V}\{\mathsf{v}_{L+l}\} = \sigma_l^2 , \quad 1 \le l \le L . \tag{5.15}$$

The parameters s_l and $2\sigma_l^2$ are the average amplitude of the specular component (when present) and the power gain of the scattered component of the lth path, respectively. Thus, the average power gain of the lth path is $\Gamma_l = \mu_l^2 + 2\sigma_l^2$. For notational convenience we will define the following vectors and matrices of the channel parameters: $\boldsymbol{\mu} = [\mu_1,\ \mu_2,\ \ldots,\ \mu_{2L}]$, $\boldsymbol{\Psi} = \operatorname{diag}\left\{[\sigma_1^2,\ \sigma_2^2,\ \ldots,\ \sigma_L^2]\right\}$, and $\boldsymbol{\Psi}_2 = \mathbf{I}_2 \otimes \boldsymbol{\Psi}$, where $\mathbf{I}_n$ is the $n \times n$ identity matrix and $\otimes$ is the Kronecker product.

5.1.2 Finite Ensemble of Channel Realizations

In the finite ensemble case, $s(t)$ belongs to a finite set of CPR realizations. We denote the ensemble of realizations as $\left\{s^{(k)}(t)\right\}_{k=1}^{N_{\mathrm{CPR}}}$, where $s^{(k)}(t)$ is the kth realization and N_{CPR} is the total number of CPR realizations. The CPRs are normalized to have an average channel gain of unity so that E_{p} represents the average received energy per transmitted pulse. The ensemble of CPRs can be obtained from a measurement campaign to asses the performance in a realistic environment. Care must be taken during the data collection process to ensure that a sufficient number of uncorrelated realizations are captured. Furthermore, the ensemble of realizations must be collected from an area where the multipath phenomena have similar statistical properties. Alternatively, $s^{(k)}(t)$ can be drawn independently according to a statistical model (e.g., the IEEE 802.15.4a channel model [93]) as part of a Monte Carlo approach when direct analytical evaluation of the bound becomes intractable. In general, the accuracy of these methods will improve as N_{CPR} increases.

5.2 The Ziv-Zakai Lower Bound

The Ziv-Zakai lower bound can be derived starting from the following general identity for MSE estimation[4]

$$\mathsf{MSE} = \mathbb{E}\left\{\epsilon^2\right\} = \frac{1}{2}\int_0^\infty z \cdot \mathbb{P}\left\{|\epsilon| \ge \frac{z}{2}\right\} dz , \tag{5.16}$$

---

[4] Here the expectation is with respect to τ and $r(t)$.

where $\epsilon \triangleq \hat{\tau} - \tau$ represents the estimation error. A lower bound on the MSE can then be obtained by lower-bounding the quantity $\mathbb{P}\left\{|\epsilon| \geq z/2\right\}$ [85]. It can be shown that

$$\mathbb{P}\left\{|\epsilon| \geq \frac{z}{2}\right\} = \int_{-\infty}^{\infty} \left[f_{\tau}(\zeta)\, \mathbb{P}\left\{\hat{\tau} \geq \zeta + \frac{z}{2} \middle| \tau = \zeta \right\} + f_{\tau}(\zeta + z)\, \mathbb{P}\left\{\hat{\tau} \leq \zeta + \frac{z}{2} \middle| \tau = \zeta + z \right\} \right] d\zeta \tag{5.17}$$

where $f_{\tau}(\cdot)$ is the PDF of the TOA τ. The previous expression can be lower-bounded by

$$2 \int_{-\infty}^{\infty} \min\left\{f_{\tau}(\zeta), f_{\tau}(\zeta + z)\right\} \left[\frac{1}{2}\mathbb{P}\left\{\hat{\tau} \geq \zeta + \frac{z}{2} \middle| \tau = \zeta \right\} + \frac{1}{2}\mathbb{P}\left\{\hat{\tau} \leq \zeta + \frac{z}{2} \middle| \tau = \zeta + z \right\} \right] d\zeta\,. \tag{5.18}$$

The term in square brackets in (5.18) represents the probability of error for deciding between two equally probable hypotheses

$$\begin{aligned} H_1 &: \ \tau = \zeta \\ H_2 &: \ \tau = \zeta + z \end{aligned} \tag{5.19}$$

according to a suboptimal rule. This rule requires that the parameter τ is first estimated and the decision between the two hypothesis is made based on a minimum distance criterion as described in [86]. Thus, (5.18) can be further lower-bounded by replacing the term in square brackets with the error probability $P_{\min}(\zeta, \zeta + z)$ corresponding to the optimum decision rule, that minimizes the error probability, based on the likelihood ratio test (LRT)

$$\frac{\Lambda\left[r(t)|\tau = \zeta\right]}{\Lambda\left[r(t)|\tau = \zeta + z\right]} \ \underset{H_2}{\overset{H_1}{\gtrless}} \ 1\,, \tag{5.20}$$

where $\Lambda\left[r(t)|\tau = \zeta\right]$ is the likelihood functional which quantifies the likelihood of receiving a waveform $r(t)$ given that the true value of the TOA τ is equal to ζ.

In general $P_{\min}(\zeta, \zeta + z)$ does not depend on the delay ζ, thus it can be written as $P_{\min}(z)$ and the bound can be formulated in terms of z [86]. When τ is uniformly distributed in $[0, T_{\mathrm{a}})$, the ZZB is given by [85, 86]

$$\mathsf{ZZB} = \frac{1}{T_{\mathrm{a}}} \int_{0}^{T_{\mathrm{a}}} z\left(T_{\mathrm{a}} - z\right) P_{\min}(z)\, dz\,. \tag{5.21}$$

The main challenge in evaluating (5.21) is to design the binary detection scheme based on the likelihood ratio in (5.20) and to derive a tractable expression for its performance

$P_{\min}(z)$. It is interesting to observe that the ZZB is obtained by recognizing that the performance evaluation of an estimation problem can be transformed to a binary detection problem. We will exploit this observation in subsequent sections to obtain the ZZB for multipath environments.

5.3 Theoretical Limits in Ideal Propagation Conditions

Before considering the general multipath case we analyze the theoretical performance limits of TOA estimation in AWGN channels in the absence of other error sources (i.e., $L = 1$, $\alpha_1 = 1$). This will provide insights into the influence of system parameters on fundamental ranging accuracy. In the absence of other error sources, the received signal is described by

$$r(t) = p(t-\tau) + n(t) \tag{5.22}$$

where τ is the TOA to be estimated based on the received signal $r(t)$. This is a classic nonlinear parameter estimation problem where the corresponding ML estimator, which is asymptotically efficient, is simply composed of a filter matched to the pulse $p(t)$ (or equivalently by a correlator with template $p(t)$) [75].

In ideal propagation conditions, the likelihood functional $\Lambda\left[r(t)|\tau\right]$ can be determined by first expanding the continuous waveforms in terms of a set of orthonormal basis functions as discussed in [75]:

$$\begin{aligned}\Lambda\left[r(t)|\tau\right] &= \lim_{K\to\infty} \frac{\prod_{i=1}^{K} \exp\left\{-\frac{(r_i-p_i)^2}{N_0}\right\}}{\prod_{i=1}^{K} \exp\left\{-\frac{r_i^2}{N_0}\right\}} \\ &= \lim_{K\to\infty} \exp\left\{-\frac{1}{N_0}\sum_{i=1}^{K} p_i^2 - 2p_i r_i\right\} \\ &= \exp\left\{-\frac{1}{N_0}\int_0^{T_{\text{ob}}} p^2(t-\tau) - 2p(t-\tau)r(t)\,dt\right\}\end{aligned} \tag{5.23}$$

where p_i and r_i are the coefficients resulting from the expansion of $p(t-\tau)$ and $r(t)$, respectively. The normalization in (5.23) ensures that the likelihood functional is well defined in the limit [75, 94].

5.3.1 The Cramér-Rao Bound in Ideal Conditions

It is well known that the MSE of any unbiased estimate $\hat{\tau}$ of τ is bounded by the CRB, that is,

$$\mathsf{MSE} = \mathbb{E}\left\{\epsilon^2\right\} \geq \mathsf{CRB}\,. \tag{5.24}$$

In the absence of multipath the CRB reduces to the classical expression [75][5]

$$\mathsf{CRB} = \left[-\mathbb{E}\left\{\frac{\partial^2}{\partial \tau^2} \ln \Lambda\left[r(t);\tau\right]\right\}\right]^{-1} = \frac{N_0/2}{(2\,\pi)^2 E_{\mathrm{p}}\,\beta^2} = \frac{1}{8\,\pi^2\,\beta^2\,\mathsf{SNR}} \tag{5.25}$$

where $\mathsf{SNR} \triangleq E_{\mathrm{p}}/N_0$, β is the effective bandwidth of $p(t)$ defined as

$$\beta^2 = \frac{\int_{-\infty}^{\infty} f^2 |P(f)|^2\, df}{E_{\mathrm{p}}} \tag{5.26}$$

and $P(f)$ is the Fourier transform of $p(t)$. If $g(t)$ is an even function, as is usual in many practical cases, (5.26) can be rewritten as $\beta^2 = f_{\mathrm{c}}^2 + \beta_g^2$ where

$$\beta_g^2 = \frac{\int_{-\infty}^{\infty} f^2 |G(f)|^2\, df}{E_{\mathrm{p}}} \tag{5.27}$$

and $G(f)$ is the Fourier transform of $g(t)$. Notice that the denominator of (5.25) is proportional to the energy in the signal, where the constant β depends on the bandwidth of the pulse through (5.26). Thus, a large value of β, i.e., a signal with wide transmission bandwidth and/or large center frequency f_{c}, is beneficial for ranging. This justifies the adoption of wideband or, better yet, UWB signals to achieve accurate ranging.

The CRB in (5.25) is meaningful when $p(t)$ is completely known at the receiver and the phase of the transmitted pulse has been retained at the receiver (coherent estimator). When the phase of the transmitted pulse is uncontrolled[6] or the estimator is not coherent, the phase of the transmitted pulse cannot be used to provide additional information about the TOA. Hence, estimation of the TOA must rely only on the signal envelope. In this case

---

[5] We will consider the CRB for the case where τ is a non-random parameter. Extension to the random parameter case is straightforward provided that the prior distribution of τ satisfies regularity conditions [75]. We restrict our attention to the non-random case since under a uniformly distributed prior for τ such conditions are not satisfied and the random parameter version of the CRB does not provide meaningful results.

[6] For example, random variations of the carrier phase will occur if the local oscillator used to generate $p(t)$ is not synchronized with the generator of the baseband pulse $g(t)$. For a discussion regarding the relationship between the ZZB for the coherent and noncoherent cases see [94].

the CRB has to be evaluated considering the equivalent lowpass received signal instead of the bandpass signal. This leads to an expression similar to (5.25) with β replaced by β_g, the effective bandwidth of the baseband pulse $g(t)$ [95], and the resulting bound depends only on the signal bandwidth and not on the center frequency f_c.

5.3.2 The Ziv-Zakai Bound in Ideal Conditions

The ZZB (5.21) relies on the expression for the error probability, $P_{\min}(z)$, of the optimum binary detector for deciding between the two hypothesis H_1 and H_2 described in (5.19). It is well known that the optimum binary detector in AWGN passes the input signal $r(t)$ through a filter matched to the signal $p(t-\zeta) - p(t-\zeta-z)$ and samples the output at time $t = T_{\text{ob}}$. If the resulting output is positive, hypothesis H_1 is chosen; otherwise H_2 is chosen. The probability of error is therefore

$$P_{\min}(z) = Q\left(\sqrt{\mathsf{SNR}\left(1 - \rho_p(z)\right)}\right) \tag{5.28}$$

where $Q(\cdot)$ is the Gaussian Q-function [96]. The expression in (5.28) is for coherent TOA estimation. In the noncoherent case the appropriate expression is given by (5.28) with $\rho_p(\cdot)$ replaced by $\rho_g(\cdot)$, the normalized autocorrelation of the baseband pulse.[7] In the remaining part of the paper we will consider only bounds for coherent TOA estimators.

5.3.3 Numerical Examples Using UWB Pulses in AWGN

Derivatives of Gaussian pulses have been used to analyze the performance of UWB systems [2], and have been proposed to meet FCC UWB emission limits [97]. The nth derivative of a Gaussian pulse is given by

$$g(t) = K_n g_0^{(n)}(t) \quad \text{for } n > 0\,, \tag{5.29}$$

where $g_0(t) = \left(\frac{1}{\pi\sigma_g^2}\right)^{1/4} \exp\left(\frac{-t^2}{2\sigma_g^2}\right)$ is the unit-energy Gaussian pulse and $K_n = \left[\frac{\sigma_g^{2n}}{\sqrt{\pi}}\Gamma\left(n+\frac{1}{2}\right)\right]^{-1/2}$ is a normalization constant that ensures $g(t)$ has unit energy.[8] The parameter σ_g affects both the pulse width and bandwidth. It can be shown that $g(t)$

---

[7] Note that, when $p(t) = \Re\{g(t)e^{j2\pi f_c t}\}$, $\rho_p(z) = \Re\{\rho_g(z)e^{j2\pi f_c z}\}$.

[8] The notation $g_0^{(n)}(t)$ is used to denote the nth derivative of $g_0(t)$ with respect to t, and $\Gamma(\cdot)$ denotes the Gamma function.

has an effective bandwidth $\beta_g^{(n)}$ given by

$$\beta_g^{(n)} = \sqrt{\frac{2n+1}{8\pi^2\sigma_g^2}}\,. \tag{5.30}$$

From (5.30) we can observe that larger effective bandwidth, and hence a lower CRB for TOA estimation, can be achieved by increasing n or decreasing σ_g.[9]

Alternatively, [93] suggests the following RRC pulse

$$g(t) = \frac{4\nu}{\pi\sqrt{\tau_p}} \frac{\cos\left((1+\nu)\pi t/\tau_p\right) + \sin\left((1-\nu)\pi t/\tau_p\right)/(4\nu t/\tau_p)}{1-(4\nu t/\tau_p)^2}\,, \tag{5.31}$$

where the parameter τ_p and roll-off factor ν determine the transmitted signal bandwidth $W = (1+\nu)/\tau_p$. In this case it can be shown that the effective bandwidth of the RRC pulse is given by

$$\beta_g = \sqrt{\frac{\pi^2 - 24\nu^2 + 3\pi^2\nu^2}{12\pi^2\tau_p^2}}\,. \tag{5.32}$$

Figure 5-1 shows the RMSE for the CRB and ZZB using 2nd order Gaussian monocycle pulses and RRC pulses at a center frequency of 4 GHz. As recommended in [93], the RRC pulses have roll-off factor $\nu = 0.6$, $\tau_p = 1\,\text{ns}$ and $\tau_p = 3.2\,\text{ns}$ corresponding to transmission bandwidths of $W = 1.6\,\text{GHz}$ and $W = 500\,\text{MHz}$. The effective bandwidths in these two cases are: $\beta = 4.0125\,\text{GHz}$ and $\beta = 4.0012\,\text{GHz}$. The 2nd order Gaussian pulses with these effective bandwidths are given by $\sigma_g = 0.794\,\text{ns}$ and $\sigma_g = 2.541\,\text{ns}$, respectively.

The presence of the threshold effect can be immediately seen from the ZZB curves. In fact, the a priori region is clearly indicated by the ZZB curves, which approach $T_\text{a}/\sqrt{12}$ for low SNR values. However, the CRB does not account for this behavior. For high SNRs, i.e., in the asymptotic region, the estimation error approaches the value predicted by the CRB. The value of the CRB is essentially the same for $\tau_p = 1\,\text{ns}$ and $\tau_p = 3.2\,\text{ns}$, since the effective bandwidth is primarily determined by f_c when $W \ll f_\text{c}$. When the effective bandwidths are the same, the ZZB curves are nearly identical, with only minor differences occurring in the ambiguity region, due to the pulse shape. Note that a gap, in terms of RMSE, between the ZZB and the CRB can be observed in the ambiguity region between 12 dB and 30 dB for a RRC pulse with $\tau_p = 3.2\,\text{ns}$. In general, for a signal with rectangular

---

[9] As the differentiation order n increases, (5.30) can be used to verify that $\beta_g^{(n)}/\beta_g^{(n+1)}$ tends to 1 for large n, indicating that the improvement in the CRB by increasing n is limited.

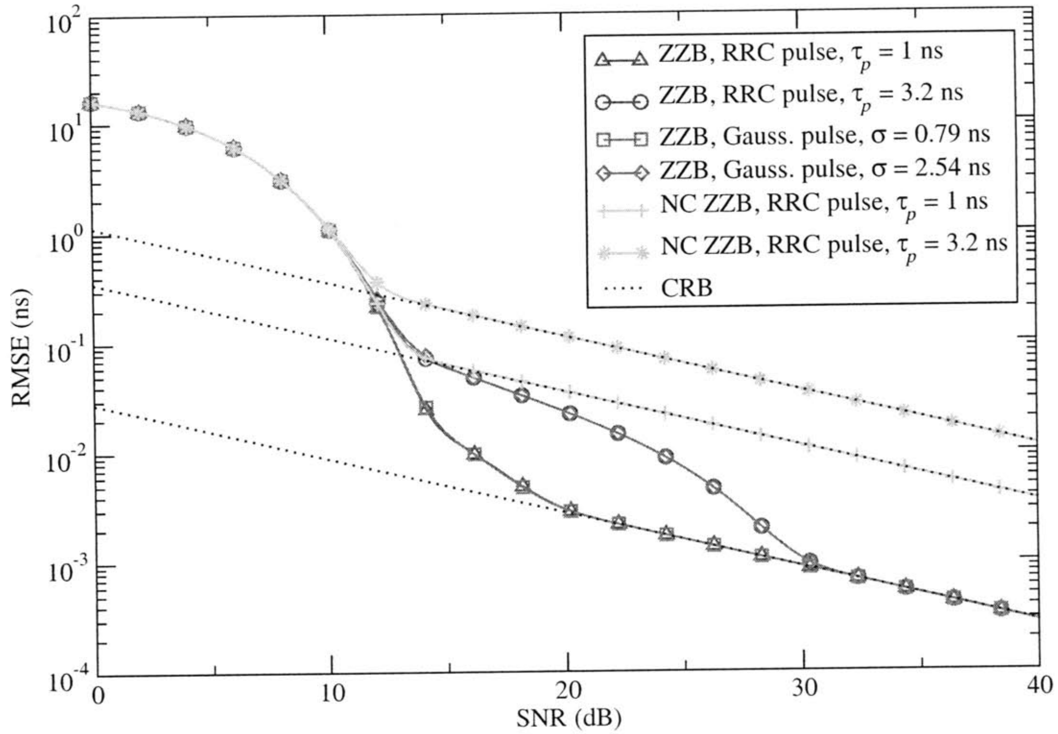

Figure 5-1: CRB and ZZB on the RMSE as a function of SNR in an AWGN channel with $T_{\mathrm{a}} = 100\,\mathrm{ns}$ and $f_{\mathrm{c}} = 4\,\mathrm{GHz}$. Bandpass 2nd-order Gaussian monocycle pulses with $\sigma = 0.79\,\mathrm{ns}$ and $\sigma = 2.54\,\mathrm{ns}$, as well as bandpass RRC pulses with $\nu = 0.6$, $\tau_p = 1\,\mathrm{ns}$ and $\tau_p = 3.2\,\mathrm{ns}$, respectively, are considered. Coherent and noncoherent estimators are shown.

spectrum, the RMSE gap depends on the ratio between the center frequency f_{c} and the signal bandwidth W as discussed in [77, 90]. In particular, having small f_{c}/W leads to a lower RMSE for medium SNR. In fact, as τ_p is decreased to 1 ns, that is increasing W, the ambiguity region begins to vanish. It is evident that the CRB is loose even for the AWGN channel, except in the high SNR region. For comparison purposes the CRB and ZZB for the noncoherent case are also reported in Fig. 5-1 using RRC pulses. As expected the resulting bounds increase significantly.

5.3.4 Extending the Bounds to the Multipath Case

When evaluating the bound on the MSE of the estimation of a single parameter in the presence of several nuisance parameters, three different approaches can be followed. In the first one, referred to as *conditional bounding*, the (scalar) bound on the parameter of interest is evaluated conditioned on the nuisance parameters and then the result is averaged over the nuisance parameters. In the second approach, referred to as *averaging bounding*, the likelihood functional is first marginalized over the nuisance parameters and then the scalar bound on the parameter of interest is determined. Finally, in the third approach, referred to as *joint bounding*, the joint bound on all parameters is derived and then the bound for the parameter of interest is selected. It has been shown that bounds obtained using the averaging approach are always tighter than bounds obtained using the conditioning approach [87,98]. The joint bounding approach instead gives different results depending on the problem. In any case, the suitability of each approach is strictly related to the a priori knowledge of the receiver regarding the nuisance parameters (accounting for the multipath), thus leading to different bounds. In subsequent sections we focus on the derivation of the CRB and the ZZB for two cases of interest: where the receiver 1) has perfect knowledge of the CPR using the conditional bounding approach, and 2) has statistical knowledge of the CPR using the averaging bounding approach.

5.4 Receiver with Perfect Knowledge of the CPR

Although it may be unrealistic to assume that the receiver has perfect knowledge of the CPR, this case can provide insights into the TOA estimation performance. Any estimator we design can never be better than a hypothetical estimator in which the receiver first measures the CPR perfectly, and then performs the estimation conditioned on that CPR. In this case the bound is derived conditioned on the channel realization (i.e., the nuisance parameters), then the unconditional bound is determined by averaging over all possible channel realizations. We refer to this approach as conditional bounding and is also known as the *perfect measurement bound* [75].

5.4.1 Cramér-Rao Bound

The first step is to obtain the expression for the CRB conditioned on the CPR $s(t)$ as

$$\mathsf{CRB}(s(t)) = \left[-\mathbb{E}\left\{\frac{\partial^2}{\partial\zeta^2}\ln\Lambda\left[r(t)|s(t);\tau\right]\right\}\right]^{-1}. \tag{5.33}$$

In this case, the likelihood functional $\Lambda\left[r(t)|s(t);\tau\right]$, similar to (5.23), is given by

$$\Lambda\left[r(t)|s(t);\tau\right] = \exp\left\{-\frac{1}{N_0}\int_0^{T_{\text{ob}}} s^2(t-\tau) - 2s(t-\tau)r(t)\,dt\right\}, \tag{5.34}$$

and it can be shown that

$$\mathsf{CRB}(s(t)) = \frac{1}{8\,\pi^2\,\beta_s^2\,\mathsf{SNR}}\,, \tag{5.35}$$

where $\beta_s^2 = \int_{-\infty}^{\infty} f^2\,|S(f)|^2\,df$. Using the model described in Sec. 5.1, we can equivalently write

$$\mathsf{CRB}(\mathbf{v}) = \frac{1}{2\,\mathbf{v}^T\boldsymbol{\Upsilon}\mathbf{v}\,\mathsf{SNR}}\,, \tag{5.36}$$

where

$$\boldsymbol{\Upsilon} = \begin{bmatrix} \dot{\mathbf{R}} + (2\pi f_c)^2\mathbf{R}(0) & 4\pi f_c \mathbf{R}_{g\dot{g}} \\ -4\pi f_c \mathbf{R}_{g\dot{g}} & \dot{\mathbf{R}} + (2\pi f_c)^2\mathbf{R}(0) \end{bmatrix}. \tag{5.37}$$

Here, $\mathbf{R}(z)$ is a matrix with elements $R(z)_{kl} = \rho_g(z + (l-k)/W)$, $\dot{\mathbf{R}}$ is a symmetric matrix with elements $\dot{R}_{kl} = \int \dot{g}(t - \frac{k-1}{W})\dot{g}(t - \frac{l-1}{W})\,dt$, and $\mathbf{R}_{g\dot{g}}$ is a skew-symmetric matrix with elements $R_{g\dot{g}kl} = \int g(t - \frac{k-1}{W})\dot{g}(t - \frac{l-1}{W})\,dt$. The next step is to average (5.36) over the nuisance parameters $\mathbf{v}$. A related approach was adopted in [99], where averaging of (5.35) was carried out using CPRs generated according to IEEE 802.15.3a UWB channel models. In our case, averaging (5.36) can give misleading results since the CRB is valid only for large values of the quantity $\mathbf{v}^T\boldsymbol{\Upsilon}\mathbf{v}$. In other words, for certain realizations of the channel parameters the denominator of (5.36) assumes low values (including zero) resulting in high contributions during the averaging process, which can potentially lead to erroneous results. Alternatively, the use of Jensen's inequality results in the modified CRB (MCRB) [100] as follows

$$\mathsf{CRB} = \mathbb{E}_{\mathbf{v}}\{\mathsf{CRB}(\mathbf{v})\} \geq \frac{1}{2\,\mathbb{E}\left\{\mathbf{v}^T\boldsymbol{\Upsilon}\mathbf{v}\right\}\,\mathsf{SNR}} = \frac{1}{2\left((2\pi)^2\beta^2\sum_{l=1}^{2L}\sigma_l^2 + \boldsymbol{\mu}^T\boldsymbol{\Upsilon}\boldsymbol{\mu}\right)\,\mathsf{SNR}} \tag{5.38}$$

where we have used the fact that $\mathbb{E}\left\{\mathbf{v}\mathbf{v}^T\right\} = \boldsymbol{\Psi} + \boldsymbol{\mu}\boldsymbol{\mu}^T$ and $\dot{R}_{kk} = (2\pi)^2\beta_g^2$. Note that, in some cases, the bound in (5.38) is the same as the one in (5.25): 1) when there is no mean component ($\boldsymbol{\mu} = \mathbf{0}$), 2) when μ_l and μ_{L+l} are non-zero for only one $l \in [1, 2, \ldots, L]$, or 3) when there is no overlap between adjacent pulses. This can be seen as follows. In the first case, when $\boldsymbol{\mu} = \mathbf{0}$, the second term in the denominator of (5.38) becomes zero and

$\sum_{l=1}^{2L} \sigma_l^2 = 1$, due to normalization. For the second and third cases, expanding the second term in the denominator gives:

$$\begin{aligned}\boldsymbol{\mu}^T \boldsymbol{\Upsilon} \boldsymbol{\mu} = (2\pi f_{\mathrm{c}})^2 \left(\boldsymbol{\mu}_1^T \mathbf{R}(0) \boldsymbol{\mu}_1 + \boldsymbol{\mu}_2^T \mathbf{R}(0) \boldsymbol{\mu}_2 \right) + \boldsymbol{\mu}_1^T \dot{\mathbf{R}} \boldsymbol{\mu}_1 + \boldsymbol{\mu}_2^T \dot{\mathbf{R}} \boldsymbol{\mu}_2 \\ + 4\pi f_{\mathrm{c}} \left(\boldsymbol{\mu}_1^T \mathbf{R}_{g\dot{g}} \boldsymbol{\mu}_2 - \boldsymbol{\mu}_2^T \mathbf{R}_{g\dot{g}} \boldsymbol{\mu}_1 \right) \,,\end{aligned}$$

where $\boldsymbol{\mu}_1 = [\mu_1,\ \mu_2, \ldots, \mu_L]^T$ and $\boldsymbol{\mu}_2 = [\mu_{L+1},\ \mu_{L+2}, \ldots, \mu_{2L}]^T$. For the case when μ_l and μ_{L+l} are non-zero for only one $l \in [1,\ 2, \ldots, L]$, it can be shown that

$$\begin{aligned}\boldsymbol{\mu}^T \boldsymbol{\Upsilon} \boldsymbol{\mu} &= (2\pi f_{\mathrm{c}})^2 \left(\mu_l^2 + \mu_{L+l}^2 \right) R(0)_{ll} + \left(\mu_l^2 + \mu_{L+l}^2 \right) \dot{R}_{ll} \\ &= (2\pi)^2 \beta^2 \left(\mu_l^2 + \mu_{L+l}^2 \right) \,,\end{aligned}$$

where in the second line we have used the fact that $R(0)_{ll} = 1$ and $\dot{R}_{ll} = (2\pi)^2 \beta_g^2$. Finally, when there is no overlap between adjacent pulses it can be shown that $\mathbf{R}(0) = \mathbf{I}_L$, $\dot{\mathbf{R}} = (2\pi)^2 \beta_g^2 \mathbf{I}_L$, and $\mathbf{R}_{g\dot{g}} = \mathbf{0}$. Thus, in this case for arbitrary $\boldsymbol{\mu}$, $\boldsymbol{\mu}^T \boldsymbol{\Upsilon} \boldsymbol{\mu} = (2\pi)^2 (f_{\mathrm{c}}^2 + \beta_g^2) \boldsymbol{\mu}^T \boldsymbol{\mu}$.

5.4.2 Ziv-Zakai Bound

Infinite Ensemble of CPRs

As discussed in Sec. 5.2, the ZZBT bound requires the evaluation of the error probability of the optimum detector, $P_{\min}(z)$, for deciding between the two hypothesis H_1 and H_2 described in (5.19). The test we design can never be better than a "genie test" in which a genie provides the receiver with the perfect CPR $s(t)$ (or, equivalently, $\mathbf{v}$) and then the receiver performs the optimum likelihood ratio test conditioned on that CPR. This is equivalent to evaluating the error probability $P_{\min}(z, \mathbf{v})$ corresponding to a classical binary communication system employing the real waveforms $s(t - \zeta, \mathbf{v})$ and $s(t - \zeta - z, \mathbf{v})$ for hypothesis H_1 and H_2, respectively, with known $\mathbf{v}$. Therefore, the error probability is given by

$$P_{\min}(z, \mathbf{v}) = Q\left(\sqrt{\mathsf{SNR}\big(\rho_s(0, \mathbf{v}) - \rho_s(z, \mathbf{v})\big)} \right) \tag{5.39}$$

where we have defined the normalized autocorrelation function

$$\begin{aligned}\rho_s(z,\mathsf{v}) &= \frac{1}{E_\mathrm{p}}\int_{-\infty}^{\infty} s(t-\zeta,\mathsf{v})\,s(t-\zeta-z,\mathsf{v})\,dt \\ &= \sum_{k=1}^{L}\sum_{l=1}^{L}\Big[\mathsf{v}_k\mathsf{v}_l\cos(2\pi f_\mathrm{c}z)+\mathsf{v}_k\mathsf{v}_{L+l}\sin(2\pi f_\mathrm{c}z) \\ &\qquad\qquad -\mathsf{v}_{L+k}\mathsf{v}_l\sin(2\pi f_\mathrm{c}z)+\mathsf{v}_{L+k}\mathsf{v}_{L+l}\cos(2\pi f_\mathrm{c}z)\Big]\rho_g\left(z+\frac{l-k}{W}\right) \\ &= \mathsf{v}^T\mathbf{R}_2(z)\mathsf{v}\,, \end{aligned} \tag{5.40}$$

and

$$\mathbf{R}_2(z) \triangleq \left(\begin{bmatrix}\cos(2\pi f_\mathrm{c}z) & \sin(2\pi f_\mathrm{c}z)\\ -\sin(2\pi f_\mathrm{c}z) & \cos(2\pi f_\mathrm{c}z)\end{bmatrix}\otimes\mathbf{R}(z)\right). \tag{5.41}$$

By replacing $P_{\min}(z)$ with $P_{\min}(z,\mathsf{v})$ in (5.21), we obtain the ZZBT bound conditioned on v as

$$\mathsf{ZZB}(\mathsf{v}) = \frac{1}{T_\mathrm{a}}\int_0^{T_\mathrm{a}} z\,(T_\mathrm{a}-z)\,P_{\min}(z,\mathsf{v})\;dz\,. \tag{5.42}$$

Starting from (5.42) the unconditional ZZBT bound can be evaluated by averaging over v, that is,

$$\mathsf{ZZB} = \int_{\mathbb{R}^{2L}} f_\mathsf{v}(\boldsymbol{v})\,\mathsf{ZZB}(\boldsymbol{v})\,d\boldsymbol{v} = \frac{1}{T_\mathrm{a}}\int_0^{T_\mathrm{a}} z\,(T_\mathrm{a}-z)\,P_{\min}^{(\mathrm{av})}(z)\,dz \tag{5.43}$$

where

$$P_{\min}^{(\mathrm{av})}(z) \triangleq \int_{\mathbb{R}^{2L}} f_\mathsf{v}(\boldsymbol{v})\,P_{\min}(z,\boldsymbol{v})\;d\boldsymbol{v}\,. \tag{5.44}$$

We stress that (5.43) assumes that the receiver has perfect knowledge of the CPR, and hence serves as a lower bound on the TOA when the receiver measures the CPR perfectly. Note that (5.44) is the average bit error probability (BEP) for coherent detection of binary pulse position modulation (PPM) employing a Rake receiver in the presence of multipath assuming perfect channel state information. Such BEP expressions are known in the literature and can be used to derive the ZZB [92, 101–103]. Similar to [92], we take an approach that leverages the well-known identity [48]:

$$Q(x) = \frac{1}{\pi} \int_0^{\pi/2} \exp\left\{ -\frac{x^2}{2\sin^2\theta} \right\} d\theta \,. \tag{5.45}$$

Using, (5.45) in (5.39) gives

$$P_{\min}(z, \mathbf{v}) = \frac{1}{\pi} \int_0^{\pi/2} \exp\left\{ -\frac{\mathsf{SNR}\, \mathbf{v}^T \left(\mathbf{R}_2(0) - \mathbf{R}_2(z)\right) \mathbf{v}}{2\sin^2\theta} \right\} d\theta \,, \tag{5.46}$$

and thus

$$\mathbb{E}_{\mathbf{v}}\{P_{\min}(z, \mathbf{v})\} = \frac{1}{\pi} \int_0^{\pi/2} \mathbb{E}_{\mathbf{v}}\left\{ \exp\left\{ -\frac{\mathsf{SNR}\, \mathbf{v}^T \left(\mathbf{R}_2(0) - \mathbf{R}_2(z)\right) \mathbf{v}}{2\sin^2\theta} \right\} \right\} d\theta \,. \tag{5.47}$$

We recognize that the integrand in (5.47) is equivalent to averaging over the scalar quantity $\varrho \triangleq \mathbf{v}^T \left(\mathbf{R}_2(0) - \mathbf{R}_2(z)\right) \mathbf{v} = \mathbf{v}^T \mathbf{T} \mathbf{v}$, where $\mathbf{T}$ is a symmetric matrix given by

$$\mathbf{T} = \mathbf{R}_2(0) - \frac{1}{2} \left(\mathbf{R}_2(z) + \mathbf{R}_2(z)^T \right) \,.$$

Furthermore, the integrand can be replaced by the MGF of ϱ evaluated at $-\mathsf{SNR}/\left(2\sin^2\theta\right)$. Using the results of [104] the MGF can be derived as

$$M_\varrho(t) = \frac{\exp\left\{ t \boldsymbol{\mu}^T \mathbf{T} \left(\mathbf{I}_{2L} - 2t\boldsymbol{\Psi}_2\mathbf{T}\right)^{-1} \boldsymbol{\mu} \right\}}{\det\{\mathbf{I}_{2L} - 2t\boldsymbol{\Psi}_2\mathbf{T}\}^{1/2}} \,. \tag{5.48}$$

We note that the evaluation of $P_{\min}^{(\mathrm{av})}(z)$ no longer requires the $2L$-fold multidimensional integration of (5.44), instead we need only evaluate a single integral with finite limits over $M_\varrho\left(-\mathsf{SNR}/\left(2\sin^2\theta\right)\right)$.

Finite Ensemble of CPRs

When a finite ensemble of CPRs is available, with proper change of notation, the ZZB becomes

$$\mathsf{ZZB} = \frac{1}{N_{\mathrm{CPR}}} \sum_{k=1}^{N_{\mathrm{CPR}}} \mathsf{ZZB}\left(s^{(k)}(t)\right) \,, \tag{5.49}$$

where $\mathsf{ZZB}\left(s^{(k)}(t)\right)$ can be evaluated using (5.42) by replacing $P_{\min}(z, \mathbf{v})$ with $P_{\min}\left(z, s^{(k)}(t)\right)$, denoting the error probability of an optimum binary detection scheme employing the waveforms $s^{(k)}(t-\zeta)$ and $s^{(k)}(t-\zeta-z)$. In a Monte Carlo framework (5.49) approximates (5.43) thus avoiding multi-dimensional integration (5.44) when it is impractical. In [88], equation (5.49) was used in conjunction with experimentally measured data to evaluate the ZZB on TOA estimation in realistic environments.

5.5 Receiver with Statistical Knowledge of the CPR

A priori statistical information of the CPR can be exploited in the estimator to improve estimation accuracy. The bound on the MSE in this case is derived by first marginalizing the conditional PDF over the nuisance parameters, and then evaluating the scalar bound on the parameter of interest. The derivation of the bound is strictly dependent on the channel model considered. In general the evaluation of the bound for channel models with generic fading statistics may not be analytically tractable. Therefore we restrict our analysis to the widely used Rayleigh/Rice channel models. Alternatively, one can adopt Monte Carlo techniques to approximate the result by considering a finite set of channel realizations.

5.5.1 Cramér-Rao Bound

Here we treat only the case of a uncountably infinite ensemble of CPRs. The extension to the finite case is straightforward. Substituting (5.13) into (5.34), gives

$$\Lambda\left[r(t)|\mathsf{v};\tau\right] = \exp\Bigg\{ -\mathsf{SNR}\Bigg(\sum_{k=1}^{L}\sum_{l=1}^{L} (\mathsf{v}_k\mathsf{v}_l + \mathsf{v}_{k+L}\mathsf{v}_{l+L})\,\rho_g((k-l)\Delta\tau) \\ - 2\sum_{k=1}^{L} \mathsf{v}_k\, q_k^{\mathrm{I}}(\tau) + \mathsf{v}_{k+L}\, q_k^{\mathrm{Q}}(\tau)\Bigg)\Bigg\} \tag{5.50}$$

where we have defined

$$q_k^{\mathrm{I}}(\tau) \triangleq \frac{1}{E_{\mathrm{p}}}\int_0^{T_{\mathrm{ob}}} r(t)p_k^{\mathrm{I}}(t-\tau)\,dt \tag{5.51}$$

$$q_k^{\mathrm{Q}}(\tau) \triangleq \frac{1}{E_{\mathrm{p}}}\int_0^{T_{\mathrm{ob}}} r(t)p_k^{\mathrm{Q}}(t-\tau)\,dt \tag{5.52}$$

and

$$p_k^{\mathrm{I}}(t) \triangleq \sqrt{2E_{\mathrm{p}}}\, g(t-(k-1)\Delta\tau)\cos(2\pi f_{\mathrm{c}} t) \tag{5.53}$$

$$p_k^{\mathrm{Q}}(t) \triangleq -\sqrt{2E_{\mathrm{p}}}\, g(t-(k-1)\Delta\tau)\sin(2\pi f_{\mathrm{c}} t)\,. \tag{5.54}$$

The expression in (5.50) can be rewritten as

$$\Lambda\left[r(t)|\mathbf{v};\tau\right] = \\ \exp\left\{-\mathsf{SNR}\,\mathrm{tr}\left\{\mathbf{R}_2(0)\left[\mathbf{v}-\mathbf{R}_2(0)^{-1}\mathbf{q}(\tau)\right]\left[\mathbf{v}-\mathbf{R}_2(0)^{-1}\mathbf{q}(\tau)\right]^T-\mathbf{R}_2(0)^{-1}\mathbf{q}(\tau)\mathbf{q}(\tau)^T\right\}\right\}, \tag{5.55}$$

where

$$\mathbf{q}(\tau) = \left[q_1^{\mathrm{I}}(\tau),\, q_2^{\mathrm{I}}(\tau),\, \ldots,\, q_L^{\mathrm{I}}(\tau),\, q_1^{\mathrm{Q}}(\tau),\, q_2^{\mathrm{Q}}(\tau),\, \ldots,\, q_L^{\mathrm{Q}}(\tau)\right]^T.$$

Note that $\mathbf{R}_2(0) = \mathbf{I}_2 \otimes \mathbf{R}(0)$ is a symmetric matrix.

According to the averaging bounding approach, we can utilize the single parameter bound based on the likelihood functional $\Lambda\left[r(t);\tau\right]$ evaluated by averaging the conditional likelihood functional $\Lambda\left[r(t)|\mathbf{v};\tau\right]$ over the nuisance parameters $\mathbf{v}$. We note that the quantity in the exponent of (5.55) is related to a non-central Wishart distribution, and thus the expression for $\Lambda\left[r(t);\tau\right]$ can be determined from the MGF of such a distribution. Applying expressions in [104], the likelihood functional for Rayleigh/Rice fading can be written as

$$\Lambda\left[r(t);\tau\right] = \exp\left\{-\frac{1}{2}\mathrm{tr}\left\{\mathbf{\Psi}_2^{-1}\boldsymbol{\mu}\boldsymbol{\mu}^T\right\}\right\} \\ \times \frac{\exp\left\{2\,\mathsf{SNR}^2\,\mathrm{tr}\left\{\left[\mathbf{I}_{2L}+2\,\mathsf{SNR}\,\mathbf{\Psi}_2\mathbf{R}_2(0)\right]^{-1}\mathbf{\Psi}_2\left[\mathbf{q}(\tau)+\frac{1}{2\,\mathsf{SNR}}\mathbf{\Psi}_2^{-1}\boldsymbol{\mu}\right]\left[\mathbf{q}(\tau)+\frac{1}{2\,\mathsf{SNR}}\mathbf{\Psi}_2^{-1}\boldsymbol{\mu}\right]^T\right\}\right\}}{\det\left\{\mathbf{I}_L+2\,\mathsf{SNR}\,\mathbf{\Psi}\mathbf{R}(0)\right\}}. \tag{5.56}$$

Starting from (5.56), it is shown in Appendix B that the CRB is given by

$$\begin{aligned}\mathsf{CRB} &= \left[-\mathbb{E}\left\{\frac{\partial^2}{\partial\tau^2}\ln\Lambda\left[r(t);\tau\right]\right\}\right]^{-1} \\ &= \Bigg[2\,\mathsf{SNR}\,\boldsymbol{\mu}^T\boldsymbol{\Upsilon}\boldsymbol{\mu} \\ &\quad + 4\,\mathsf{SNR}^2\,\mathrm{tr}\left\{\left(\mathbf{I}_{2L}+2\,\mathsf{SNR}\,\boldsymbol{\Psi}_2\mathbf{R}_2(0)\right)^{-1}\boldsymbol{\Psi}_2\left(\boldsymbol{\Upsilon}\boldsymbol{\Psi}_2\mathbf{R}_2(0)-\boldsymbol{\Xi}(\boldsymbol{\Psi}_2+\boldsymbol{\mu}\boldsymbol{\mu}^T)\boldsymbol{\Xi}^T\right)\right\}\Bigg]^{-1},\end{aligned} \tag{5.57}$$

where the matrices $\boldsymbol{\Upsilon}$ and $\boldsymbol{\Xi}$ are given in (5.37) and (B.5), respectively. Note that the result in (5.57) is an expression for the CRB that takes into account the available a priori information about the multipath components, and thus serves as a lower bound on the TOA estimation error when the receiver has statistical knowledge of the CPR.

5.5.2 Ziv-Zakai Bound

In this section, the ZZB is derived for both the case of infinite and finite ensembles of CPR realizations. In the former, $\mathbf{v}$ is considered to be a vector of RVs with known distribution at the receiver. In the latter, the receiver knows the entire ensemble of CPR realizations $\{s^{(k)}(t)\}_{k=1}^{N_{\mathrm{CPR}}}$ but not the exact CPR realization that has been received. As shown in Sec. 5.3.2 the steps to determine the ZZB are to first design the optimum binary detector (5.20), evaluate its performance $P_{\min}(z)$, and then use $P_{\min}(z)$ to evaluate (5.21).

Infinite Ensemble of CPRs

The starting point is the binary detection scheme with equally probable hypotheses as in Sec. 5.3.2. To obtain the averaging bound, $P_{\min}(z)$ has to correspond to the minimum attainable error probability of the *binary composite hypothesis testing* problem in the presence of nuisance parameters. For this reason the likelihood ratio test in (5.20) requires the marginal likelihood functional (5.56). The corresponding log-likelihood ratio (LLR) is

$$\begin{aligned} l(r(t)) &= \ln \frac{\Lambda\left[r(t)|\tau=\zeta\right]}{\Lambda\left[r(t)|\tau=\zeta+z\right]} \\ &= \mathrm{tr}\Bigg\{ 2\,\mathsf{SNR}^2 \left(\mathbf{I}_{2L} + 2\,\mathsf{SNR}\,\mathbf{\Psi}_2\mathbf{R}_2(0)\right)^{-1}\mathbf{\Psi}_2 \\ &\quad \times \Bigg[\left(\mathbf{q}(\zeta) + \frac{1}{2\,\mathsf{SNR}}\mathbf{\Psi}_2^{-1}\boldsymbol{\mu}\right)\left(\mathbf{q}(\zeta) + \frac{1}{2\,\mathsf{SNR}}\mathbf{\Psi}_2^{-1}\boldsymbol{\mu}\right)^T \\ &\quad - \left(\mathbf{q}(\zeta+z) + \frac{1}{2\,\mathsf{SNR}}\mathbf{\Psi}_2^{-1}\boldsymbol{\mu}\right)\left(\mathbf{q}(\zeta+z) + \frac{1}{2\,\mathsf{SNR}}\mathbf{\Psi}_2^{-1}\boldsymbol{\mu}\right)^T \Bigg]\Bigg\} \end{aligned} \tag{5.58}$$

The detector evaluates $l(r(t))$ and decides for hypothesis H_1 if $l(r(t)) > 0$, otherwise hypothesis H_2 is chosen.[10] From (5.58), the decision variable under hypothesis H_1 is

$$\mathsf{y} = l(r(t)|H_1) = \mathrm{tr}\left\{\mathbf{SU}\right\}, \tag{5.59}$$

where S is a $4L \times 4L$ block diagonal matrix

$$\mathbf{S} \triangleq 2\,\mathsf{SNR}^2 \begin{bmatrix} \mathbf{I}_2 & \mathbf{0} \\ \mathbf{0} & -\mathbf{I}_2 \end{bmatrix} \otimes \left[\mathbf{I}_L + 2\,\mathsf{SNR}\,\mathbf{\Psi}\mathbf{R}(0)\right]^{-1}\mathbf{\Psi} \tag{5.60}$$

and $\mathbf{U} = (\mathbf{x}+\mathbf{m})(\mathbf{x}+\mathbf{m})^T$. The vector $\mathbf{x}$ is a $4L \times 1$ zero mean random vector given by

$$\mathbf{x} \triangleq \begin{bmatrix} \mathbf{q}^{(1)} - \mathbb{E}\left\{\mathbf{q}^{(1)}\right\} \\ \mathbf{q}^{(2)} - \mathbb{E}\left\{\mathbf{q}^{(2)}\right\} \end{bmatrix} \tag{5.61}$$

where $\mathbf{q}^{(1)} \triangleq \mathbf{q}(\zeta)|_{H_1}$ and $\mathbf{q}^{(2)} \triangleq \mathbf{q}(\zeta+z)|_{H_1}$. The corresponding mean vector $\mathbf{m}$ is given by

$$\mathbf{m} = \begin{bmatrix} \mathbb{E}\left\{\mathbf{q}^{(1)}\right\} + \frac{1}{2\,\mathsf{SNR}}\mathbf{\Psi}_2^{-1}\boldsymbol{\mu} \\ \mathbb{E}\left\{\mathbf{q}^{(2)}\right\} + \frac{1}{2\,\mathsf{SNR}}\mathbf{\Psi}_2^{-1}\boldsymbol{\mu} \end{bmatrix}, \tag{5.62}$$

where expressions for the quantities $\mathbb{E}\left\{\mathbf{q}^{(1)}\right\}$ and $\mathbb{E}\left\{\mathbf{q}^{(2)}\right\}$ are given in Appendix C.

The probability of error $P_{\mathsf{min}}(z)$, required to evaluate the ZZB in (5.21), is given by

$$P_{\mathsf{min}}(z) = \frac{1}{2}P_{\mathsf{e}|H_1}(z) + \frac{1}{2}P_{\mathsf{e}|H_2}(z) \tag{5.63}$$

---

[10] Note that the LLR (5.58) leads to the optimal binary PPM Rake receiver (correlator-squarer receiver), which is depicted in Fig. 5-2. To the best of the author's knowledge both the structure and performance of this receiver have not been investigated in the literature.

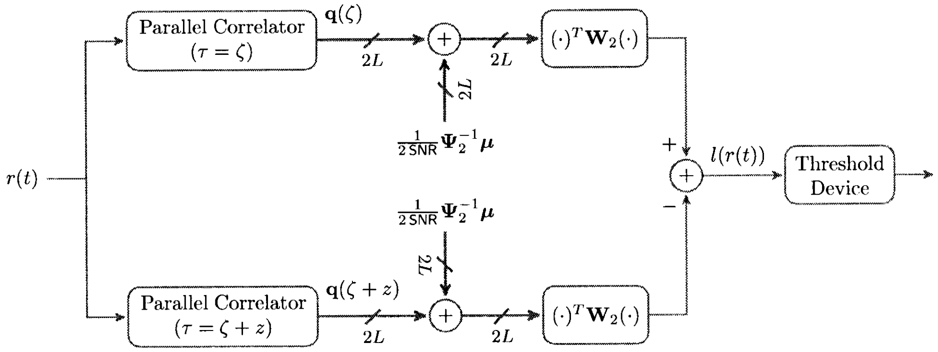

(a) Detector structure

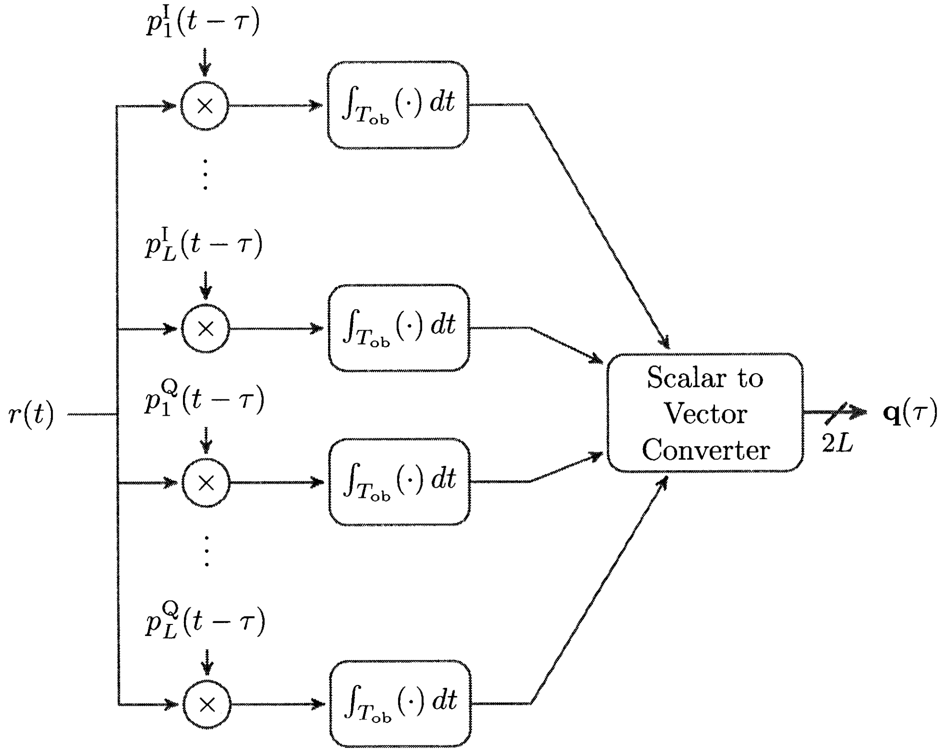

(b) Parallel correlator

Figure 5-2: Optimum detector in the presence of Rayleigh/Rice fading.

where $P_{e|H_1}(z)$ and $P_{e|H_2}(z)$ are the error probabilities conditioned on hypothesis H_1 and H_2, respectively. Since $P_{e|H_1}(z) = P_{e|H_2}(z)$, due to symmetry, it is sufficient to evaluate $P_{e|H_1}(z)$. Thus, the probability of error $P_{\min}(z)$ is given by

$$P_{\min}(z) = P_{e|H_1}(z) = \mathbb{P}\{\mathsf{y} < 0 | H_1\} . \tag{5.64}$$

To evaluate (5.64) it is necessary to characterize the statistics of the RV y. It follows from Appendix C that $\mathbf{x}$ is a zero-mean normal random vector with covariance matrix $\boldsymbol{\Sigma}$ given in

(C.18). Therefore $\mathbf{U}$ follows a noncentral Wishart distribution with one degree of freedom. In order to evaluate the probability in (5.64), we take the approach of first deriving the MGF of y, defined as $\Phi_{\mathsf{y}}(s) \triangleq \mathbb{E}\left\{e^{s\mathsf{y}}\right\}$. Using expressions in [104], the MGF is given by

$$\Phi_{\mathsf{y}}(s) = \frac{\exp\left(\operatorname{tr}\left\{s\mathbf{S}(\mathbf{I}_{4L} - 2s\boldsymbol{\Sigma}\mathbf{S})^{-1}\mathbf{M}\right\}\right)}{\det\left\{\mathbf{I}_{4L} - 2s\boldsymbol{\Sigma}\mathbf{S}\right\}^{1/2}}, \tag{5.65}$$

where $\mathbf{M} = \mathbf{m}\mathbf{m}^T$. To facilitate computation, the denominator above can be rewritten as

$$\det\left\{\mathbf{I}_L - 2s\mathbf{A}\mathbf{W}\right\} \det\left\{\mathbf{I}_L + 2s\mathbf{D}\mathbf{W} + (2s)^2\mathbf{X}^T\mathbf{W}\left(\mathbf{I} - 2s\mathbf{A}\mathbf{W}\right)^{-1}\mathbf{X}\mathbf{W}\right\} \tag{5.66}$$

$$= \det\left\{\mathbf{I}_L - 2\,\mathsf{SNR}\,s\mathbf{R}(0)\boldsymbol{\Psi}\right\}$$

$$\times \det\left\{\mathbf{I}_L + 2s\mathbf{D}\mathbf{W} + (2s)^2\,\mathsf{SNR}\,\mathbf{R}(z)^T\boldsymbol{\Psi}\left(\mathbf{I} - 2\,\mathsf{SNR}\,s\mathbf{R}(0)\boldsymbol{\Psi}\right)^{-1}\mathbf{X}\mathbf{W}\right\} \tag{5.67}$$

where

$$\mathbf{W} = 2\,\mathsf{SNR}^2\left[\mathbf{I}_L + 2\,\mathsf{SNR}\,\boldsymbol{\Psi}\mathbf{R}(0)\right]^{-1}\boldsymbol{\Psi}, \tag{5.68}$$

and $\mathbf{R}(z)$ is defined in Sec. 5.4.1. The matrices $\mathbf{A}$, $\mathbf{D}$, and $\mathbf{X}$ are given in Appendix C. From the above derivation we can see that the denominator in (5.65) does not have any dependence on f_c as $\mathbf{R}(z)$ depends on only the baseband pulse $g(t)$. Furthermore, note that in the case of purely Rayleigh fading, $\mathbf{m} = \mathbf{0}$ and the numerator in (5.65) becomes one. Thus, we do not expect the expression for $P_{\min}(z)$ to exhibit oscillations on the order of f_c and performance should approach that exhibited in the baseband case.

Several techniques are available to evaluate (5.64) using the MGF (5.65). The classical way is to use the Inversion Theorem [105]

$$P_{\min}(z) = \mathbb{P}\left\{\mathsf{y} < 0\right\} = \frac{1}{2} - \frac{1}{\pi}\Re\left\{\int_0^\infty \frac{\Phi_{\mathsf{y}}(\jmath v)}{\jmath v}\,dv\right\}. \tag{5.69}$$

$$= \frac{1}{2} - \frac{1}{\pi}\int_0^\infty \frac{\Im\{\{\}\,\Phi_{\mathsf{y}}(\jmath v)\}}{v}\,dv. \tag{5.70}$$

Finite Ensemble of CPRs

In the case of a finite ensemble of CPRs, the likelihood functional is given by

$$\begin{aligned}\Lambda\left[r(t)|\tau\right] &= \mathbb{E}\left\{\Lambda\left[r(t)|\tau, s(t)\right]\right\}\\ &= \mathbb{E}\left\{\exp\left\{-\frac{1}{N_0}\int_0^{T_{\text{ob}}} s^2(t-\tau) - 2s(t-\tau)r(t)\,dt\right\}\right\}\\ &= \frac{1}{N_{\text{CPR}}}\sum_{i=1}^{N_{\text{CPR}}} \exp\left\{-\frac{1}{N_0}\int_0^{T_{\text{ob}}} \left(s^{(i)}(t-\tau)\right)^2 - 2s^{(i)}(t-\tau)r(t)\,dt\right\}, \end{aligned} \qquad (5.71)$$

where $s^{(i)}(t)$ is the channel response to a pulse with energy E_{p}. The ensemble of available CPRs, $\left\{s^{(i)}(\cdot)\right\}_{i=1}^{N_{\text{CPR}}}$, is normalized to have an average channel gain of unity, i.e., $\frac{1}{N_{\text{CPR}}}\sum_{i}^{N_{\text{CPR}}}\int_{T_{\text{ob}}}\left(s^{(i)}(t)\right)^2 dt = 1$. Using (5.71) the likelihood ratio (LR) in (5.20) becomes

$$L(r(t)) = \frac{\sum_{i=1}^{N_{\text{CPR}}} \exp\left\{-\frac{1}{N_0}\int_{T_{\text{ob}}} \left(s^{(i)}(t-\zeta)\right)^2 - 2s^{(i)}(t-\zeta)r(t)\,dt\right\}}{\sum_{i=1}^{N_{\text{CPR}}} \exp\left\{-\frac{1}{N_0}\int_{T_{\text{ob}}} \left(s^{(i)}(t-\zeta-z)\right)^2 - 2s^{(i)}(t-\zeta-z)r(t)\,dt\right\}}. \qquad (5.72)$$

We evaluate $P_{\min}(z)$ by averaging the conditional error probabilities, conditioned on a given CPR, as follows

$$\begin{aligned}P_{\min}(z) &= \mathbb{E}\left\{\mathbb{P}\left\{L\left(r(t)\right) < 1|s(t), H_1\right\}\right\}\\ &= \frac{1}{N_{\text{CPR}}}\sum_{k=1}^{N_{\text{CPR}}} \mathbb{P}\left\{L\left(r(t)\right) < 1|s^{(k)}(t), H_1\right\} = \frac{1}{N_{\text{CPR}}}\sum_{k=1}^{N_{\text{CPR}}} \mathbb{P}\left\{L\left(r^{(k)}(t)\right) < 1|H_1\right\}\end{aligned} \qquad (5.73)$$

where $r^{(k)}(t) = s^{(k)}(t-\zeta)+n(t)$ is the received signal conditioned on the kth CPR realization under hypothesis H_1.

The LR in (5.73), conditioned on H_1, is given by

$$L\left(r^{(k)}(t)\right)|H_1 = \frac{\sum_{i=1}^{N_{\text{CPR}}}\exp\left\{V_{k,i}\right\}}{\sum_{i=1}^{N_{\text{CPR}}}\exp\left\{W_{k,i}\right\}}, \qquad (5.74)$$

where we have defined

$$V_{k,i} = -\frac{1}{N_0}\int_{T_{\text{ob}}} \left(s^{(i)}(t-\zeta)\right)^2 - 2s^{(i)}(t-\zeta)r^{(k)}(t)\,dt \tag{5.75}$$

$$W_{k,i} = -\frac{1}{N_0}\int_{T_{\text{ob}}} \left(s^{(i)}(t-\zeta-z)\right)^2 - 2s^{(i)}(t-\zeta-z)r^{(k)}(t)\,dt\,. \tag{5.76}$$

The $V_{k,i}$ and $W_{k,i}$ are Gaussian RVs since they are each a function of the AWGN present in $r^{(k)}(t)$. This means that the numerator and denominator of (5.74) are sums of log-normal RVs. Furthermore, the underlying Gaussian RVs are correlated. The properties of the underlying Gaussian RVs can be shown to be

$$\mathbb{E}\left\{V_{k,i}\right\} = \mathsf{SNR}\left(2\rho_s^{(k,i)}(0) - \rho_s^{(i,i)}(0)\right) \tag{5.77}$$

$$\mathbb{E}\left\{W_{k,i}\right\} = \mathsf{SNR}\left(2\rho_s^{(k,i)}(z) - \rho_s^{(i,i)}(0)\right) \tag{5.78}$$

$$\text{Cov}\left\{V_{k,i}, V_{k,j}\right\} = \text{Cov}\left\{W_{k,i}, W_{k,j}\right\} = 2\,\mathsf{SNR}\rho_s^{(i,j)}(0) \tag{5.79}$$

$$\text{Cov}\left\{V_{k,i}, W_{k,j}\right\} = 2\,\mathsf{SNR}\rho_s^{(i,j)}(z)\,, \tag{5.80}$$

where $\rho_s^{(i,j)}(z) = \frac{1}{E_{\text{p}}}\int_0^{T_{\text{ob}}} s^{(i)}(t-\zeta)s^{(j)}(t-\zeta-z)\,dt$.

The exact evaluation of the probabilities in (5.73) appears to be prohibitive. To facilitate evaluation of $P_{\min}(z)$, we make the following approximations in the numerator and denominator of (5.74):

$$Z_{\text{a},k} = \sum_{i=1}^{N_{\text{CPR}}} \exp\left\{V_{k,i}\right\} \simeq \exp\left\{U_{\text{a},k}\right\} \tag{5.81}$$

$$Z_{\text{b},k} = \sum_{i=1}^{N_{\text{CPR}}} \exp\left\{W_{k,i}\right\} \simeq \exp\left\{U_{\text{b},k}\right\} \tag{5.82}$$

where $U_{\text{a},k}$ and $U_{\text{b},k}$ are Gaussian RVs. That is, in (5.81) and (5.82) we take the approach that the distribution of a power sum of Gaussian RVs can be approximated by a single log-normal distribution. This is a natural choice that has been shown to be a good approximation in a variety of cases. The approximations in (5.81) and (5.82), in turn allows $P_{\min}(z)$ to be written as:

$$P_{\min}(z) \simeq \frac{1}{N_{\text{CPR}}}\sum_{k=1}^{N_{\text{CPR}}} Q\left(\sqrt{\frac{\left(\mathbb{E}\left\{U_{\text{a},k}\right\} - \mathbb{E}\left\{U_{\text{b},k}\right\}\right)^2}{\mathbb{V}\{U_{\text{a},k}\} - 2\text{Cov}\left\{U_{\text{a},k}, U_{\text{b},k}\right\} + \mathbb{V}\{U_{\text{b},k}\}}}\right)\,. \tag{5.83}$$

In the above derivation we have approximated two power sums of correlated normal RVs as two, possibly correlated, log-normal RVs ($U_{\mathrm{a},k}$ and $U_{\mathrm{b},k}$). The next step is to determine expressions for the parameters of $U_{\mathrm{a},k}$ and $U_{\mathrm{b},k}$. Two well-known methods for approximating power sums of normal RVs as a single log-normal RV are the Fenton-Wilkinson method [106] and the Schwartz-Yeh method [107], both of which were originally formulated for independent RVs. These methods will be described briefly along with our proposed solution below. The soundness of the approximation will be evaluated by comparing results of the infinite ensemble case with those of the approximation based on a finite set of channels drawn from the distribution described in Sec. 5.1.1. There are several other approximation methods in the literature which are based on the joint characteristic function (CF) of several log-normal RVs [108, 109], but evaluation of these methods can become too complex when N_{CPR} is large.

The Fenton-Wilkinson method makes the assumption that the sum of two or more log-normal RVs is well approximated, to a first order, by a single log-normal RV. The method works by matching two moments of the sum of log-normal RVs to a single RV. Here we will specifically consider matching the first and second moments. As discussed in [106] matching the first and second moments will give a resulting distribution that is a best approximation to the sum in the middle range of the RV. Matching higher moments can give better approximations for higher ranges of the RV. Since the moments and joint moments of log-normal RVs are easily calculated, the Fenton-Wilkinson can be extended to handle the case where the underlying Gaussian RVs are correlated. The expressions used are given in Appendix D.

The Schwartz-Yeh method also makes the assumption that the sum of two or more log-normal RVs can be approximated by a single log-normal RV [107, 110]. Based on exact formulae for the mean and variance of the sum of two log-normal RVs, the method uses a recursive procedure to approximate the mean and variance of a sum of log-normal RVs. This method was later extended for the case of power sums of correlated normal RVs [110]. The interested reader is directed to [110] for the complete details of this method, which we omit for brevity. In our case, we have two power sums of correlated components, so we apply the Schwartz-Yeh method twice. Computing exact expressions for the correlation between the resulting two components is difficult, so as a further approximation we set $\mathrm{Cov}\left\{U_{\mathrm{a},k}, U_{\mathrm{b},k}\right\} = 0$.

An alternate method of approximating the sums in (5.81) and (5.82) can be derived by first noting that the sums consist of log-normal RVs with different means and variances. Furthermore, the differences of the means and variances increase as a function of the SNR. In the sum (5.81) the exponential with the largest sample of $V_{k,i}$ will dominate and the dominant sample $V_{k,i}$ will likely be the one from $\{V_{k,i}\}_{i=1}^{N_{\mathrm{CPR}}}$ with the largest mean. This fact was also discussed in [108], where it was noted that the CF for log-normal sums with differing means tends toward the CF of the dominant RV. A similar statement can be made for (5.82) and $W_{k,i}$. Therefore, a simple and computationally inexpensive way to approximate (5.74) is to choose $U_{\mathrm{a},k} = V_{k,m}$ and $U_{\mathrm{b},k} = W_{k,n}$ where $m = \arg\max_i \mathbb{E}\{V_{k,i}\}$ and $n = \arg\max_i \mathbb{E}\{W_{k,i}\}$. We refer to this method as the *maximum-mean* method. A similar approach was taken to the problem of decision fusion in sensor networks [111]. The covariance between the numerator and denominator, $U_{\mathrm{a},k}$ and $U_{\mathrm{b},k}$, could then be approximated as $\mathrm{Cov}\{U_{\mathrm{a},k}, U_{\mathrm{b},k}\} = \mathrm{Cov}\{V_{k,m}, W_{k,n}\}$. Based on our empirical results, we found that this value for $\mathrm{Cov}\{U_{\mathrm{a},k}, U_{\mathrm{b},k}\}$ was not accurate and a better approximation was achieved by using $\mathrm{Cov}\{U_{\mathrm{a},k}, U_{\mathrm{b},k}\} = 0$. The results of these approximations will be discussed and illustrated in the numerical results section.

5.6 Numerical Results

In this section, numerical illustrations of the results in previous sections are provided. In particular, the focus is on the averaging bound described in Sec. 5.5. For the case of an infinite ensemble of channel realizations, a bandpass RRC pulse with center frequency $f_{\mathrm{c}} = 4\,\mathrm{GHz}$, roll-off $\nu = 0.6$, $\tau_p = 1\,\mathrm{ns}$ is considered. For the finite ensemble ensemble case a bandpass RRC pulse with roll-off $\nu = 0.6$ is used. In this case the center frequency and τ_p are set appropriately for the channel under consideration.

5.6.1 Infinite Ensemble of Channel Realizations

In Figs. 5-3–5-5, the CRB and the ZZB on the RMSE are plotted as a function of the SNR for uniform PDP ($\Gamma_l = 1/L$ for each l) in different multipath conditions assuming the receiver has a priori statistical knowledge of the CPR. The CRBs for the channel models of interest are generated by evaluating (5.57), while the ZZBs are evaluated using (5.21) in conjunction with (5.65) and (5.70).

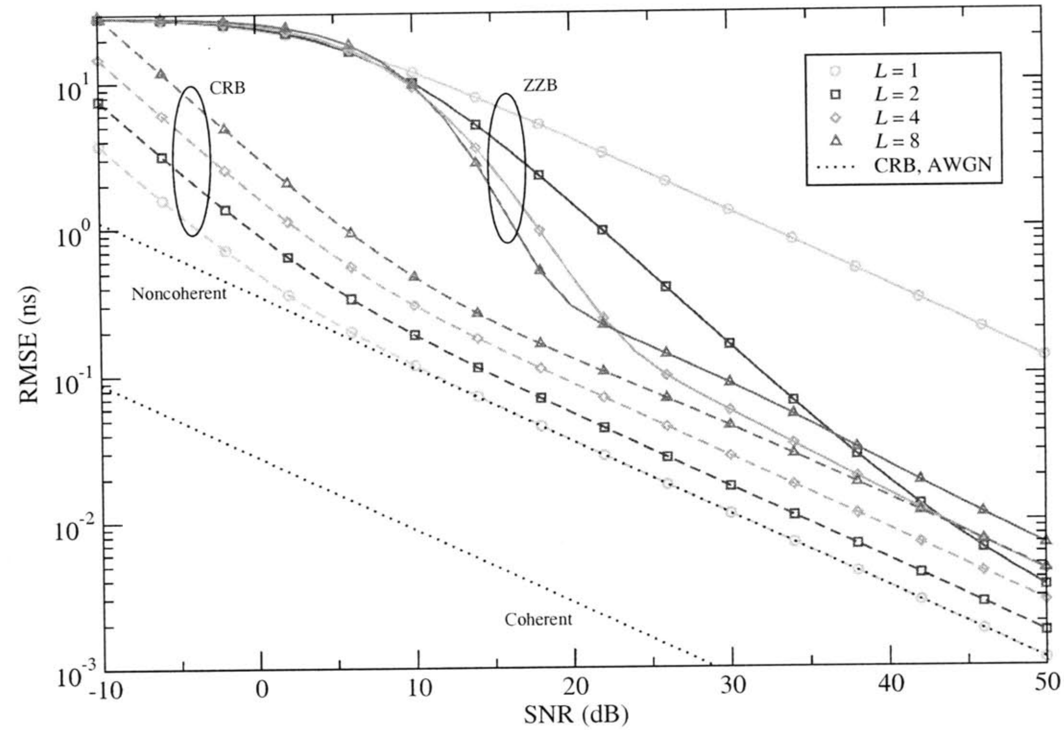

Figure 5-3: ZZB and CRB on the RMSE, using the averaging bounding approach, as a function of SNR for the Rayleigh fading channel model with $L = 1, 2, 4, 8$. The CRB is also shown for coherent and noncoherent detection in AWGN.

Fig. 5-3 illustrates the performance for Rayleigh fading channels with $L = 1, 2, 4$, and 8 paths. The curves for the CRB indicate that the performance is worse than that of the noncoherent AWGN case. This is to be expected since the CRB curves given by (5.57) incorporate the effect of both the random amplitude and phase of the paths. The performance degradation of the CRB apparent for larger values of L can be attributed to the fact that pulse overlap becomes more significant and the power (i.e., variance) of the individual path amplitudes decreases as L is increased for a uniform PDP. The figure also clearly shows that the performance of the ZZB for Rayleigh fading, as expected, is not better than that of the CRB for the noncoherent AWGN case. For larger numbers of paths L, the ZZB decreases more quickly from the a priori region (at low SNRs). However, at high SNRs larger L does not always yield better performance. As discussed earlier, under a uniform PDP larger L means that each path will have reduced energy, ultimately leading to a performance degradation at high SNR. At moderate SNRs it is sometimes possible that larger values of L can yield better performance because the increased dispersion of the CPR improves the likelihood that the estimated TOA is close to the true TOA.

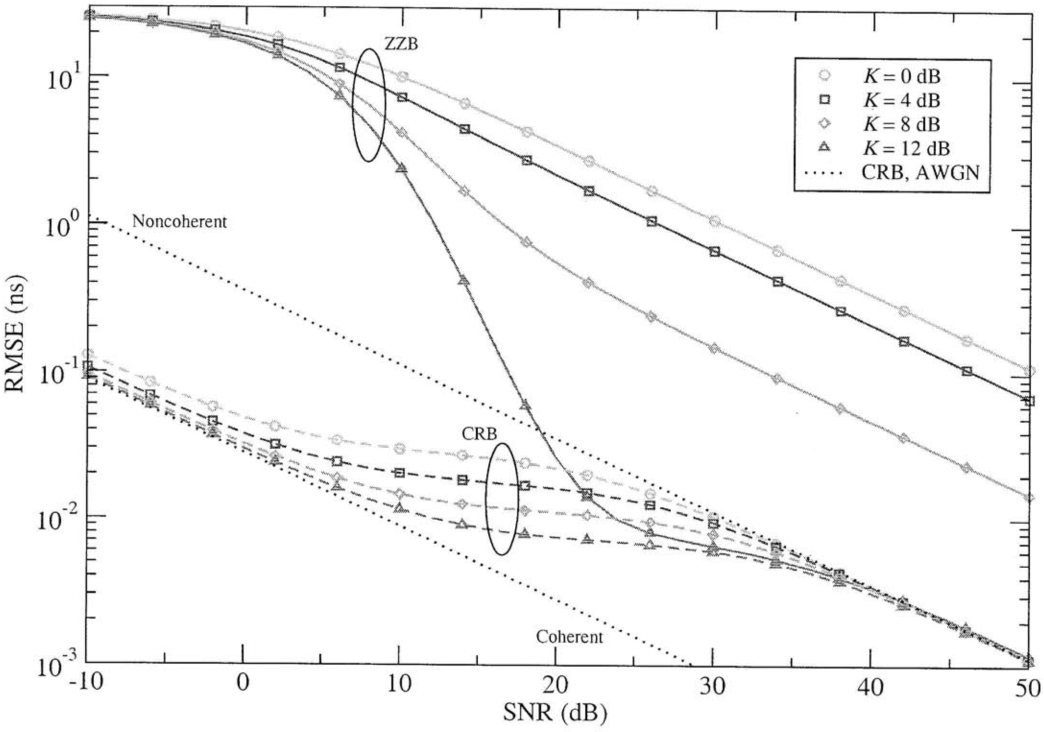

Figure 5-4: ZZB and CRB, using the averaging bounding approach, on the RMSE as a function of SNR for the Rice/Rayleigh channel model with $L = 1$ and $K = 0, 4, 8, 12$ dB. In this channel model the first path is Ricean distributed and the remaining paths are Rayleigh distributed. The CRB is also shown for coherent and noncoherent detection in AWGN.

To illustrate the effect of the specular component in the path gains on the RMSE we first investigate the single path case. Fig. 5-4 shows the CRB and ZZB on the RMSE for the case of a single path Ricean channel, as described in Sec. 5.1.1, for various values of Rice factor, $K = 0, 4, 8, 12$ dB. The figure indicates that the CRB transitions from the coherent AWGN bound for low SNRs to the noncoherent AWGN bound at high SNRs. The figure also indicates that for larger values of K the ZZB decreases more quickly from the a priori region toward the associated CRB. This occurs because larger K means that there is a reduced amount of fading in the single path channel, which in turn improves the accuracy of TOA estimation. However, convergence of the ZZB to the CRB only appears to occur for sufficiently large values of K. Depending on the value of K, the ZZB decreases below the CRB for noncoherent receivers operating in AWGN. In fact, for $K = 12$ dB we see that this is the case for SNRs greater than approximately 20 dB.

Fig. 5-5 considers channels where the first path is affected by Ricean fading and the remaining paths experience Rayleigh fading. Here we consider a Rice factor of $K = 10$ dB.

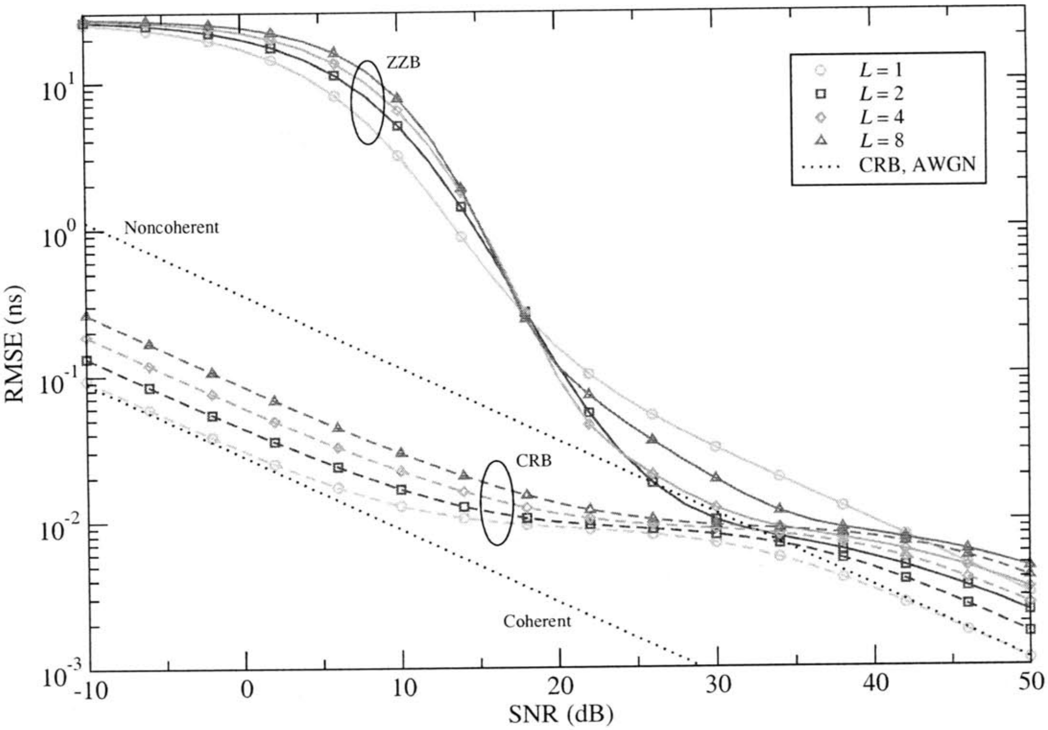

Figure 5-5: ZZB and CRB, using the averaging bounding approach, on the RMSE as a function of SNR for the Rice/Rayleigh channel model. Rice factor $K = 10\,\text{dB}$ is considered with $L = 1, 2, 4, 8$. The CRB is also shown for coherent and noncoherent detection in AWGN.

Compared to the purely Rayleigh fading case (Fig. 5-3), the effect of L is less pronounced. This is possibly due to the presence of a specular component in the first path which, regardless of the number of paths, causes the ZZB to decrease more rapidly. However, we note that larger L causes the ZZB to converge more closely to the associated CRB at high SNRs. Again, we see that larger values of L do not always imply improved performance for all values of SNR. For example, at $\mathsf{SNR} = 25\,\text{dB}$ the performance for $L = 8$ is better than $L = 1$, but worse than $L = 2$ and $L = 4$. This can be attributed to the differences in the individual path powers and the dispersion of the CPRs.

Nakagami-m fading, which has been extensively adopted to characterize UWB channels, is often well approximated as a Ricean distribution with a suitable mapping of parameters. Given the Nakagami parameters $m \geq 1$ and Γ, the Rice parameters $K = s^2/(2\sigma^2)$ (the power ratio between the specular and the scattered signals) and σ can be evaluated through the following relationships [93]

$$K = \frac{\sqrt{m^2 - m}}{m - \sqrt{m^2 - m}} \tag{5.84}$$

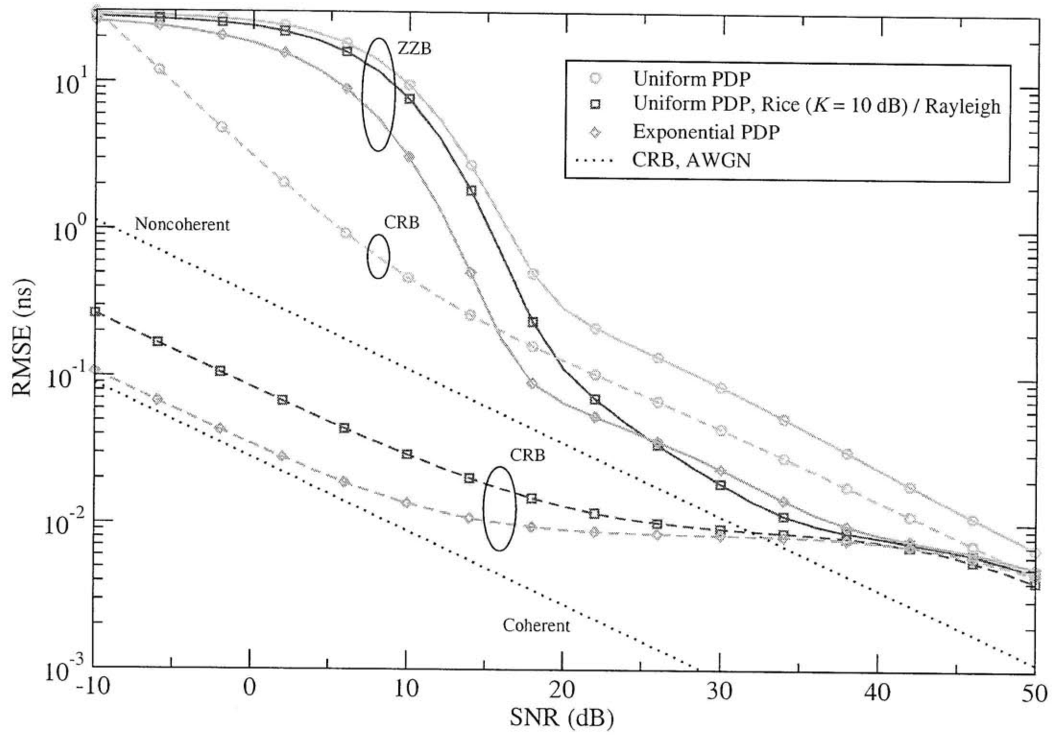

Figure 5-6: ZZB and CRB, using the averaging bounding approach, on the RMSE as a function of SNR for different power delay profiles and channel models with $L = 8$. The CRB is also shown for coherent and noncoherent detection in AWGN. The channel models considered are: 1) uniform PDP with Rayleigh distributed paths, 2) uniform PDP with the first path Rice distributed ($K = 10\,\text{dB}$) and the remaining paths Rayleigh distributed, and 3) exponential PDP with Rice distributed paths according to (5.86).

$$\sigma^2 = \frac{\Gamma}{2\,(K+1)}\,. \tag{5.85}$$

In Fig. 5-6 we consider a multipath channel with exponential PDP with average path power gains given by

$$\Gamma_l = \frac{(e^{\Delta/\varepsilon_\Gamma} - 1)e^{-\Delta(l-1)/\varepsilon_\Gamma}}{e^{\Delta/\varepsilon_\Gamma}(1 - e^{-L\Delta/\varepsilon_\Gamma})} \tag{5.86}$$

and Nakagami severity parameter $m_l = m_1\, e^{-(l-1)/\varepsilon_\text{m}}$ for $l = 1, 2, ..., L$ [6, 69, 102] using the Nagagami-m fading approximation outlined above. The parameter ε_Γ describes the multipath spread of the channel. We consider $L = 8$, $\varepsilon_\Gamma = 6$ ns, $\varepsilon_\text{m} = 4$, and $m_1 = 3$. The comparison between different channel models is reported in Fig. 5-6 for the case of 1) uniform PDP with Rayleigh fading, 2) uniform PDP with the first path Rice distributed and the remaining paths experiencing Rayleigh fading, and 3) the exponential PDP given in (5.86). The best performance is given by the exponential PDP for low to moderate SNRs. For higher SNRs the exponential PDP and uniform PDP with Rice/Rayleigh fading provide

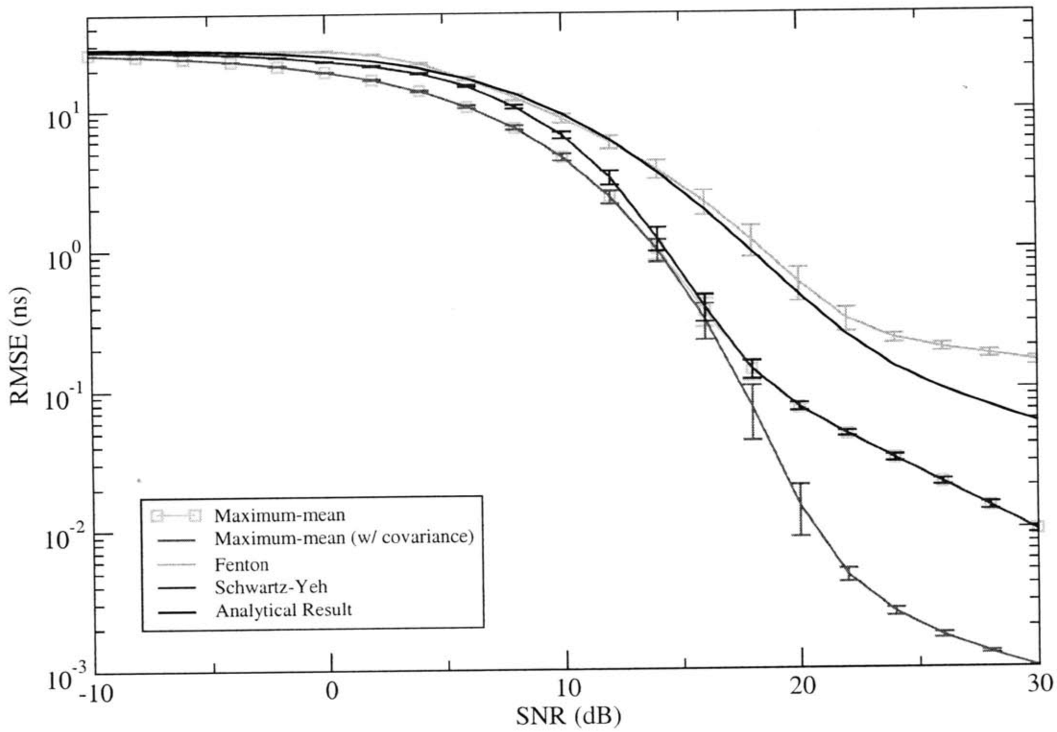

Figure 5-7: ZZB on the RMSE calculated using the various approximation methods described in 5.5.2 for the Rayleigh fading channel model with $L = 4$ paths. The Schwartz-Yeh method and the maximum-mean method have nearly identical performance.

similar performance that is better than the uniform PDP Rayleigh fading case.

5.6.2 Finite Ensemble of Channel Realizations

Figs. 5-7 and 5-8 show the various approximations, as described in Sec. 5.5.2, for the ZZB on the TOA estimation error for the case of a finite ensemble of channel realizations. The figures consider the case of Rayleigh and Ricean fading channels, respectively, with $L = 4$ paths. The set of channel realizations are produced according to the model described in Sec. 5.1.1 by first generating the random channel parameters $\boldsymbol{v}$ and using using (5.13). The analytical results (solid black curves) are evaluated using (5.21) in conjunction with (5.65) and (5.70). Each figure also reports the performance of the approximation methods described above. In each case, the method is applied to 25 sets of $N_{\mathrm{CPR}} = 25$ channels, and the curves reported are the mean of the results accompanied by the 95% confidence intervals. The results indicate that the maximum-mean method (by neglecting the correlation between the numerator and denominator) performed as well as the Schwartz-Yeh method for moderate and high SNRs. For low SNRs, the Schwartz-Yeh method was closer to the analytical curves.

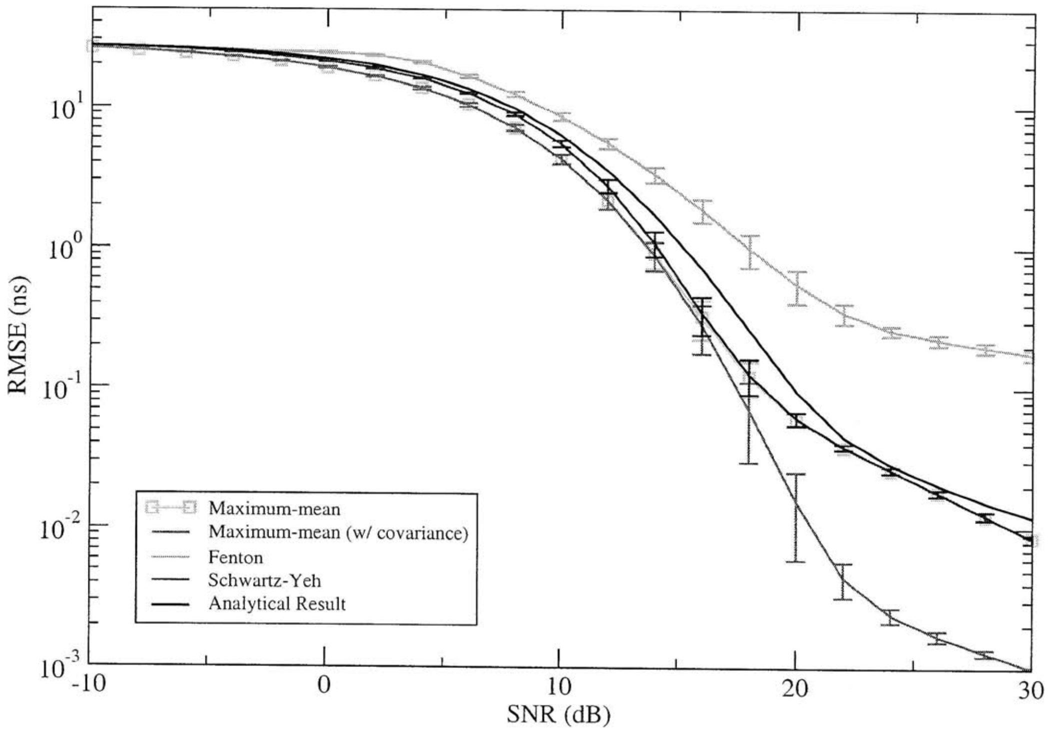

Figure 5-8: ZZB on the RMSE calculated using the various approximation methods described in 5.5.2 for the Rice/Ricean channel model with $L = 4$ paths and $K = 10\,\text{dB}$. The Schwartz-Yeh method and the maximum-mean method have nearly identical performance. We can see that the maximum-mean method provides a good approximation when there is a specular component.

In Rayleigh fading, the Fenton-Wilkinson method provided results that were the closest to the analytical curves. However, in Ricean fading the Fenton-Wilkinson method performed much worse than the maximum-mean method, especially at moderate and high SNRs. This is possibly due to the fact that this method becomes more inaccurate as the variance of the underlying Gaussian RVs becomes large. Interestingly, incorporating the covariance in the maximum-mean method, as described in Sec. 5.5.2, caused degradation in the accuracy of the approximation. This is likely due to the fact that the covariance of the two sums is not close to the covariance of the dominating components from each sum.

We now demonstrate application of the ZZB for finite ensembles of CPRs extracted from measured channel responses. In this case, the channel parameter extraction method described in Sec. 3.4.3 is utilized. This method employs the search-subtract-readjust algorithm to produce an estimate of the delays and gains of the multipath components. Using

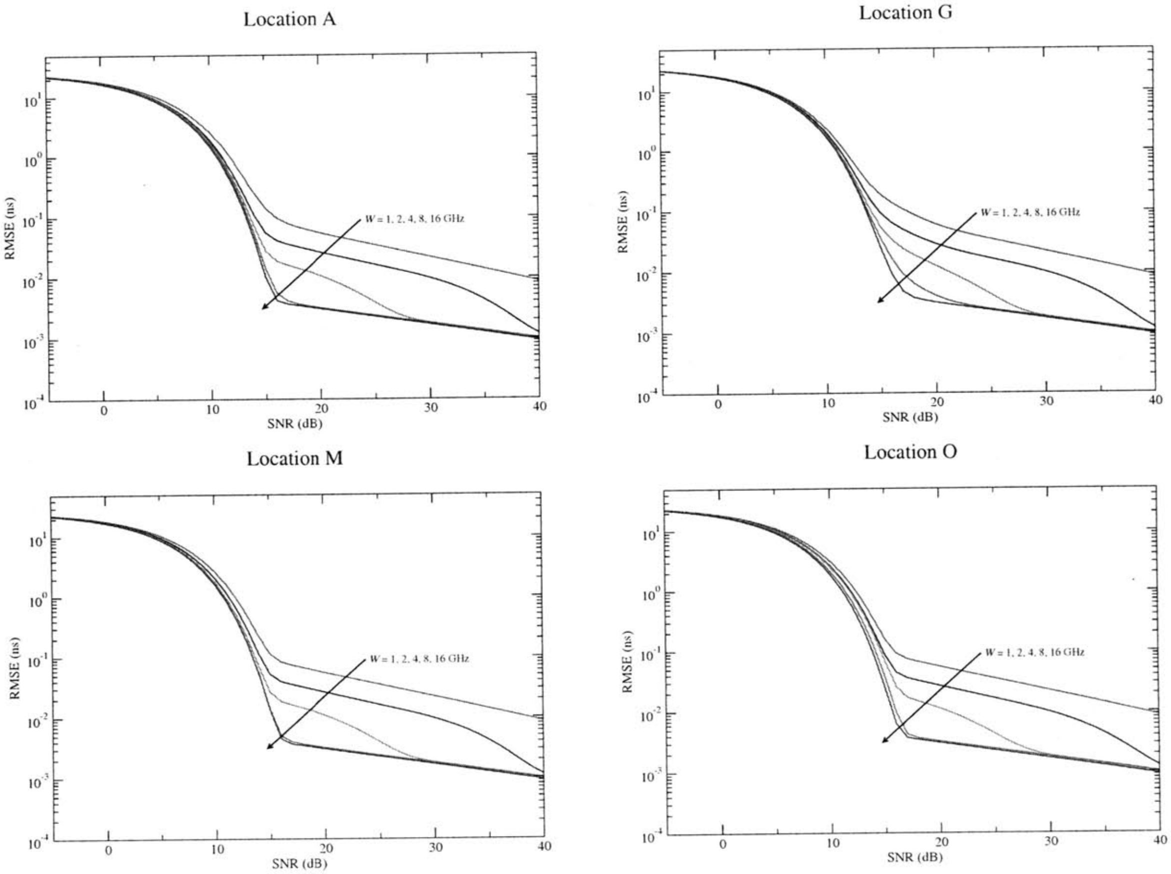

Figure 5-9: ZZB on the RMSE as a function of SNR for locations A, G, O, and M with $T_{\mathrm{a}} = 100\,\mathrm{ns}$ and $f_{\mathrm{c}} = 10\,\mathrm{GHz}$. Bandpass RRC pulses with $\nu = 0.6$ at various bandwidths are considered.

the output of the algorithm, the synthesized channel response is given by:

$$s^{(k)}(t) = \sum_{l=1}^{N^{(k)}} \Re\Big\{ \hat{h}_l^{(k)} g\big(t - \hat{\tau}_l^{(k)} - \hat{\tau}_{\mathrm{min}}^{(k)}\big) \exp\left(\jmath 2\pi f_{\mathrm{c}} t\right) \Big\} \,, \tag{5.87}$$

where $\hat{\tau}^{(k)}$ and $\hat{h}^{(k)}$ are the delays and gains extracted from the kth measured channel response after conversion to baseband. The quantity $\hat{\tau}_{\mathrm{min}}^{(k)}$ is the delay of the first arriving path and is equal to $\min_l \hat{\tau}_l^{(k)}$. Subtracting this delay from all paths has the effect of aligning the responses in the time domain and enables them to be used in the framework of Sec. 5.5.2. For each measurement location, the ZZB was computed using the averaging bound approach on a set of 188 waveforms from the main measurement grid at various bandwidths. Here, we specifically consider bandwidths $W = 1, 2, \ldots, 16\,\mathrm{GHz}$ at a fixed center frequency of $f_{\mathrm{c}} = 10\,\mathrm{GHz}$, corresponding to the set $\mathcal{S}_{\mathrm{s}}\{f_{\mathrm{c}} = 10\}$, and four representative measurement locations: A, G, M, and O. Locations A and G are both LOS, with G short range and A long range. Locations M and O are NLOS, with M short range and O long range.

Fig. 5-9 depicts the ZZB for the four representative locations for bandwidths $W = 1, 2, 4, 8$, and 16. The curves clearly show the a priori region, where the ZZB is dominated by the initial distribution of the TOA. At high SNR, the curves tend toward a common limit. The four sets of results are in very close agreement with each other, with only very subtle differences. In each case we note that increased bandwidth reduces the RMSE. In particular it can be seen that the ambiguity region begins to vanish as the bandwidth is increased. To investigate this behavior, Fig. 5-10 shows the ZZB as a function of bandwidth for three fixed SNRs of 10, 20, and 30 dB. At an SNR of 10 dB the ZZB is nearly constant with only slight variations for all bandwidths. At SNRs of 20 and 30 dB there a more significant variations as a function of bandwidth. For 20 dB, the ZZB becomes constant after about 8 GHz bandwidth, while at 30 dB the ZZB becomes constant after 4 GHz. This figure further shows that there are only minor differences in the behavior of the bounds for channel realizations collected in different locations. The most significant of these difference is for location G at an SNR of 20 dB where the ZZB is slightly above the ZZB for the other three locations.

5.7 Conclusion

In this chapter, analytical expressions for the CRB and ZZB on TOA estimation error for wideband and UWB ranging systems operating in realistic multipath environments were developed under different a priori knowledge of the multipath phenomena. The cases of both uncountably infinite and finite CPR ensembles were considered. The finite ensemble case is particularly useful to evaluate the bounds when only measured channel responses are available.

In the infinite ensemble case, it was shown that for practical SNR values, the classical CRB gives results which are too optimistic and it is not able to properly account for the effect of multipath. On the other hand, the ZZB provides improved bounds. For coherent systems operating in tapped-delay line channels with Rayleigh or Ricean fading, the bounds on the RMSE tended toward the CRB for the noncoherent case at high SNRs. In the finite ensemble case, the ZZB expressions were evaluated using captured channel response from

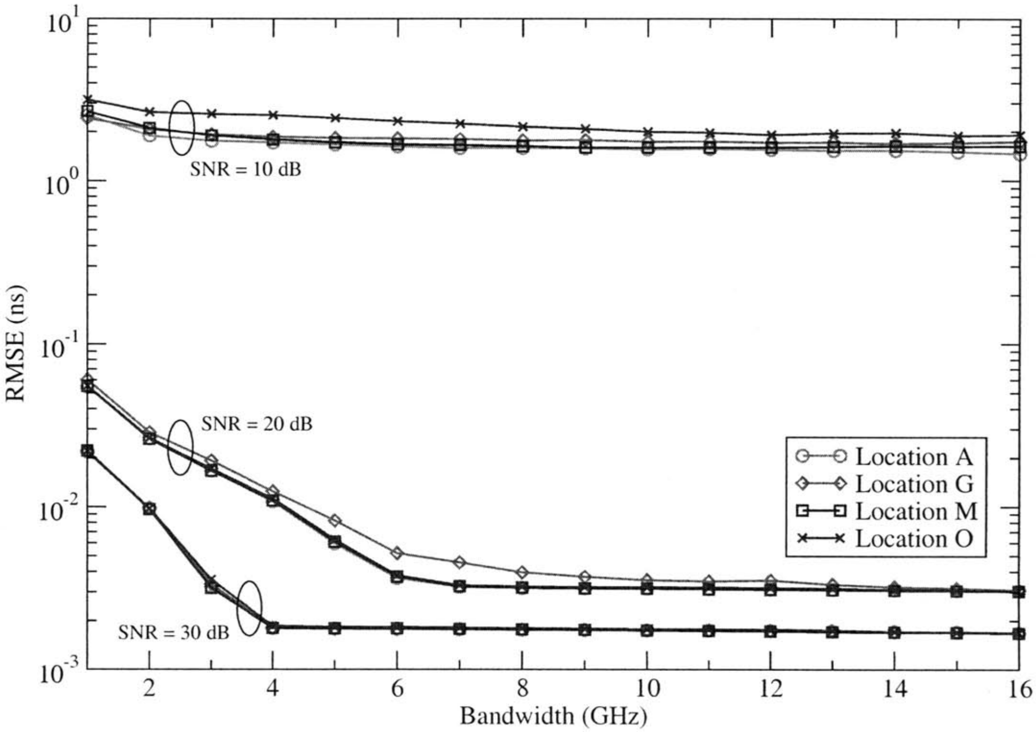

Figure 5-10: ZZB on the RMSE as a function of bandwidth for locations A, G, O, and M with $T_{\mathrm{a}} = 100\,\mathrm{ns}$ and $f_{\mathrm{c}} = 10\,\mathrm{GHz}$. Bandpass RRC pulses with $\nu = 0.6$ at 10, 20, and 30 dB SNR are considered.

four representative locations at a variety of bandwidths. These results showed behavior that was similar to the infinite ensemble case. The results also indicate the presence of an ambiguity region in the ZZB, which vanishes as the bandwidth is increased. For bandwidths above approximately 8 GHz, results were nearly identical.

The analysis of ZZB in the presence of multipath has shown how any amount of a priori knowledge about the CPR can provide more accurate lower bounds on the MSE of TOA estimation, especially in realistic environments where there is rich multipath.

Chapter 6

Conclusion

This thesis focused on the behavior of wireless systems as a function of bandwidth and center frequency. The analysis utilized data collected with a custom designed and built channel measurement apparatus. The apparatus can accurately characterize wideband channels over a frequency range of 2–18 GHz, more than double the bandwidth of conventional UWB systems, and allows for the investigation of the effects of bandwidth at ranges beyond those currently available in the literature. This chapter reviews the results based on the measurement data and discusses how they differ from those in the literature.

6.1 Wideband Diversity Systems

The first part of the thesis dealt with wideband diversity systems, where diversity arises as multipath components in the channel response. A framework for evaluating the SEP for non-ideal RSSD systems operating in a variety of multipath channels was developed. In particular, two cases were considered: 1) a WSSUS channel model, where the magnitude of the channel gains are Rayleigh distributed, and 2) the case where only a set of channel realizations, measured in a realistic environment, are available. The system studied was non-ideal, that is, the channel gains were estimated using the transmission of pilot symbols. The SEP expressions, in the case where only a set of channel realizations are available, are semi-analytical in nature. That is, they make use of Monte-Carlo averaging of exact conditional expressions. Comparisons between exact results for the Rayleigh fading case and the semi-analytical expressions showed excellent agreement.

Using the framework that was developed, the SEP performance based on measurements from four representative locations in the measurement environment was investigated. The numerical results showed that as bandwidth is increased the channel responses contain more multipath components. The increase was nonlinear; the number of paths increased with bandwidth but became saturated. This is in contrast to models which assume a linear increase as a function of bandwidth [28, 29, 112]. The fact that the number of multipath components saturates agrees with intuition. Since the multipath components are due to reflections off scatterers in the environment, at some bandwidth additional multipath components should no longer be resolved because there are a finite number of scatterers present.

Results also indicated that there are significant differences in the mean path energy capture under different propagation conditions. In particular, in LOS conditions the SEP curves were much closer for different L_d, while in NLOS conditions the SEP curves were much more spread. This provides interesting insights into the design of diversity receivers. If a system will be operating in a NLOS environment, the receiver should use several correlators, since additional combined paths significantly improves performance. On the other hand, in LOS environments, receivers should only use a few correlators, since good performance can be achieved with only a few combined paths.

Finally, numerical results indicated that, based on the measurement data considered, 1 GHz bandwidth provides the best performance. As discussed, this was due to the fact that at 1 GHz the multipath components contained significantly more energy than those at higher bandwidths.

6.2 TOA Estimation Error Bounds

The second part of the thesis investigated lower bounds on TOA estimation. Analytical expressions for the CRB and ZZB on TOA estimation error for wideband ranging systems operating in realistic multipath environments were developed under different a priori knowledge of the multipath phenomena. The cases of both uncountably infinite and finite CPR ensembles were considered. The expression for the uncountably infinite case is applicable when a statistical description of the channel is available, while the expression for the finite ensemble case is applicable when a set of measured channel responses are available.

The ZZB was evaluated for measurements at bandwidths $W = 1, 2, \ldots, 16$ GHz and a fixed center frequency of 10 GHz for four representative measurement locations. The results showed behavior that was very similar to the infinite ensemble case. In particular the ZZB curves clearly showed the a priori and asymptotic regions. The curves also indicated the presence of an ambiguity region in the ZZB, which vanished for increasing bandwidths. For bandwidths above approximately 8 GHz, the results were nearly identical.

6.3 Future Work

The data collected as part of this thesis offers many possibilities for future analyses. In particular, the following areas are of interest:

- Understanding the impact of spatial correlation. The multiscale measurement grid, as described in Chap. 3, contains several grids with different spacings. In this thesis, the analysis focused on the main grid, where all elements were considered to be uncorrelated. The data collected on the multiscale grid, particularly the center and corner sub-grids, facilitates the future analysis of system and channel parameters over finer spacings. For example, understanding how received waveforms are correlated over such finer spacings has implications for the design of physical-layer security systems, as well as ranging systems.
- Parameterization of the number of significant multipath components. The behavior of the number of significant multipath components was discussed in Chap. 4. Data from the four representative locations indicates a similar trend; the number of multipath components increases nonlinearly with bandwidth and becomes saturated. Future work in this area is to model this phenomenon and report the parameters of the model for all measured locations.
- Investigation of the role of center frequency on the ZZB. Results in Chap. 5 were given for a fixed center frequency of 10 GHz, which provides the most variation of bandwidth for the data collected with the measurement apparatus. The measurement data can also be analyzed for different center frequencies to better understand the role center frequency plays in ranging systems.

These are just a few areas of interest; the hope is that the wealth of data collected with the channel measurement apparatus will support a variety of future investigations.

Appendix A

Distribution of the Decision Variable for the Case of NSNC in Rayleigh Fading

This appendix investigates the distribution of the decison variable for the case of NSNC in Rayleigh fading. In particular, it shows that D, given by (4.12), conditioned on $\mathcal{S}_{\mathrm{N}}$ is a nonzero mean, circularly symmetric complex Gaussian r.v.

Proof. To facilitate analysis, D may be rewritten as

$$D = \sum_{k:\, k \in \mathcal{O}_{\mathrm{N}}} d_k \,, \tag{A.1}$$

where we have defined the auxiliary variables

$$d_k \triangleq \hat{h}_k^* \left[\left(\hat{h}_k - e_k \right) s_i + n_k \right] .$$

Expanding d_k gives

$$\begin{aligned} d_k = s_i \left| \hat{h}_k \right|^2 &+ \left[\hat{h}_{k,\mathrm{r}} n_{k,\mathrm{r}} + \hat{h}_{k,\mathrm{i}} n_{k,\mathrm{i}} \right] + \jmath \left[\hat{h}_{k,\mathrm{r}} n_{k,\mathrm{i}} - \hat{h}_{k,\mathrm{i}} n_{k,\mathrm{r}} \right] \\ &- s_i \left[\hat{h}_{k,\mathrm{r}} e_{k,\mathrm{r}} + \hat{h}_{k,\mathrm{i}} e_{k,\mathrm{i}} \right] + \jmath s_i \left[\hat{h}_{k,\mathrm{i}} e_{k,\mathrm{r}} - \hat{h}_{k,\mathrm{r}} e_{k,\mathrm{i}} \right] \end{aligned} \tag{A.2}$$

where the subscripts $(\cdot)_{k,\mathrm{r}}$, $(\cdot)_{k,\mathrm{i}}$ indicate the real and imaginary parts of the kth term, respectively.

Since each d_k depends on the channel only through $\hat{h}_k$, conditioning D on the set $\mathcal{S}_{\mathrm{N}}$ is equivalent to conditioning each d_k (for $k \in \mathcal{O}_{\mathrm{N}}$) on the particular $\hat{h}_k$ on which it depends. Thus, we proceed by examining the conditional distributions of the real and imaginary parts of each d_k, when conditioned on $\hat{h}_k$. From (A.2) we have,

$$\begin{aligned}
\Re\{d_k\} = s_{i,\mathrm{r}}\left|\hat{h}_k\right|^2 &+ \left[\hat{h}_{k,\mathrm{r}}n_{k,\mathrm{r}} + \hat{h}_{k,\mathrm{i}}n_{k,\mathrm{i}}\right] \\
&- \left[s_{i,\mathrm{r}}\hat{h}_{k,\mathrm{r}} + s_{i,\mathrm{i}}\hat{h}_{k,\mathrm{i}}\right] e_{k,\mathrm{r}} \\
&- \left[s_{i,\mathrm{r}}\hat{h}_{k,\mathrm{i}} - s_{i,\mathrm{i}}\hat{h}_{k,\mathrm{r}}\right] e_{k,\mathrm{i}} \qquad \text{(A.3)} \\
\Im\{d_k\} = s_{i,\mathrm{i}}\left|\hat{h}_k\right|^2 &+ \left[\hat{h}_{k,\mathrm{r}}n_{k,\mathrm{i}} - \hat{h}_{k,\mathrm{i}}n_{k,\mathrm{r}}\right] \\
&+ \left[s_{i,\mathrm{r}}\hat{h}_{k,\mathrm{i}} - s_{i,\mathrm{i}}\hat{h}_{k,\mathrm{r}}\right] e_{k,\mathrm{r}} \\
&- \left[s_{i,\mathrm{r}}\hat{h}_{k,\mathrm{r}} + s_{i,\mathrm{i}}\hat{h}_{k,\mathrm{i}}\right] e_{k,\mathrm{i}} \qquad \text{(A.4)}
\end{aligned}$$

The first term in (A.3), conditioned on $\hat{h}_k$, is a constant. The second term is distributed as a zero mean Gaussian r.v. with variance $(N_0/2)|\hat{h}_k|^2$. For the third and fourth terms, we first need to find the conditional distribution of $e_{k,\mathrm{r}}$ and $e_{k,\mathrm{i}}$ given $\hat{h}_k$. Using Bayes' rule we have

$$\begin{aligned}
f_{e_{\mathrm{i}}|\hat{h}_{\mathrm{i}}}(x|y) = f_{e_{\mathrm{r}}|\hat{h}_{\mathrm{r}}}(x|y) &= \frac{f_{\hat{h}_{\mathrm{r}}|e_{\mathrm{r}}}(y|x)f_{e_{\mathrm{r}}}(x)}{f_{\hat{h}_{\mathrm{r}}}(y)} \\
&= \frac{\frac{1}{\sqrt{2\pi\sigma_h^2}}\exp\left\{-\frac{(y-x)^2}{2\sigma_h^2}\right\}\frac{1}{\sqrt{2\pi\sigma_e^2}}\exp\left\{-\frac{x^2}{2\sigma_e^2}\right\}}{\frac{1}{\sqrt{2\pi(\sigma_h^2+\sigma_e^2)}}\exp\left\{-\frac{y^2}{2(\sigma_h^2+\sigma_e^2)}\right\}} \\
&= \frac{1}{\sqrt{2\pi}}\sqrt{\frac{\sigma_h^2+\sigma_e^2}{\sigma_h^2\sigma_e^2}}\exp\left\{-\frac{\left(x-\frac{\sigma_e^2}{\sigma_e^2+\sigma_h^2}y\right)^2}{2\frac{\sigma_h^2\sigma_e^2}{\sigma_h^2+\sigma_e^2}}\right\}. \qquad \text{(A.5)}
\end{aligned}$$

Thus, conditioned on $\hat{h}_k$, e_k is a complex Gaussian r.v. with mean $\hat{h}_k\,\sigma_e^2/(\sigma_e^2+\sigma_h^2)$ and variance per dimension $\sigma_h^2\sigma_e^2/(\sigma_h^2+\sigma_e^2)$. Using these results, we see that $\Re\{d_k\}$ is a conditionally Gaussian random variable with mean and variance given by

$$\mathbb{E}\Big\{\Re\{d_k\} \,\Big|\, \hat{h}_k\Big\} = s_{i,\mathrm{r}} \left|\hat{h}_k\right|^2 \frac{\sigma_h^2}{\sigma_e^2 + \sigma_h^2} \tag{A.6}$$

$$\mathbb{V}\Big\{\Re\{d_k\} \,\Big|\, \hat{h}_k\Big\} = \left|\hat{h}_k\right|^2 \left(\frac{N_0}{2} + |s_i|^2 \frac{\sigma_h^2 \sigma_e^2}{\sigma_h^2 + \sigma_e^2}\right) . \tag{A.7}$$

Using a similar argument it can be shown that the random variable $\Im\{d_k\}$ in (A.4) is also conditionally Gaussian with

$$\mathbb{E}\Big\{\Im\{d_k\} \,\Big|\, \hat{h}_k\Big\} = s_{i,\mathrm{i}} \left|\hat{h}_k\right|^2 \frac{\sigma_h^2}{\sigma_e^2 + \sigma_h^2} \tag{A.8}$$

$$\mathbb{V}\Big\{\Im\{d_k\} \,\Big|\, \hat{h}_k\Big\} = \left|\hat{h}_k\right|^2 \left(\frac{N_0}{2} + |s_i|^2 \frac{\sigma_h^2 \sigma_e^2}{\sigma_h^2 + \sigma_e^2}\right) . \tag{A.9}$$

Furthermore, it can be shown that

$$\mathbb{E}\Big\{\Re\{d_k\}\,\Im\{d_k\} \,\Big|\, \hat{h}_k\Big\} - \mathbb{E}\Big\{\Re\{d_k\} \,\Big|\, \hat{h}_k\Big\}\,\mathbb{E}\Big\{\Im\{d_k\} \,\Big|\, \hat{h}_k\Big\} = 0 .$$

Therefore, when conditioned on $\hat{h}_k$, $\Re\{d_k\}$ and $\Im\{d_k\}$ are uncorrelated Gaussian r.v.'s and hence they are conditionally independent. Thus, d_k is a conditionally circularly symmetric complex Gaussian r.v. with nonzero mean. Since D is the sum of conditionally independent circulalry symmetric r.v.'s, d_k, it is also a conditionally circularly symmetric complex Gaussian r.v. with nonzero mean. □

Appendix B

Cramér Rao Bound Using the Averaging Bounding Approach

The CRB can be derived as

$$\mathsf{CRB} = \left[-\mathbb{E}\left\{ \frac{\partial^2}{\partial \tau^2} \ln \Lambda\left[r(t) | \tau \right] \right\} \right]^{-1} \tag{B.1}$$

where $\Lambda\left[r(t)|\tau\right]$ is given in this case by (5.56). We can write

$$\begin{aligned} -\mathbb{E}\left\{ \frac{\partial^2}{\partial \tau^2} \ln \Lambda\left[r(t) | \tau \right] \right\} = -4\,\mathsf{SNR}^2 \operatorname{tr}\Bigg\{ & \left(\mathbf{I}_{2L} + 2\,\mathsf{SNR}\, \boldsymbol{\Psi}_2 \mathbf{R}_2(0) \right)^{-1} \boldsymbol{\Psi}_2 \\ & \times \mathbb{E}\left\{ \ddot{\mathbf{q}}(\tau) \left(\mathbf{q}(\tau) + \frac{1}{2\,\mathsf{SNR}} \boldsymbol{\Psi}_2^{-1} \boldsymbol{\mu} \right)^T + \dot{\mathbf{q}}(\tau) \dot{\mathbf{q}}(\tau)^T \right\} \Bigg\}, \end{aligned} \tag{B.2}$$

where the elements of $\dot{\mathbf{q}}(\tau)$ and $\ddot{\mathbf{q}}(\tau)$ are given by

$$\dot{\mathsf{q}}(\tau)_k = \begin{cases} \frac{1}{E_\mathrm{p}} \int_0^{T_\mathrm{ob}} r(t) \frac{\partial}{\partial \tau} p_k^\mathrm{I}(t-\tau)\, dt & 1 \le k \le L \\ \frac{1}{E_\mathrm{p}} \int_0^{T_\mathrm{ob}} r(t) \frac{\partial}{\partial \tau} p_k^\mathrm{Q}(t-\tau)\, dt & L < k \le 2L \end{cases} \tag{B.3}$$

$$\ddot{\mathsf{q}}(\tau)_k = \begin{cases} \frac{1}{E_\mathrm{p}} \int_0^{T_\mathrm{ob}} r(t) \frac{\partial}{\partial \tau} p_k^\mathrm{I}(t-\tau)\, dt & 1 \le k \le L \\ \frac{1}{E_\mathrm{p}} \int_0^{T_\mathrm{ob}} r(t) \frac{\partial^2}{\partial \tau^2} p_k^\mathrm{Q}(t-\tau)\, dt & L < k \le 2L \end{cases} \tag{B.4}$$

It can then be shown that

$$\begin{aligned}
\mathbb{E}\left\{\ddot{\mathbf{q}}(\tau)\mathbf{q}(\tau)^T\right\} &= -\boldsymbol{\Upsilon}\left(\mathbb{E}\left\{\mathbf{v}\mathbf{v}^T\right\}\mathbf{R}_2(0) + \frac{1}{2\,\mathsf{SNR}}\mathbf{I}_{2L}\right) \\
\mathbb{E}\left\{\ddot{\mathbf{q}}(\tau)\right\} &= -\boldsymbol{\Upsilon}\boldsymbol{\mu} \\
\mathbb{E}\left\{\dot{\mathbf{q}}(\tau)\dot{\mathbf{q}}(\tau)^T\right\} &= \boldsymbol{\Xi}\mathbb{E}\left\{\mathbf{v}\mathbf{v}^T\right\}\boldsymbol{\Xi}^T + \frac{1}{2\,\mathsf{SNR}}\boldsymbol{\Upsilon}\,,
\end{aligned}$$

where

$$\boldsymbol{\Xi} = \begin{bmatrix} \mathbf{R}_{g\dot{g}} & -2\pi f_c\mathbf{R}(0) \\ 2\pi f_c\mathbf{R}(0) & \mathbf{R}_{g\dot{g}} \end{bmatrix}\,. \tag{B.5}$$

Using the above expressions, the expectation in (B.2) reduces to:

$$\begin{aligned}
&\mathbb{E}\left\{\ddot{\mathbf{q}}(\tau)\left(\mathbf{q}(\tau) + \frac{1}{2\,\mathsf{SNR}}\boldsymbol{\Psi}_2^{-1}\boldsymbol{\mu}\right)^T + \dot{\mathbf{q}}(\tau)\dot{\mathbf{q}}(\tau)^T\right\} \\
&\quad = -\boldsymbol{\Upsilon}\boldsymbol{\Psi}_2\mathbf{R}_2(0) - \boldsymbol{\Upsilon}\boldsymbol{\mu}\boldsymbol{\mu}^T\left(\mathbf{R}_2(0) + \frac{1}{2\,\mathsf{SNR}}\boldsymbol{\Psi}_2^{-1}\right) + \boldsymbol{\Xi}(\boldsymbol{\Psi}_2 + \boldsymbol{\mu}\boldsymbol{\mu}^T)\boldsymbol{\Xi}^T
\end{aligned} \tag{B.6}$$

Appendix C

Derivation of the Statistics of $\mathsf{q}^{(1)}$ and $\mathsf{q}^{(2)}$

This appendix derives the statistical properties of $\mathsf{q}^{(1)}$ and $\mathsf{q}^{(2)}$ used in the derivation of the averaging bound approach in Sec. 5.5. Under hypothesis H_1, the expressions in (5.51) imply that

$$\begin{aligned}\mathsf{q}_k^{\mathrm{I}}(\tau+z) &= \sum_{m=1}^{L} \mathsf{v}_m \rho_g(z+(k-m)\Delta\tau)\cos(2\pi f_{\mathrm{c}} z) - \mathsf{v}_{L+m}\rho_g(z+(k-m)\Delta\tau)\sin(2\pi f_{\mathrm{c}} z) \\ &\quad + n_k^{\mathrm{I}}(\tau+z) \qquad \text{(C.1)}\\ \mathsf{q}_k^{\mathrm{Q}}(\tau+z) &= \sum_{m=1}^{L} \mathsf{v}_m \rho_g(z+(k-m)\Delta\tau)\sin(2\pi f_{\mathrm{c}} z) + \mathsf{v}_{L+m}\rho_g(z+(k-m)\Delta\tau)\cos(2\pi f_{\mathrm{c}} z) \\ &\quad + n_k^{\mathrm{Q}}(\tau+z) \qquad \text{(C.2)}\end{aligned}$$

where we have assumed that the contribution of any double frequency terms are negligible. Here the noise terms are given by

$$\mathsf{n}_k^{\mathrm{I}}(\tau+z) = \frac{1}{E_{\mathrm{p}}}\int_0^{T_{\mathrm{ob}}} n(t)p_k^{\mathrm{I}}(t-\tau-z)\,dt \qquad \text{(C.3)}$$

$$\mathsf{n}_k^{\mathrm{Q}}(\tau+z) = \frac{1}{E_{\mathrm{p}}}\int_0^{T_{\mathrm{ob}}} n(t)p_k^{\mathrm{Q}}(t-\tau-z)\,dt\,. \qquad \text{(C.4)}$$

Note that $\mathsf{n}_k^I(\cdot)$ and $\mathsf{n}_k^Q(\cdot)$ are zero-mean Gaussian, but will, in general, be correlated:

$$\begin{aligned}
\mathbb{E}\left\{\mathsf{n}_k^{\mathrm{I}}(\tau+z_1)\mathsf{n}_l^{\mathrm{I}}(\tau+z_2)\right\} &= \mathbb{E}\left\{\mathsf{n}_k^{\mathrm{Q}}(\tau+z_1)\mathsf{n}_l^{\mathrm{Q}}(\tau+z_2)\right\} \\
&= \frac{1}{2\,\mathsf{SNR}}\rho_g(z_2-z_1+(l-k)\Delta\tau)\cos(2\pi f_c(z_2-z_1)) && \text{(C.5)} \\
\mathbb{E}\left\{\mathsf{n}_k^{\mathrm{I}}(\tau+z_1)\mathsf{n}_l^{\mathrm{Q}}(\tau+z_2)\right\} &= -\mathbb{E}\left\{\mathsf{n}_k^{\mathrm{Q}}(\tau+z_1)\mathsf{n}_l^{\mathrm{I}}(\tau+z_2)\right\} \\
&= \frac{1}{2\,\mathsf{SNR}}\rho_g(z_2-z_1+(l-k)\Delta\tau)\sin(2\pi f_c(z_2-z_1))\,. && \text{(C.6)}
\end{aligned}$$

Now, we can write

$$\begin{aligned}
\mathsf{q}^{(1)} &= \mathbf{R}_2(0)^T\mathsf{v}+\mathsf{n}^{(1)} && \text{(C.7)} \\
\mathsf{q}^{(2)} &= \mathbf{R}_2(z)^T\mathsf{v}+\mathsf{n}^{(2)}\,, && \text{(C.8)}
\end{aligned}$$

where

$$\begin{aligned}
\mathsf{n}^{(1)} &= \left[\mathsf{n}_1^{\mathrm{I}}(\tau),\, \mathsf{n}_2^{\mathrm{I}}(\tau),\, \ldots, \mathsf{n}_L^{\mathrm{I}}(\tau),\, \mathsf{n}_{L+1}^{\mathrm{Q}}(\tau),\, \mathsf{n}_{L+2}^{\mathrm{Q}}(\tau),\, \ldots, \mathsf{n}_{2L}^{\mathrm{Q}}(\tau)\right]^T \\
\mathsf{n}^{(2)} &= \left[\mathsf{n}_1^{\mathrm{I}}(\tau+z),\, \mathsf{n}_2^{\mathrm{I}}(\tau+z),\, \ldots, \mathsf{n}_L^{\mathrm{I}}(\tau+z),\, \mathsf{n}_{L+1}^{\mathrm{Q}}(\tau+z),\, \mathsf{n}_{L+2}^{\mathrm{Q}}(\tau+z),\, \ldots, \mathsf{n}_{2L}^{\mathrm{Q}}(\tau+z)\right]^T .
\end{aligned}$$

Under the Rayleigh/Ricean fading model of Sec. 5.1.1, v is a Gaussian random vector, therefore we conclude that $\mathsf{q}^{(1)}$ and $\mathsf{q}^{(2)}$ are jointly Gaussian random vectors. Using (C.7)–(C.8), gives

$$\begin{aligned}
\mathbb{E}\left\{\mathsf{q}^{(1)}\right\} &= \mathbf{R}_2(0)^T\boldsymbol{\mu} && \text{(C.9)} \\
\mathbb{E}\left\{\mathsf{q}^{(2)}\right\} &= \mathbf{R}_2(z)^T\boldsymbol{\mu}\,. && \text{(C.10)}
\end{aligned}$$

Similarly, using (C.5)–(C.8), the covariances between $\mathsf{q}^{(1)}$ and $\mathsf{q}^{(2)}$ can be determined as

$$\begin{aligned}
\mathrm{Cov}\left\{\mathsf{q}^{(1)},\mathsf{q}^{(1)}\right\} &= \mathbf{R}_2(0)^T\boldsymbol{\Psi}_2\mathbf{R}_2(0)+\frac{1}{2\,\mathsf{SNR}}\mathbf{R}_2(0) = \mathbf{I}_2\otimes\mathbf{A} && \text{(C.11)} \\
\mathrm{Cov}\left\{\mathsf{q}^{(1)},\mathsf{q}^{(2)}\right\} &= \mathrm{Cov}\left\{\mathsf{q}^{(2)},\mathsf{q}^{(1)}\right\}^T \\
&= \mathbf{R}_2(0)^T\boldsymbol{\Psi}_2\mathbf{R}_2(z)+\frac{1}{2\,\mathsf{SNR}}\mathbf{R}_2(z) = \boldsymbol{\Omega}(z)\otimes\mathbf{X} && \text{(C.12)} \\
\mathrm{Cov}\left\{\mathsf{q}^{(2)},\mathsf{q}^{(2)}\right\} &= \mathbf{R}_2(z)^T\boldsymbol{\Psi}_2\mathbf{R}_2(z)+\frac{1}{2\,\mathsf{SNR}}\mathbf{R}_2(0) = \mathbf{I}_2\otimes\mathbf{D}\,, && \text{(C.13)}
\end{aligned}$$

where

$$\mathbf{A} = \mathbf{R}(0)^T \boldsymbol{\Psi} \mathbf{R}(0) + \frac{1}{2\,\mathsf{SNR}} \mathbf{R}(0) \tag{C.14}$$

$$\mathbf{X} = \mathbf{R}(0)^T \boldsymbol{\Psi} \mathbf{R}(z) + \frac{1}{2\,\mathsf{SNR}} \mathbf{R}(z) \tag{C.15}$$

$$\mathbf{D} = \mathbf{R}(z)^T \boldsymbol{\Psi} \mathbf{R}(z) + \frac{1}{2\,\mathsf{SNR}} \mathbf{R}(0) \tag{C.16}$$

$$\boldsymbol{\Omega}(z) = \begin{bmatrix} \cos(2\pi f_c z) & \sin(2\pi f_c z) \\ -\sin(2\pi f_c z) & \cos(2\pi f_c z) \end{bmatrix} . \tag{C.17}$$

Using the results of (C.11)-(C.13), the covariance matrix of $\mathbf{x}$ in (5.61) can now be written as

$$\boldsymbol{\Sigma} = \mathrm{Cov}\left\{\mathbf{x}, \mathbf{x}\right\} = \begin{bmatrix} \mathbf{I}_2 \otimes \mathbf{A} & \boldsymbol{\Omega}(z) \otimes \mathbf{X} \\ \boldsymbol{\Omega}(z)^T \otimes \mathbf{X}^T & \mathbf{I}_2 \otimes \mathbf{D} \end{bmatrix} . \tag{C.18}$$

Appendix D

Fenton-Wilkinson Method

This appendix describes the Fenton-Wilkinson method, a technique to approximate the sum of log-normal RVs with a single log-normal RV [106, 113]. This derivation focuses on the case where the underlying RVs are correlated and also derives an expression for the covariance between two sums of correlated log-normal RVs.

We begin by stating a few results for log-normal random variables. If $S \sim \mathcal{N}(\mu, \sigma^2)$, then $T = \exp\{S\}$ is log-normally distributed with

$$\mathbb{E}\{T\} = \exp\{\mu + \sigma^2/2\} \tag{D.1}$$

$$\mathbb{V}\{T\} = \left(\exp\{\sigma^2\} - 1\right)\exp\{2\mu + \sigma^2\}\ . \tag{D.2}$$

If $S_1 \sim \mathcal{N}(\mu_1, \sigma_1^2)$ and $S_2 \sim \mathcal{N}(\mu_2, \sigma_2^2)$ are jointly Gaussian, with $T_1 = \exp\{S_1\}$ and $T_2 = \exp\{S_2\}$ then

$$\mathrm{Cov}\{T_1, T_2\} = \exp\left\{\mu_1 + \mu_2 + \frac{\sigma_1^2 + \sigma_2^2}{2}\right\}\left(\exp\{\mathrm{Cov}\{S_1, S_2\}\} - 1\right), \tag{D.3}$$

where we have used the fact that $S_1 + S_2 \sim \mathcal{N}(\mu_1 + \mu_2, \sigma_1^2 + \sigma_2^2 + 2\mathrm{Cov}\{S_1, S_2\})$.

Applying (D.1) and (D.2) to (5.81), we can find the desired mean and variance of

$\exp\{U_{\mathrm{a},k}\}$ as

$$\mathbb{E}\left\{\exp\{U_{\mathrm{a},k}\}\right\} = \mathbb{E}\left\{Z_{\mathrm{a},k}\right\} = \mathbb{E}\left\{\sum_{i=1}^{N_{\mathrm{CPR}}} X_{k,i}\right\} = \sum_{i} \exp\left\{\mathbb{E}\left\{V_{k,i}\right\} + \mathbb{V}\{V_{k,i}\}/2\right\}$$
$$\mathbb{V}\{\exp\{U_{\mathrm{a},k}\}\} = \mathbb{V}\{Z_{\mathrm{a},k}\} = \mathbb{V}\left\{\sum_{i=1}^{N_{\mathrm{CPR}}} X_{k,i}\right\} = \sum_{i,j} \mathrm{Cov}\left\{X_{k,i}, X_{k,j}\right\} ,$$

where the covariance can be found by using (D.3). The mean and variance of $U_{\mathrm{a},k}$ can then be found by using the relationship in (D.1) and (D.2) with $\mu = \mathbb{E}\left\{U_{\mathrm{a},k}\right\}$ and $\sigma^2 = \mathbb{V}\{U_{\mathrm{a},k}\}$:

$$\mathbb{E}\left\{U_{\mathrm{a},k}\right\} = \log\Big(\mathbb{E}\left\{Z_{\mathrm{a},k}\right\}\Big) - \frac{1}{2}\log\Big(1 + \mathbb{V}\{Z_{\mathrm{a},k}\}/\mathbb{E}\left\{Z_{\mathrm{a},k}\right\}^2\Big) \tag{D.4}$$
$$\mathbb{V}\{U_{\mathrm{a},k}\} = \log\Big(1 + \mathbb{V}\{Z_{\mathrm{a},k}\}/\mathbb{E}\left\{Z_{\mathrm{a},k}\right\}^2\Big) . \tag{D.5}$$

The statistics of $U_{\mathrm{b},k}$ can be determined in a similar way.

In general, $Z_{\mathrm{a},k}$ and $Z_{\mathrm{b},k}$ in (5.81) and (5.82) will be correlated, thus we want the approximations $U_{\mathrm{a},k}$ and $U_{\mathrm{b},k}$ to also exhibit the appropriate correlation. Using (D.3) we can express $\mathrm{Cov}\left\{U_{\mathrm{a},k}, U_{\mathrm{b},k}\right\}$ in terms of the covariance of the underlying $V_{k,i}$, $W_{k,j}$:

$$\begin{aligned}\mathrm{Cov}\left\{Z_{\mathrm{a},k}, Z_{\mathrm{b},k}\right\} &= \sum_{i,j} \mathrm{Cov}\left\{X_{k,i}, Y_{k,j}\right\} \\ &= \sum_{i,j} \Big(\exp\left\{\mathrm{Cov}\left\{V_{k,i}, W_{k,j}\right\}\right\} - 1\Big) \\ &\qquad \times \exp\left\{\mathbb{E}\left\{V_{k,i}\right\} + \mathbb{E}\left\{W_{k,j}\right\} + \frac{\mathbb{V}\{V_{k,i}\} + \mathbb{V}\{W_{k,j}\}}{2}\right\} .\end{aligned} \tag{D.6}$$

Also, from (D.3) we have

$$\mathrm{Cov}\left\{U_{\mathrm{a},k}, U_{\mathrm{b},k}\right\} = \log\left(\frac{\mathrm{Cov}\left\{Z_{\mathrm{a},k}, Z_{\mathrm{b},k}\right\}}{\mathbb{E}\left\{Z_{\mathrm{a},k}\right\}\mathbb{E}\left\{Z_{\mathrm{b},k}\right\}} + 1\right) . \tag{D.7}$$

Bibliography

[1] M. Z. Win and R. A. Scholtz, "Impulse radio: How it works," *IEEE Commun. Lett.*, vol. 2, no. 2, pp. 36–38, Feb. 1998.

[2] ——, "Ultra-wide bandwidth time-hopping spread-spectrum impulse radio for wireless multiple-access communications," *IEEE Trans. Commun.*, vol. 48, no. 4, pp. 679–691, Apr. 2000.

[3] ——, "On the robustness of ultra-wide bandwidth signals in dense multipath environments," *IEEE Commun. Lett.*, vol. 2, no. 2, pp. 51–53, Feb. 1998.

[4] ——, "On the energy capture of ultra-wide bandwidth signals in dense multipath environments," *IEEE Commun. Lett.*, vol. 2, no. 9, pp. 245–247, Sep. 1998.

[5] ——, "Characterization of ultra-wide bandwidth wireless indoor communications channel: A communication theoretic view," *IEEE J. Sel. Areas Commun.*, vol. 20, no. 9, pp. 1613–1627, Dec. 2002.

[6] D. Cassioli, M. Z. Win, and A. F. Molisch, "The ultra-wide bandwidth indoor channel: from statistical model to simulations," *IEEE J. Sel. Areas Commun.*, vol. 20, no. 6, pp. 1247–1257, Aug. 2002.

[7] R. J.-M. Cramer, R. A. Scholtz, and M. Z. Win, "An evaluation of the ultra-wideband propagation channel," *IEEE Trans. Antennas Propag.*, vol. 50, no. 5, pp. 561–570, May 2002.

[8] M. Z. Win, "Spectral density of random time-hopping spread-spectrum UWB signals," *IEEE Commun. Lett.*, vol. 6, no. 12, pp. 526–528, Dec. 2002.

[9] ——, "A unified spectral analysis of generalized time-hopping spread-spectrum signals in the presence of timing jitter," *IEEE J. Sel. Areas Commun.*, vol. 20, no. 9, pp. 1664–1676, Dec. 2002.

[10] S. S. Kolenchery, J. K. Townsend, J. A. Freebersyser, and G. Bilbro, "Performance of local power control in peer-to-peer impulse radio networks with bursty traffic," in *Proc. IEEE Global Telecomm. Conf.*, vol. 2, Phoenix, AZ, Nov. 1997, pp. 910–916.

[11] S. S. Kolenchery, J. K. Townsend, and J. A. Freebersyser, "A novel impulse radio network for tactical military wireless communications," in *Proc. Military Commun. Conf.*, vol. 1, Boston, MA, Oct. 1998, pp. 59–65.

[12] G. D. Weeks, J. K. Townsend, and J. A. Freebersyser, "Performance of hard decision detection for impulse radio," in *Proc. Military Commun. Conf.*, vol. 2, Atlantic City, NJ, Oct. 1999, pp. 1201–1206.

[13] J. Conroy, J. L. LoCicero, and D. R. Ucci, "Communication techniques using monopulse waveforms," in *Proc. Military Commun. Conf.*, vol. 2, Atlantic City, NJ, Oct. 1999, pp. 1181–1185.

[14] L. Zhao and A. M. Haimovich, "Interference suppression in ultra-wideband communications," in *Proc. Conf. on Inform. Sci. and Sys.*, vol. 2, Baltimore, MD, Mar. 2001, pp. 759–763.

[15] L. Zhao, A. M. Haimovich, and H. Grebel, "Performance of ultra-wideband communications in the presence of interference," in *Proc. IEEE Int. Conf. on Commun.*, vol. 10, Helsinki, FINLAND, Jun. 2001, pp. 2948–2952.

[16] Federal Communications Commission, "Revision of part 15 of the commission's rules regarding ultra-wideband transmission systems, first report and order (ET Docket 98-153)," Adopted Feb. 14, 2002, Released Apr. 22, 2002.

[17] C.-C. Chong and S. K. Yong, "A generic statistical-based UWB channel model for high-rise apartments," *IEEE Trans. Antennas Propag.*, vol. 53, pp. 2389–2399, 2005.

[18] R. Price and P. E. Green, Jr., "A communication technique for multipath channels," *Proc. IRE*, vol. 46, no. 3, pp. 555–570, Mar. 1958.

[19] G. Turin, "Introduction to spread-spectrum antimultipath techniques and their application to urban digital radio," *Proc. IEEE*, vol. 68, no. 3, pp. 328–353, Mar. 1980.

[20] R. L. Pickholtz, D. L. Schilling, and L. B. Milstein, "Theory of spread spectrum communications–A tutorial," *IEEE Trans. Commun.*, vol. COM-30, no. 5, pp. 855–884, May 1982.

[21] J. S. Lehnert and M. B. Pursley, "Multipath diversity reception of spread spectrum multiple-access communications," *IEEE Trans. Commun.*, vol. COM-35, no. 11, pp. 1189–1198, Nov. 1987.

[22] T. Eng and L. B. Milstein, "Coherent DS-CDMA performance in Nakagami multipath fading," *IEEE Trans. Commun.*, vol. 43, no. 2/3/4, pp. 1134–1143, Feb./Mar./Apr. 1995.

[23] J. G. Proakis, *Digital Communications*, 3rd ed. New York, NY, 10020: McGraw-Hill, Inc., 1995.

[24] R. L. Peterson, R. E. Ziemer, and D. E. Borth, *Introduction to Spread Spectrum Communications*, 1st ed. Englewood Cliffs, New Jersey 07632: Prentice Hall, 1995.

[25] M. K. Simon, J. K. Omura, R. A. Scholtz, and B. K. Levitt, *Spread Spectrum Communications Handbook*. New York, NY: McGraw-Hill, 2001.

[26] M. Z. Win and Z. A. Kostić, "Virtual path analysis of selective Rake receiver in dense multipath channels," *IEEE Commun. Lett.*, vol. 3, no. 11, pp. 308–310, Nov. 1999.

[27] ——, "Impact of spreading bandwidth on Rake reception in dense multipath channels," *IEEE J. Sel. Areas Commun.*, vol. 17, no. 10, pp. 1794–1806, Oct. 1999.

[28] M. Z. Win, G. Chrisikos, and N. R. Sollenberger, "Performance of Rake reception in dense multipath channels: Implications of spreading bandwidth and selection diversity order," *IEEE J. Sel. Areas Commun.*, vol. 18, no. 8, pp. 1516–1525, Aug. 2000.

[29] M. Z. Win and G. Chrisikos, "Impact of spreading bandwidth and selection diversity order on selective Rake reception," in *Wideband Wireless Digital Communications*, A. F. Molisch, Ed. Upper Saddle River, NJ 07458: Prentice Hall Publishers, 2001, ch. 29, pp. 424–454 and 523–525, translated into Chinese by Publishing House of Electronics Industry, Beijing, China.

[30] W. M. Gifford, M. Z. Win, and M. Chiani, "Diversity with pilot symbol assisted modulation," in *Proc. Conf. on Inform. Sci. and Sys.*, Princeton, NJ, Mar. 2004.

[31] ——, "On the SNR penalty for realistic diversity systems," in *Proc. Conf. on Inform. Sci. and Sys.*, Princeton, NJ, Mar. 2004.

[32] X. Wang and J. Wang, "Effect of imperfect channel estimation on transmit diversity in CDMA systems," *IEEE Trans. Veh. Technol.*, vol. 53, no. 5, pp. 1400–1412, Sep. 2004.

[33] W. M. Gifford, M. Z. Win, and M. Chiani, "Realistic diversity systems in correlated fading," in *Proc. IEEE Global Telecomm. Conf.*, vol. 1, Dallas, TX, Dec. 2004, pp. 457–461.

[34] B. Xia and J. Wang, "Analytical study of QAM with interference cancellation for high-speed multicode CDMA," *IEEE Trans. Veh. Technol.*, vol. 54, no. 3, pp. 1070–1080, May 2005.

[35] W. M. Gifford, M. Z. Win, and M. Chiani, "Diversity with practical channel estimation," *IEEE Trans. Wireless Commun.*, vol. 4, no. 4, pp. 1935–1947, Jul. 2005.

[36] C. Falsi, D. Dardari, L. Mucchi, and M. Z. Win, "Time of arrival estimation for UWB localizers in realistic environments," *EURASIP J. Appl. Signal Process.*, vol. 2006, pp. Article ID 32 082, 1–13, 2006, special issue on *Wireless Location Technologies and Applications*.

[37] J.-Y. Lee and R. A. Scholtz, "Ranging in a dense multipath environment using an UWB radio link," *IEEE J. Sel. Areas Commun.*, vol. 20, no. 9, pp. 1677–1683, Dec. 2002.

[38] "Agilent AN 1287-6, using a network analyzer to characterize high-power components," Agilent Technologies. [Online]. Available: \url{http://cp.literature.agilent.com/litweb/pdf/5966-3319E.pdf}

[39] "PNA help user's and programming guide," Agilent Technologies, June 2010. [Online]. Available: \url{http://na.tm.agilent.com/pna/help/index.html}

[40] "Agilent N1911A/1912A P-series power meters, user's guide," Agilent Technologies, April 2010. [Online]. Available: \url{http://cp.literature.agilent.com/litweb/pdf/N1912-90002.pdf}

[41] "SLO-SYN WARPDRIVE SS2000D6i/D3i programmable step motor controller installation and operating instructions," Danaher Motion, Jan. 2003. [Online]. Available: \url{http://www.kollmorgen.com/website/com/eng/download/document/400030106_71841_snapshot.pdf}

[42] A. F. Molisch, *Wireless Communications*, 1st ed. Piscataway, New Jersey, 08855-1331: IEEE Press, J. Wiley and Sons, 2005.

[43] A. V. Oppenheim and A. S. Willsky, *Signals and Systems*, 2nd ed. Prentice Hall, 1997.

[44] A. N. Shiryaev, *Probability*, 2nd ed. New York, NY: Springer-Verlag, 1995.

[45] R. Durrett, *Probability: Theory and Examples*, 1st ed. Pacific Grove, California: Wadsworth and Brooks/Cole Publishing Company, 1991.

[46] M. Z. Win and J. H. Winters, "Virtual branch analysis of symbol error probability for hybrid selection/maximal-ratio combining in Rayleigh fading," *IEEE Trans. Commun.*, vol. 49, no. 11, pp. 1926–1934, Nov. 2001.

[47] M.-S. Alouini and M. K. Simon, "An MGF-based performance analysis of generalized selection combining over Rayleigh fading channels," *IEEE Trans. Commun.*, vol. 48, no. 3, pp. 401–415, Mar. 2000.

[48] J. W. Craig, "A new, simple and exact result for calculating the probability of error for two-dimensional signal constellations," in *Proc. Military Commun. Conf.*, Boston, MA, 1991, pp. 25.5.1–25.5.5.

[49] M. K. Simon and D. Divsalar, "Some new twists to problems involving the Gaussian probability integral," *IEEE Trans. Commun.*, vol. 46, no. 2, pp. 200–210, Feb. 1998.

[50] D. P. Bertsekas and J. N. Tsitsiklis, *Introduction to Probability.* Athena Scientific, 2008.

[51] W. M. Gifford, M. Z. Win, and M. Chiani, "Antenna subset diversity with non-ideal channel estimation," *IEEE Trans. Wireless Commun.*, vol. 7, no. 5, pp. 1527–1539, May 2008.

[52] W. M. Gifford and M. Z. Win, "On the SNR penalties of ideal and non-ideal subset diversity systems," *IEEE Trans. Inf. Theory*, 2009, submitted for publication.

[53] J. A. Rice, *Mathematical Statistics and Data Analysis*, 3rd ed. Belmont, CA: Brooks/Cole, 2007.

[54] T. Pavani, F. Marchesi, A. Conti, D. Dardari, and O. Andrisano, "A context aware platform for mobility in immersive environment," in *Proc. of Int. Conf. on Immersive Telecommunications (IMMERSCOM)*, Padova, ITALY, Sep. 2007.

[55] H. Wymeersch, J. Lien, and M. Z. Win, "Cooperative localization in wireless networks," *Proc. IEEE*, vol. 97, no. 2, pp. 427–450, Feb. 2009, special issue on *Ultra-Wide Bandwidth (UWB) Technology & Emerging Applications.*

[56] S. Gezici, Z. Sahinoglu, H. Kobayashi, and H. V. Poor, *Ultrawideband Wireless Communications.* John Wiley & Sons, Inc., 2006, ch. Ultra Wideband Geolocation.

[57] R. Verdone, D. Dardari, G. Mazzini, and A. Conti, *Wireless Sensor and Actuator Networks: Technologies, Analysis and Design.* Elsevier, 2008.

[58] Y. Shen and M. Z. Win, "Fundamental limits of wideband localization – Part I: A general framework," *IEEE Trans. Inf. Theory*, vol. 56, no. 10, Oct. 2010, to appear. [Online]. Available: http://arxiv.org/abs/1006.0888v1

[59] Y. Shen, H. Wymeersch, and M. Z. Win, "Fundamental limits of wideband localization – Part II: Cooperative networks," *IEEE Trans. Inf. Theory*, vol. 56, no. 10, Oct. 2010, to appear. [Online]. Available: http://arxiv.org/abs/1006.0890v1

[60] D. Dardari, A. Conti, U. J. Ferner, A. Giorgetti, and M. Z. Win, "Ranging with ultrawide bandwidth signals in multipath environments," *Proc. IEEE*, vol. 97, no. 2, pp. 404–426, Feb. 2009, special issue on *Ultra-Wide Bandwidth (UWB) Technology & Emerging Applications.*

[61] R. J. Fontana and S. J. Gunderson, "Ultra-wideband precision asset location system," *Proc. IEEE Conf. on Ultra Wideband Syst. and Technol. (UWBST)*, vol. 21, no. 1, pp. 147–150, May 2002.

[62] W. C. Chung and D. Ha, "An accurate ultra wideband (UWB) ranging for precision asset location," in *Proc. IEEE Conf. on Ultra Wideband Syst. and Technol. (UWBST)*, Nov. 2003, pp. 389–393.

[63] K. Yu and I. Oppermann, "An ultra wideband TAG circuit transceiver architecture," in *International Workshop on Ultra Wideband Systems. Joint UWBST and IWUWBS 2004.*, Kyoto, Japan, May 2004, pp. 258–262.

[64] D. Dardari, "Pseudo-random active UWB reflectors for accurate ranging," *IEEE Commun. Lett.*, vol. 8, no. 10, pp. 608–610, Oct. 2004.

[65] S. Gezici, Z. Tian, G. B. Giannakis, H. Kobayashi, A. F. Molisch, H. V. Poor, and Z. Sahinoglu, "Localization via ultra-wideband radios: a look at positioning aspects for future sensor networks," *IEEE Signal Process. Mag.*, vol. 22, pp. 70–84, Jul. 2005.

[66] D. B. Jourdan, D. Dardari, and M. Z. Win, "Position error bound for UWB localization in dense cluttered environments," *IEEE Trans. Aerosp. Electron. Syst.*, vol. 44, no. 2, pp. 613–628, Apr. 2008.

[67] D. Dardari, A. Conti, J. Lien, and M. Z. Win, "The effect of cooperation on localization systems using UWB experimental data," *EURASIP J. Appl. Signal Process.*, vol. 2008, pp. Article ID 513 873, 1–11, 2008, special issue on *Cooperative Localization in Wireless Ad Hoc and Sensor Networks.*

[68] C.-C. Chong, Y.-E. Kim, S. K. Yong, and Seong-SooLee, "Statistical characterization of the UWB propagation channel in indoor residential environments," *Wireless Communications and Mobile Computing*, vol. 5, no. 5, pp. 503–512, Aug. 2005.

[69] A. F. Molisch, D. Cassioli, C.-C. Chong, S. Emami, A. Fort, B. Kannan, J. Karedal, J. Kunisch, H. Schantz, K. Siwiak, and M. Z. Win, "A comprehensive standardized model for ultrawideband propagation channels," *IEEE Trans. Antennas Propag.*, vol. 54, no. 11, pp. 3151–3166, Nov. 2006, special issue on *Wireless Communications.*

[70] D. Dardari, C.-C. Chong, and M. Z. Win, "Threshold-based time-of-arrival estimators in UWB dense multipath channels," *IEEE Trans. Commun.*, vol. 56, no. 8, pp. 1366–1378, Aug. 2008.

[71] P. Cheong, A. Rabbachin, J. Montillet, K. Yu, and I. Oppermann, "Synchronization, TOA and position estimation for low-complexity LDR UWB devices," in *Proc. IEEE Int. Conf. on Ultrawideband*, Zurich, Switzerland, Sep 2005, pp. 480–484.

[72] K. Yu and I. Oppermann, "Performance of UWB position estimation based on time-of-arrival measurements," in *International Workshop on Ultra Wideband Systems. Joint UWBST and IWUWBS 2004.*, Kyoto, Japan, May 2004, pp. 400–404.

[73] I. Guvenc and Z. Sahinoglu, "Threshold-based TOA estimation for impulse radio UWB systems," in *Proc. IEEE Int. Conf. on Ultra-Wideband (ICUWB)*, Zurich, Switzerland, 2005, pp. 420–425.

[74] V. Lottici, A. D'Andrea, and U. Mengali, "Channel estimation for ultra-wideband communications," *IEEE J. Sel. Areas Commun.*, vol. 20, no. 9, pp. 1638–1645, Dec. 2002.

[75] H. L. Van Trees, *Detection, Estimation, and Modulation Theory*, 1st ed. New York, NY 10158-0012: John Wiley & Sons, Inc., 1968.

[76] A. J. Weiss and E. Weinstein, "Fundamental limitations in passive time delay estimation - part I: Narrow-band systems," *IEEE Trans. Acoust., Speech, Signal Process.*, vol. ASP-31, no. 2, pp. 472–486, Apr. 1983.

[77] E. Weinstein and A. J. Weiss, "Fundamental limitations in passive time delay estimation - part II: Wide-band systems," *IEEE Trans. Acoust., Speech, Signal Process.*, vol. ASSP-32, no. 5, pp. 1064–1078, Oct. 1984.

[78] J. P. Iannello, "Large and small error performance limits for multipath time delay estimation," *IEEE Trans. Acoust., Speech, Signal Process.*, vol. ASSP-34, no. 2, pp. 245–251, Apr. 1986.

[79] E. Weinstein and A. J. Weiss, "A general class of lower bounds in parameter estimation," *IEEE Trans. Inf. Theory*, vol. 34, no. 2, pp. 338–342, Mar. 1988.

[80] J. Li and R. Wu, "An efficient algorithm for time delay estimation," *IEEE Trans. Signal Process.*, vol. 46, no. 8, pp. 2231–2235, Aug. 1998.

[81] T. Manickam, R. Vaccaro, and D. Tufts, "A least-squares algorithm for multipath time-delay estimation," *IEEE Trans. Signal Process.*, vol. 42, no. 11, pp. 3229–3233, 1994.

[82] A. Zeira and P. M. Schultheiss, "Realizable lower bounds for time delay estimation," *IEEE Trans. Signal Process.*, vol. 41, no. 1, pp. 3102–3113, Nov. 1993.

[83] ——, "Realizable lower bounds for time delay estimation: Part 2-threshold phenomena," *IEEE Trans. Signal Process.*, vol. 32, no. 5, pp. 1001–1007, May 1994.

[84] J. Ziv and M. Zakai, "Some lower bounds on signal parameter estimation," *IEEE Trans. Inf. Theory*, vol. 15, no. 3, pp. 386–391, May 1969.

[85] S. Bellini and G. Tartara, "Bounds on error in signal parameter estimation," *IEEE Trans. Commun.*, vol. 22, no. 3, pp. 340–342, Mar. 1974.

[86] D. Chazan, M. Zakai, and J. Ziv, "Improved lower bounds on signal parameter estimation," *IEEE Trans. Inf. Theory*, vol. 21, no. 1, pp. 90–93, Jan. 1975.

[87] K. L. Bell, Y. Steinberg, Y. Ephraim, and H. L. V. Trees, "Extended Ziv-Zakai lower bound for vector parameter estimation," *IEEE Trans. Inf. Theory*, vol. 43, no. 2, pp. 624–637, Feb. 1997.

[88] D. Dardari, C.-C. Chong, and M. Z. Win, "Improved lower bounds on time-of-arrival estimation error in realistic UWB channels," in *Proc. IEEE Int. Conf. on Ultra-Wideband (ICUWB)*, Waltham, MA, Sep. 2006, pp. 531–537.

[89] H. Anouar, A. M. Hayar, R. Knopp, and C. Bonnet, "Ziv-Zakai lower bound on the time delay estimation of UWB signals," in *in Proc. Int. Symposium on Commun., Control, and Signal Processing (ISCCSP)*, Marrakech, Morocco, Mar. 2006.

[90] B. M. Sadler, L. Huang, and Z. Xu, "Ziv-Zakai time delay estimation bound for ultra-wideband signals," in *IEEE International Conference on Acoustics, Speech and Signal Processing, 2007. ICASSP 2007*, vol. 3, Honolulu, HI, Apr. 2007, pp. 549–552.

[91] J. Zhang, R. A. Kennedy, and T. D. Abhayapala, "Cramer-Rao lower bounds for the time delay estimation of UWBsignals," in *Proc. IEEE Int. Conf. on Commun.*, Paris, France, May 2004, pp. 3424–3428.

[92] Z. Xu and B. Sadler, "Time delay estimation bounds in convolutive random channels," *IEEE J. Sel. Topics in Signal Process.*, vol. 1, no. 3, pp. 418–430, Oct. 2007.

[93] "IEEE standard for information technology - telecommunications and information exchange between systems - local and metropolitan area networks - specific requirement part 15.4: Wireless medium access control (MAC) and physical layer (PHY) specifications for low-rate wireless personal area networks (WPANs)," *IEEE Std 802.15.4a-2007 (Amendment to IEEE Std 802.15.4-2006)*, pp. 1–203, 2007.

[94] C. W. Helstrom, *Elements of Signal Detection and Estimation*, 1st ed. Englewood Cliffs, New Jersey 07632: Prentice-Hall, 1994.

[95] ——, *Statistical Theory of Signal Detection*, 2nd ed. Headington Hill Hall, Oxford: Pergamon Press, 1968.

[96] J. G. Proakis, *Digital Communications*, 4th ed. New York, NY, 10020: McGraw-Hill, Inc., 2001.

[97] H. Sheng, P. Orlik, A. M. Haimovich, L. J. Cimini Jr., and J. Zhang, "On the spectral and power requirements for ultra-wideband transmission," *Proc. IEEE Int. Conf. on Commun.*, vol. 1, pp. 738–742, May 2003.

[98] B. Z. Bobrovsky, E. Mayer-Wolf, and M. Zakai, "Some classes of global Cramér-Rao bounds," *The Annals of Statistics*, vol. 15, no. 4, pp. 1421–1438, 1987.

[99] R. Cardinali, L. De Nardis, P. Lombardo, and M. Di Benedetto, "Lower bounds for ranging accuracy with multi band OFDM and direct sequence UWB signals," *IEEE International Conference on Ultra-Wideband (ICU 2005)*, pp. 302–307, Sep. 2005.

[100] A. D'Andrea, U. Mengali, and R. Reggiannini, "The modified Cramer-Rao bound and its application to synchronization problems," *IEEE Trans. Commun.*, vol. 42, no. 2,3,4, pp. 1391–1399, Feb.-Apr. 1994.

[101] B. Hu and N. C. Beaulieu, "Exact bit error rate of TH-PPM UWB systems in the presence of multiple access interference," *IEEE Communications Letters*, vol. 7, pp. 572–574, Dec. 2003.

[102] A. Giorgetti, M. Chiani, and M. Z. Win, "The effect of narrowband interference on wideband wireless communication systems," *IEEE Trans. Commun.*, vol. 53, no. 12, pp. 2139–2149, Dec. 2005.

[103] ——, "Ultrawide bandwidth Rake reception in the presence of narrowband interference," in *Proc. IEEE Semiannual Veh. Technol. Conf.*, vol. 3, Milan, Italy, May 2004, pp. 1659–1663.

[104] J.-Y. Tourneret, A. Ferrari, and G. Letac, "The noncentral Wishart distribution: properties and application to speckle imaging," in *IEEE Workshop on Statistical Signal Processing*, Bordeaux, France, Jul. 2005, pp. 924–929.

[105] J. Gil-Pelaez, "Note on the inversion theorem," *Biometrika*, vol. 38, no. 3/4, pp. 481–482, Dec. 1951.

[106] L. Fenton, "The sum of lognormal probability distributions in scatter transmission systems," *IEEE Trans. Commun.*, vol. CS-8, pp. 57–67, Mar. 1960.

[107] S. C. Schwartz and Y. S. Yeh, "On the distribution function and moments of power sums with lognormal components," *Bell System Technical Journal*, vol. 61, pp. 1441–1462, Sep. 1982.

[108] N. C. Beaulieu and Q. Xie, "An optimal lognormal approximation to lognormal sum distributions," *IEEE Trans. Veh. Technol.*, vol. 53, no. 2, pp. 479–489, Mar. 2004.

[109] N. B. Mehta, J. Wu, A. F. Molisch, and J. Zhang, "Approximating a Sum of Random Variables with a Lognormal," *IEEE Trans. Wireless Commun.*, vol. 6, no. 7, p. 2690, 2007.

[110] A. Safak, "Statistical analysis of the power sum of multiple correlated log-normal components," *IEEE Trans. Veh. Technol.*, vol. 42, no. 1, pp. 58–61, Feb. 1993.

[111] A. Lei and R. Schober, "Coherent max-log decision fusion in wireless sensor networks," *IEEE Trans. Commun.*, vol. 58, no. 5, pp. 1327–1332, May 2010.

[112] W. M. Gifford, W. Suwansantisuk, and M. Z. Win, "Rake subset diversity in the presence of non-ideal channel estimation," in *Proc. IEEE 1st Int. Conf. on Next-Generation Wireless Systems*, Dhaka, Bangladesh, Jan. 2006, pp. 253–259.

[113] A. A. Abu-Dayya and N. C. Beaulieu, "Outage probabilities in the presence of correlated lognormal interferers," *IEEE Trans. Veh. Technol.*, vol. 43, no. 1, pp. 164–173, Feb. 1994.